Effect of Dislocation Density on Residual Stress in Polycrystalline Silicon Wafers

A Thesis
Presented To
The Academic Faculty

By

Victoria Garcia

In Partial Fulfillment
Of the Requirements for the Degree
Master of Science in Mechanical Engineering

Georgia Institute of Technology

Spring 2008

Effect of Dislocation Density on Residual Stress in Polycrystalline Silicon Wafers

Approved by:

Dr. Steven Danyluk
Manufacturing Research Center
Georgia Institute of Technology

Dr. Shreyes Melkote
School of Mechanical Engineering
Georgia Institute of Technology

Dr. Ajeet Rohatgi
School of Electrical and Computer Engineering
Georgia Institute of Technology

Date Approved: 19th of February, 2008

In loving memory of

my grandmother,

Maria C. Alvarez.

ACKNOWLEDGEMENTS

I would like to give my heartfelt gratitude to my advisor, Dr. Steven Danyluk of the Georgia Institute of Technology for his continual guidance and support throughout this research.

I also would like to express thanks to Dr. Shreyes Melkote of Georgia Institute of Technology for his numerous helpful suggestions and for serving as a member for my thesis committee. I want to thank Dr. Ajeet Rohatgi of Georgia Institute of Technology for his useful education and serving as a member for my thesis committee.

Appreciation goes to Sergei Ostapenko for providing the wafers used in this research and Juris Kalejs for his expert help.

I would like to show gratefulness to Lynn Boatner and Jim Kolopus of Oak Ridge National Laboratories for their assistance in the Laue system data acquisition.

Special thanks to Fang Li for his enormous help in all aspects of my research, especially the polariscopy work. More thanks to Dr. J.C. Lu and Dr. Naresh Thadhani for pushing me forward.

Finally, sincere thanks go to my family and friends for their limitless encouragement. I am grateful to my mother and her tremendous love and support.

TABLE OF CONTENTS

ACKNOWLEDGEMENTS iv

LIST OF TABLES vii

LIST OF FIGURES viii

LIST OF SYMBOLS x

SUMMARY xi

CHAPTER I: INTRODUCTION 1

CHAPTER II: LITERATURE REVIEW 5
2.1 Summary 5
2.2 Overview of Residual Stress 5
2.3 Overview of Dislocation Density 7

CHAPTER III: RESEARCH PLAN 16
3.1 Objective 16
3.2 Approach of the Research 16

CHAPTER IV: METHODOLOGY 20
4.1 Optical Microscope 20
4.2 Back Reflection Laue System 24
4.3 Polariscope 26

CHAPTER V: EXPERIMENTAL RESULTS 28
5.1 Lines 28
5.2 Areas 36

CHAPTER VI: MODELING OF DISLOCATION DENSITY 47

CHAPTER VII: DISCUSSION 63
7.1 Lines 63
7.2 Areas 65

CHAPTER VIII: CONCLUSIONS 68

CHAPTER IX: RECOMMENDATIONS 70

APPENDIX A: Experimental Data - Residual Stress vs Dislocation Density 71

APPENDIX B: Residual Stress Modeling Using a Constant A 74

APPENDIX C: Residual Stress Piecewise Modeling Using Variable A.......................... 79

APPENDIX D: Laue Patterns of EFG Wafers 83

REFERENCES 92

LIST OF TABLES

Table 1: Etch Pit Density by B Rau [16] 15

Table 2: Correlation of Dislocation Density to Residual Stress 35

Table 3: Correlation Between Residual Stress and Dislocation Density 45

Table 4: Correlation by Type of Etch Pit 60

Table 5: Summarized Results for Lines with Variable C_1 64

Table 6: Summarized Results for Areas with Variable C_1 66

LIST OF FIGURES

Figure 1a: EFG Growth from C. Bhihe [32] 3

Figure 1b: Front view of EFG growth process from He [13] 3

Figure 1c: Side View of EFG Growth from Hahn [76] 4

Figure 2: a) Edge dislocation b) Edge dislocation after etching c) Screw dislocation d) Screw dislocation after etching [2] 8

Figure 3: Etch pit density vs. minority carrier lifetime by Y. Ohshita [27] 9

Figure 4: Distribution of stress and dislocation density in CZ wafers [24] 14

Figure 5: Basic configuration of the polariscope 17

Figure 6: Flowchart for overall experiment 19

Figure 7: Etch pit counting method 21

Figure 8: Graph of a typical iteration to find optimum color threshold *h* 23

Figure 9: Before and after conversion to black and white image 23

Figure 10: Visualizing Bragg's Law 25

Figure 11: Back reflection Laue system with an example of a Laue pattern 26

Figure 12: Measured Areas of EFG Sample 29

Figure 13: Dislocation Density at Line 10 vs at Line 20 30

Figure 14: Residual Stress at Line 10 vs at Line 20 31

Figure 15: Residual Stress of EFG wafer in MPa 32

Figure 16a: Dislocation Density (Round) vs Stress in Line C (Raw Data) 33

Figure 16b: Dislocation Density (Round) vs Stress in Line C (Smoothed) 34

Figure 17: Dislocation Density (Elliptical) vs Stress in Line C 35

Figure 18: EFG Area 1 (D1-3). Wafer was cracked during measuring. Area Size: 14mm x 8mm 37

Figure 19: Normalized Dislocation Density of Area 1 38

Figure 20: Residual Stress of Area 1 in MPa. Area was measured before the crack........ 38

Figure 21: Microscope image of Area 2 (D1-2). Area Size: 15 mm x 10mm 39

Figure 22: Normalized Dislocation Density Map of Area 2 40

Figure 23: Residual Stress of Area 2 41

Figure 24: Microscope Image of Area 3 (D-3). Area Size: 16mm x 2.5mm 42

Figure 25: Normalized Dislocation Density Map of Area 3 42

Figure 26: Residual Stress of Area 3 in MPa 42

Figure 27: Microscope Image of Area 4 (Wafer A6-3 Area 1). Area Size: 12 mm x 8mm 43

Figure 28: Normalized Dislocation Density Map of Area 4 43

Figure 29: Residual Stress of Area 4 in MPa 44

Figure 30: Maximum Shear Stress Field (Colorbar in MPa) of a Single Dislocation in a 100 x 100 Micron Area 49

Figure 31: Flowchart describing the steps taken to obtain the model 52

Figure 32: Absolute Stress Field (Colorbar in MPa) of an Area 200 x 200 Micron With Dislocation Density of 5 x 10^5 /cm^2, Average Stress: 1.13MPa 53

Figure 33: Absolute Stress Field (Colorbar in MPa) of an Area 200 x 200 Micron Area With Dislocation Density of 1 x 10^6 /cm^2, Average Stress: 1.71MPa 54

Figure 34: Theoretical Maximum Shear Stress vs Dislocation Density 55

Figure 35: Experimental Data plotted with Increasing Dislocation Density 58

Figure 36: Residual stress model based on dislocation density 59

Figure 37: Model vs Experimental by Piecewise (Adjusted C_1 for each half peak)........ 61

LIST OF SYMBOLS

η – Efficiency

ρ – Dislocation density

N – Number of dislocations

$\dot{N}$ – Rate of dislocations

$\dot{\varepsilon}$ – Strain rate

U – Activation energy

τ_{th} – Thermal shear stress

τ_{p} – Stress relaxation caused by plasticity

m – Power constant

K – Constant

h – Maximum color threshold value

λ – Wavelength

d – Distance between sequential atomic plans

θ – Angle

δ – Phase shift caused by polariscope

b – Burgers vector

μ – Shear modulus

ν – Poisson's ratio

SUMMARY

The goal of this research was to examine the relationship between dislocation density and in-plane residual stress in edge-defined film-fed growth (EFG) silicon wafers.

Previous research has shown models for linking dislocation density and residual stress based on temperature gradient parameters during crystal growth. Residual stress and dislocation density have a positive relationship for wafers with very low dislocation density such as Cz wafers. There has been limited success in experimental verifications of residual stress for EFG wafers, without any reference to dislocation density. No model of stress relaxation has been verified experimentally in post production wafers. A model that assumes stress relaxation and links residual stress and dislocation density without growth parameters will be introduced here.

Dislocation density and predominant grain orientation of EFG wafers have been measured by the means of chemical etching/optical microscope and x-ray diffraction, respectively. The results have been compared to the residual stress obtained by a near infrared transmission polariscope. A model was established to explain the results linking dislocation density and residual stress in a randomly selected EFG wafer.

Stress within the wafer increases with dislocation density and other as yet unexplained sources until it reaches a critical resolved shear stress, initiating stress relaxation. A negative square root relationship between dislocation density and residual stress, $\sigma_R = -A\mu b\sqrt{\rho} + \sigma_0$, is introduced here to describe the post production of EFG wafers when stress relaxation occurs. The negative square root model describes the experimental data with a margin of error of 15%. In cases where stress relaxation has not

occurred, a positive square root equation based on stress fields describes the relationship between residual stress and dislocation density with a margin error of 0.3%. The crystallographic grain orientation is found to vary across the growth direction of an EFG wafer with several principal orientations, [210], [110], and [321].

CHAPTER I: INTRODUCTION

The manufacturing of photovoltaic (PV) cells used in solar arrays uses thin wafers produced by edge-defined film-fed growth (EFG), Czochralski (Cz) growth, and casting blocks which are then sliced into wafers. EFG wafers are grown as hollow octagonal tubes as shown in Fig.1a. The tubes are cut into wafers by lasers, as shown in Fig.1a, and as a result, kerf loss is dramatically reduced.

During solidification and grain growth of silicon, sheets develop stresses due to thermal gradient at or near the solid-melt interface and this causes atoms to be displaced from their equilibrium lattice positions. If the atoms cannot relax into their original lattice sites, then the crystals are in a state of strain, which may be relieved by annealing. Residual strain frozen into the wafer is termed residual stress (more detail is given in Chapter 2.2). Stress relaxation results in the generation of dislocations (more detail is given in Chapter 2.3).

Residual stress contributes to wafer breakage in the PV manufacturing industry. This thesis addresses the role played by dislocations on the residual stresses of edge-defined film-fed (EFG) wafers on a macroscopic scale. Obtaining this relationship is significant because it may allow manufacturers to adjust their production processes to reduce residual stress. Dislocation density influences residual stress and this research attempts to quantify the link between the two physical effects.

Previous models have been used to calculate the stress distribution for silicon sheets with stress relaxation effects. These models are not adequate due to the lack of knowledge of the creep law applicable to ribbon/EFG growth [1]. Also, models do not

take account of the fact that stress relaxation is inhomogeneous and not uniform since EFG is polycrystalline. There is also uncertainty in the models due to the unknown variation in the temperature profile and other growth parameters [2]. Dislocation density is a parameter that may be related to the magnitudes of residual stresses in silicon. The model in this paper will disregard the growth conditions and directly link dislocation density and residual stress.

In this research, EFG wafers are chosen due to the relatively constant orientation for a straightforward dislocation measurement. Also, EFG is a high speed silicon sheet growth process, which is usually linked with stress relaxation [3]. Stress relaxation will be incorporated in the modeling in this thesis. EFG has a high and large range of dislocation density (10^{5-8} #/cm^2) due to the large thermal stresses. In addition, the rate at which the octagon tubes are being pulled can affect the magnitude of thermal stresses. When increasing the pull rate, the thermal gradient at the solid-melt interface (Fig. 1c) increases, leading to large thermal stresses and in spite of thermal management such as placing a heater above the solid-melt interface to alleviate the sharp thermal gradient [4]. Thermal stresses are still large enough to cause slip, propagating dislocations.

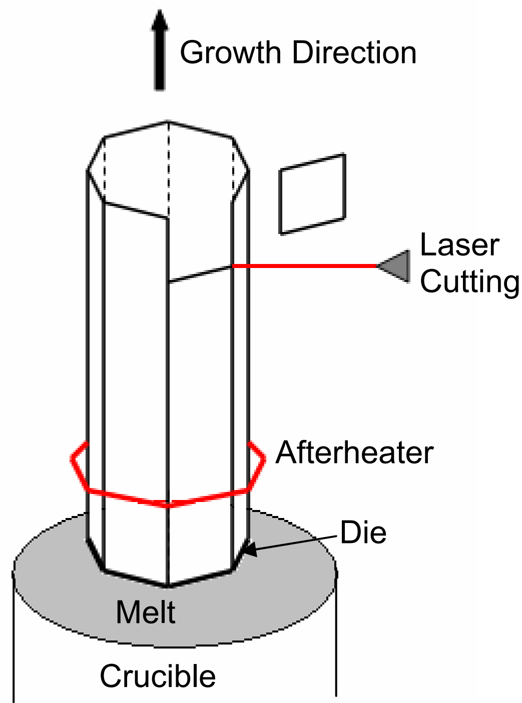

Figure 1a: EFG Growth from C. Bhihe [4]

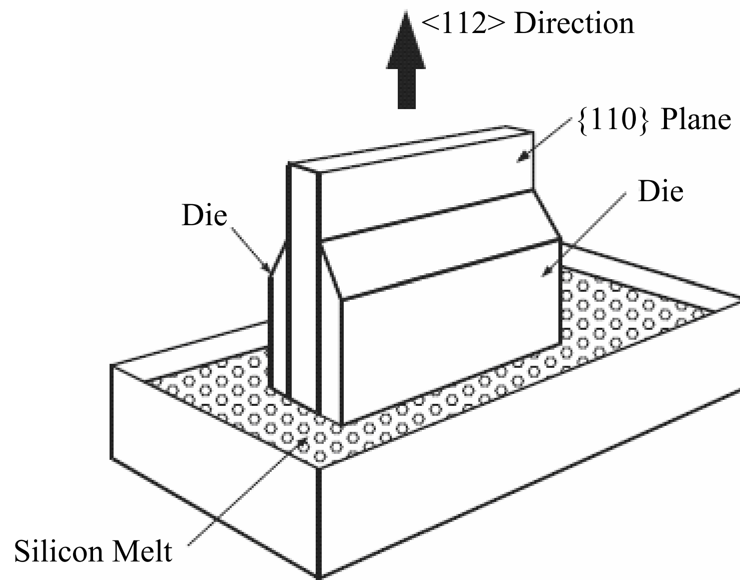

Figure 1b: Front view of EFG growth process from He [5]

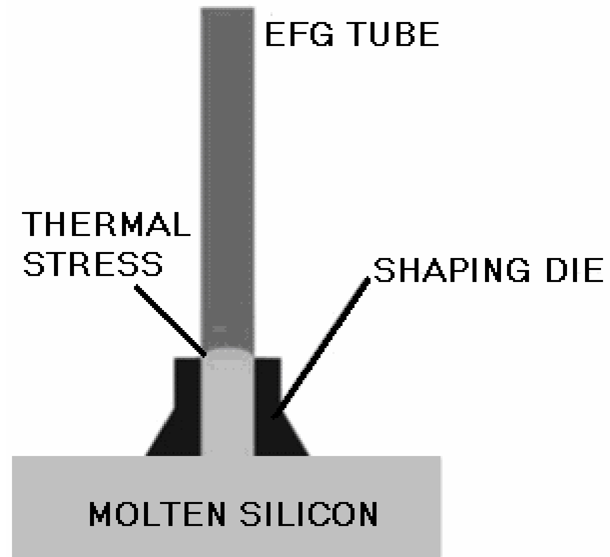

Figure 1c: Side View of EFG Growth from Hahn [6]

CHAPTER II: LITERATURE REVIEW

2.1 Summary

This chapter summarizes the literature review of dislocation density and the relation to residual stress in silicon wafers.

2.2 Overview of Residual Stress

Residual stresses refer to stresses that remain after processing and/or other deformation of a material such as crystal growth, thermal processes, and mechanical processes. For thin silicon wafers used for PV cells, residual stresses are important because of contribution to early failure or wafer breakage when handled. Sensitivity to residual stresses increase with decreasing thickness of wafers. Micro cracks found in the wafer easily propagate into regions of high residual stress causing breakage [7].

When EFG wafers are grown from the melt, the high thermal gradients (~1000°C/cm [8]) at the solid-melt interface result in thermal stresses. The magnitude of the thermal stresses is approximately proportional to the gradient of the temperature profile [9]. Sheet nonuniformity in residual stress is mainly contributed by fluctuations in the die top temperature which are difficult to measure [10]. 2D modeling of residual stress involves a general temperature profile, as seen in the work of J.C. Lambropoulos et. al. [3] and C.K. Bhihe et. al. [4]. Their work also includes stress relaxation by creep deformation. However, since there is a lack of knowledge of creep deformation

applicable to sheet growth [1], the models aforementioned are incomplete. A combination of thermal and mechanical stresses caused during the production is frozen into the wafers in the form of residual stress, which can be reduced but not completely removed from post-growth annealing [11]. In the case of EFG silicon wafers, shear stresses are contributed predominantly by thermal stresses.

There are two types of measurement of residual stress, destructive and non-destructive. Destructive techniques depend on the release of residual stresses, usually in the form of deforming the wafer. A non-destructive technique, which can be used in-situ quality monitoring during the production of silicon wafers, has been used in this research. A number of non-contact techniques to show the residual stress have been developed, such as x-ray diffraction, shadow moiré, and ultrasonic microscopy. However, the near infrared polariscope, proposed by Danyluk et. al [12], is a good candidate for in-plane residual stress measurements. Unlike some of the other techniques, the polariscope uses near infrared light transmitted through the wafer to capture the stress throughout the thickness of the wafer.

The polariscope that was used for this study uses stress-induced birefringence [5]. Stress-induced birefringence was discovered by Brewster and the stress-optic law equation relating stress to birefringence was developed by Maxwell [13]. Isochromatics and isoclinics were the photoelasticity parameters that described the magnitude and direction of the principal stresses by the means of stress-optic law. Fringes were counted to extract the photoelasticity parameters. A fringe multiplier was introduced by Post [14] to increase the sensitivity of fringe counting by ten-fold. A CCD camera/computer was later implemented into the system to find the fringes with higher accuracy. A new

concept to replace fringe counting/analysis was introduced by Hecker and Morche [15]. The concept was continuous phase stepping and uses several images with different optical settings. Since there are 6 unknown equations, 6 images need to be taken. The polarizers in the polariscope are rotated for each image taken. The intensities from the images can be analyzed per pixel to obtain the photoelastic parameters. The parameters are utilized in the stress-optic law to find the residual stress. The polariscope used in this research uses a fringe multiplier and the phase stepping method, increasing sensitivity and accuracy and has been used for other research work [5, 12]. The detailed procedure of using the polariscope will be described in Chapter III.

2.3 Overview of Dislocation Density

Dislocations are crystallographic line defects within a crystal structure and are a result of plastic slip associated with dopants, impurities, mechanical stresses, and thermal stresses. In a crystal structure, deformation occurs along a slip plane, which is generally the closest packed plane. Slip in silicon, a face centered crystal (FCC), occurs preferentially on the {111} plane along the <110> direction. Slip occurs when the shear stress acting on a slip plane reaches a critical value. This resolved shear stress can vary by several orders of magnitude since the critical value is dependent on the crystal structure, temperature, strain rate, impurity concentration, and growth conditions [16].

Two types of dislocations, edge and screw, are distinguished by their Burgers vectors. Edge dislocations have a Burgers vector perpendicular to the dislocation line, while the Burgers vector of the screw dislocation is parallel to the dislocation line. The

area surrounding a dislocation contains strained bonds, which can be broken through chemical reactions such as etching. For example, the alkaline solution from chemical wet etching attacks the surface around the dislocation and results in etch pits. Screw and edge dislocations have unique etch pit shapes, which can be seen in schematic form in Figure 2. Edge dislocations result in a round etch pit while screw dislocations result in a square or hexagonal etch pit [17, 18]. Edge dislocations were the only ones evident on the surface of EFG wafers.

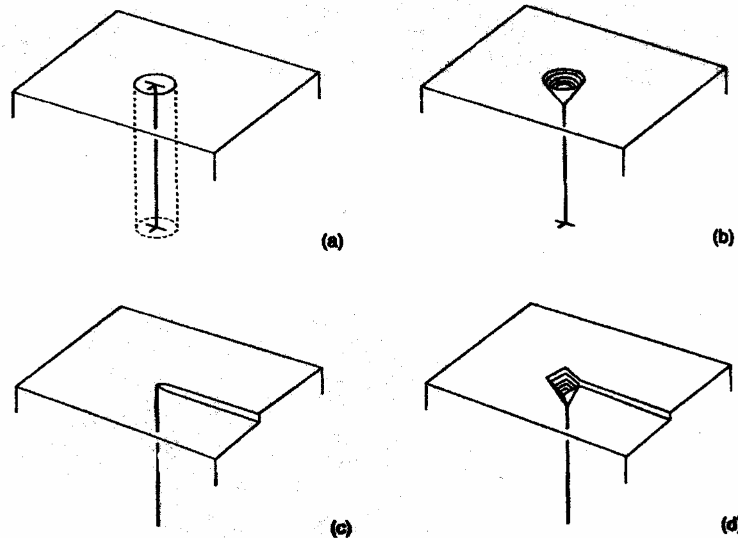

Figure 2: a) Edge dislocation b) Edge dislocation after etching c) Screw dislocation d) Screw dislocation after etching [17]

The effects of dislocations on the electrical properties of silicon have been studied extensively. Dislocations can be a limiting parameter for lifetime in silicon solar cells, reducing efficiency. Y. Ohshita found that areas where there are many defects, the minority carrier lifetime is short [19], causing low efficiency. The resulting relationship can be seen in Fig 3.

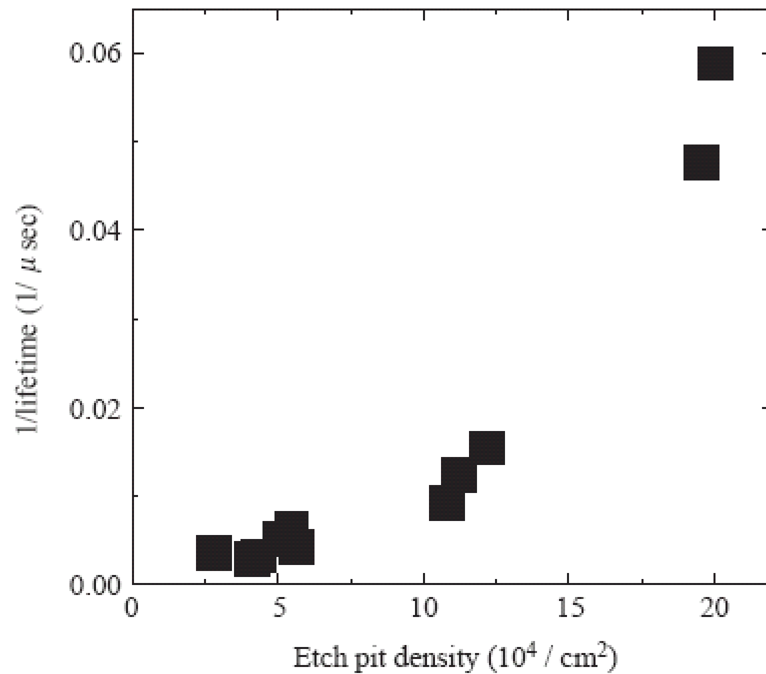

Figure 3: Etch pit density vs. minority carrier lifetime by Y. Ohshita [19]

The general conclusion is that at a dislocation density ranging between 10^3 – 10^4 /cm^2 the performance of the solar cell decreases significantly [20-22]. C.A. Dimitriadis [23] found that areas in a polycrystalline silicon wafer with dislocation density higher than 5 x 10^5/cm^2 has a relationship of conversion efficiency η to dislocation density ρ approximately $\eta \sim \rho^{-1}$. Dislocation density lower than 5 x 10^5/cm^2 follows closer to the equation $\eta \sim \rho^{-.5}$. However, other research suggests that there is an incomplete study of the effects of dislocations on the mechanical properties of silicon [15].

Shear stress can generate and propagate dislocations [24]. Long range stress fields occur around a single dislocation due to the discontinuity of the crystal structure. Atoms in the crystal structure displaced from their lattice positions accommodate the dislocation.

The displacement causes strain around the dislocation. Equations that quantify the stress field have been given by Volterra and will be discussed further in Chapter V.

The yield strength of the wafer is determined by the resolved shear stress that is needed to move dislocations along their slip planes. In a perfect crystal structure, dislocations would glide to the surface and annihilate at low stresses. However, dislocations interact with obstacles such as other dislocations, impurities, and other point defects, raising the resolved shear stress, thus raising the yield strength [25].

When silicon wafers are heated to a temperature above 500°C, both dislocation propagation and stress annealing occur [26, 27]. Annealing at temperatures exceeding 1000°C brings a sudden increase in both parameters at the edge of the wafers, not at the center [28]. Even if the temperature gradient is known, there are thermal perturbations magnified by the thinness of wafers [29]. Thermal perturbations can cause non uniformity in mechanical parameters in silicon sheet [10]. Temperature is not the only source of dislocation propagation. Numerous experiments show that dislocations propagate when sufficient stress is applied, by either introducing oxygen [30], bending/torsion [31], and tension [32].

It is well known that dislocation propagation is caused after reaching a critical value of shear stress [33], but the stress can be caused by dopants, impurities, high temperature, and external stresses. Since there are several sources of the generation of dislocations, it is difficult to pinpoint the effects of EFG production.

While most models suggest a positive relationship between dislocation density and residual stress, there has been evidence that residual stress has a negative relationship with dislocation density in high dislocation density material. J.P. Kalejs et al. have found

that EFG wafers have a lower dislocation density but also a higher residual stress than ribbon [34]. R.O. DeNicola and R.N. Tauber studied the effects of pull rate and rotation rate on the residual stress given by polariscope and dislocation density given by optical microsopy in CZ wafers. Graphs of dislocation density and the proposed stress over the same radial distance show a strong negative correlation and can be seen in Fig. 4 [35]. It is possible that if the initial dislocation density, which is at the solid-melt interface, is higher than 10^4, the behavior of stress and dislocation density may differ in the sense that dislocation density is higher and stresses are lower [36].

Extensive work has been done to study the behavior of dislocations during crystal growth. The most successful model that explains dislocation multiplication is the Haasen-Alexander-Sumino (HAS) model [37]. These researchers found that the dislocation multiplication rate at the very first stage of plastic deformation can be described by Eq (1) below and the strain rate can be described by Eq. 2, which is the classic Orowan relation for plastic flow.

$$\dot{N} = KN \frac{v_o}{\tau_0^m} \exp\left(-\frac{U}{kT}\right)(\tau_{th} - \tau_p - A\sqrt{N})^{m+1} \quad (1)$$

$$\dot{\varepsilon}^c = \phi bN \frac{v_o}{\tau_0^m} \exp\left(-\frac{U}{kT}\right)(\tau_{th} - \tau_p - A\sqrt{N})^{m} \quad (2)$$

where N is the number of mobile dislocations, $\dot{N}$ is the dislocation multiplication rate, τ_{th} is the shear stress caused by thermal gradient, τ_p is the stress relaxation caused by plasticity, ε is the creep strain rate, and T is temperature. U, K, v_o, t_o, m, φ, b, and A are material constants. Their model shows that the initial dislocation density, temperature

profile, and shear stress during growth must be known in order to find the final value of dislocation density. Knowing all those parameters is unrealistic in the manufacturing industry and this thesis will focus only on the final values of the parameters. One of the parameters for the HAS model is the initial dislocation density, which refers to the number of dislocations found at the solid-melt interface. No one has been able to experimentally quantify this value. The HAS model assumes dislocations multiply from an initial dislocation, which has an assumed value, and does not take account that new dislocations could form during growth. Also, the temperature profiles usually do not take account of the temperature fluctuations at the die top, which cause sheet nonuniformity. Even though the HAS model will not be used in this paper, it can give insight in explaining the final values of residual stress and dislocation density.

The HAS model has been utilized to find the theoretical stress or dislocation density by several authors [38]. N. Miyazaki et. al. has developed a computer code based on the HAS model to evaluate the dislocation density and compared the results to stresses [39]. The temperatures from the growth of the single crystal ingot, obtained from a heat conduction analysis, were used as input data for the stress calculation based on the theory of crystal plasticity. This comparison showed a high dislocation density with high residual stress, a positive relationship. On the other hand, C. Tsai created a nonlinear finite element formulation simulating dislocation density and residual stress based on the HAS model and his predicted results show that the dislocation density has a strong inverse dependence on the value of back-stress [40]. However, no experimental data have validated the HAS model using dislocation density and residual stress in EFG wafers.

Stress relaxation is not well known for silicon but has been validated on a microscopic scale for the local area around an edge dislocation on the surface [41]. There is experimental evidence that the temperature fluctuations across the sheet width can lead to reduction of stress in order to compensate for the stress produced by the non-uniformities in the axial (along the growth) temperature [42]. Most models that attempt to explain stress relaxation use a creep rate model based on instantaneous shear stress/dislocation density and temperature profile, such as in Equation 1 and 2. There is a lack of knowledge of creep deformation applicable to sheet growth [1], giving uncertainty to stress relaxation models. A model that will only use the final parameters for stress relaxation is introduced in this thesis in Chapter V. This thesis will examine the relationship between dislocation density and residual stress in two cases: stress relaxation occurs and with no stress relaxation.

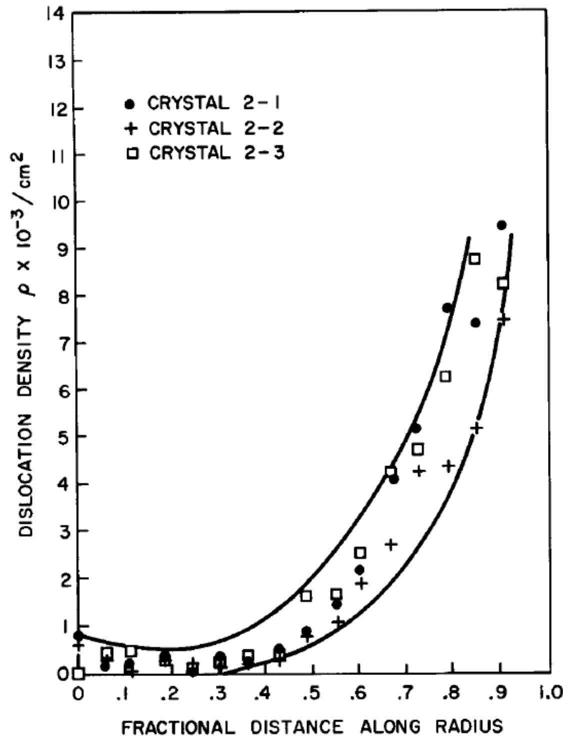

FIG. 3. Dislocation density as a function of radial fraction for crystal 2.

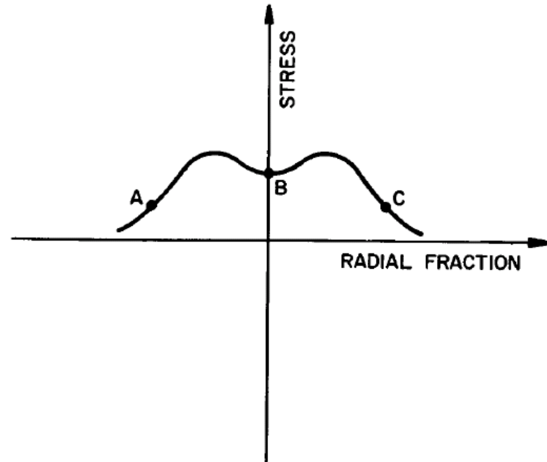

FIG. 14. Proposed stress distribution for crystal 2.

Figure 4: Distribution of stress and dislocation density in CZ wafers [35]

Dislocations can be characterized by a number of ways such as x-ray topography, transmission electron microscopy, and chemical etching. Etch pits are termination points of dislocations that intercept a surface. When a silicon wafer is etched, etch pits form as a result of the chemical attack around the dislocation core. Borle and Bagai [43] characterized etch pits' shapes on various but limited number of crystal planes of silicon. B. Rau et. al. [44] also studied the shapes of etch pits in Si films and has produced a table (Table 1) showing the results of etch pit density. One can see that elliptical etch pits occur in a higher density than round etch pits.

Table 1: Etch Pit Density by B Rau [44]

	Shape of etch pit, surface orientation	Size	Alignment of defect	Density (cm^{-2})
D	Elliptical etch pit, major axis tilted by ~20° with respect to ⟨1 0 0⟩, often appear in pairs	300 nm	⟨3 1 4⟩	2.0×10^8
E2	Elliptical etch pit, major axis ‖ ⟨1 1 0⟩	300 nm	⟨1 1 2⟩	1.6×10^8
E1	Elliptical etch pit, major axis ‖ ⟨1 0 0⟩	<200 nm	⟨1 1 0⟩	0.1×10^8
R	Round etch pit	300 nm	⟨1 0 0⟩	5.0×10^6
L	Lineshaped etch pit ‖ ⟨1 1 0⟩	up to a few μm	⟨1 1 1⟩	$<1 \times 10^5$
P	Squareshaped etch pit	$\sqrt{2} \times d_{Layer}$		2.0×10^5
Total				3.7×10^8

Etch pits can be easily seen with an optical microscope and characterized if the correct etching solution is selected. A.V. Aghabekyan et. al. used x-ray topography and an optical microscope to characterize the distribution of slip dislocations in Cz wafers and found that slip dislocations were preferentially located in concave regions (compressive areas) [45]. The relationship between dislocation density and etch pit density have been investigated and has been shown to have a one-to-one correlation [46-48].

CHAPTER III: RESEARCH PLAN

3.1 Objective

The goal of this research was to find the relationship between the residual stress obtained by using a near-infrared polariscope, and dislocation density using measurements of etch pits.

3.2 Approach of the Research

In this research, EFG wafers were used since their structure is relatively constant and the surface is smooth for a clear picture of etch pits. Dislocation density was measured by means of an optical microscope and image analysis. The resulting images from the optical microscope were used for etch pit counting. Wafers were subjected to both etch pit counting and polariscopy, and the results of etch pit density and residual stress were analyzed for a relationship.

Danyluk, et. al. [5] have designed and built a near infrared polariscope that is used to determine residual stress. The basic set up of the polariscope can be seen in Fig. 5. The polariscope contains a light source, two waveplates, polarizer, analyzer, and a CCD camera to capture the images. The polariscope also has a fringe multiplier to increase sensitivity. Near infrared light is transmitted through silicon and the resulting light beam is influenced by stress, causing birefringence. The phase stepping method was used to extract the photoelastic parameters and find the phase shift δ in order to utilize the stress-

optic law to obtain the magnitude of residual stress. The stress optic law also uses the wavelength of the light λ and the stress optic coefficient C(θ). The stress optic coefficient depends on the lattice structure of the material and the grain orientation. Four point bending was done on a known orientation with an unknown stress optic coefficient for calibration. The purpose of the four point bending test is to apply a known stress that will overwhelm the residual stress, allowing determination of the stress optic coefficient. Four point bending is usually done to beams. If the orientation of the EFG wafer matches the orientation of a silicon beam, the stress optic coefficient is assumed to represent the wafer. The stress optic coefficients of silicon beams of different orientations have been obtained by prior researchers [5]. The orientation of the EFG must be known in order to apply the corresponding stress optic coefficient. A back reflection Laue system was used to obtain the orientation of the EFG wafer surface.

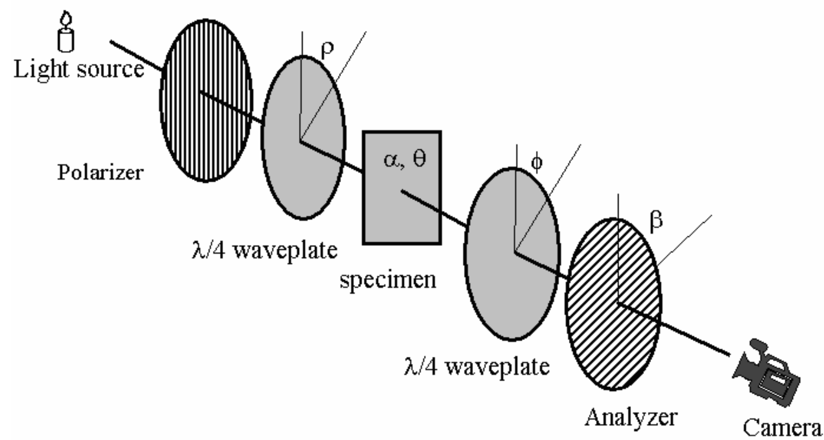

Figure 5: Basic configuration of the polariscope

A back reflection Laue system was used to obtain the orientation of EFG wafer and to verify that the orientation stays constant throughout the wafer. Orientation in this case refers to the crystal structure relative to the surface. Using the known stress optic coefficient with the known orientation, the magnitude of residual stress can be found. This has been done by S. He [13] for the orientation [110]. Several papers have suggested that the surface orientation of EFG is [110] [1, 11, 24, 34, 59].

A flow chart describing the overall aspect of this research is shown in Fig. 6. The flowchart begins with 3 divisions based on the measurement instruments, the polariscope, Laue system, and optical microscope. Each division shows the steps taken to generate the end results, which are stress maps, orientation, and dislocation densities, and all the results are compared and analyzed to find the relationship between dislocation density and residual stress.

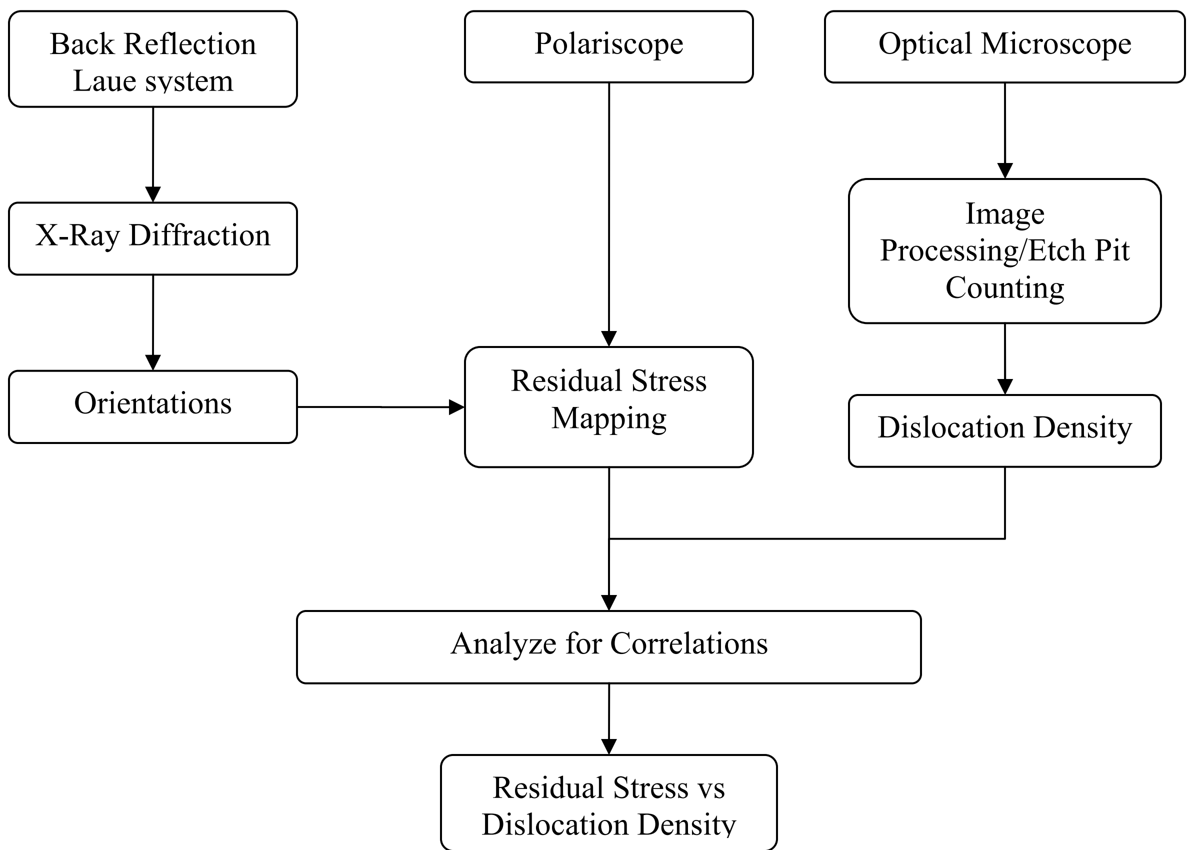

Figure 6: Flowchart for overall experiment

CHAPTER IV: METHODOLOGY

4.1 Optical Microscope

The Nikon Microphot FXL microscope was used to view and analyze images at magnifications in the range of 200-400X. The microscope had a CCD camera with the accompanying software for capturing images. Sequential images were captured and pieced together for a larger area of the wafer.

Chemical etching was done with the Sopori solution consisting of a mixture of HF (46%), CH_3COOH (glacial), and HNO (70%) with the volume ratio of 36:20:2. The samples were mechanically agitated in the etching solution for approximately 30 seconds and then rinsed with deionized water. Etch pit counting were accomplished in two different ways. For the smaller areas captured under a higher magnification (400X), the etch pit line counting method (ASTM F1049) was done per image captured. The method works by drawing 2 diagonal lines on the image such as shown in Figure 7 and counting etch pits that intersect these lines.

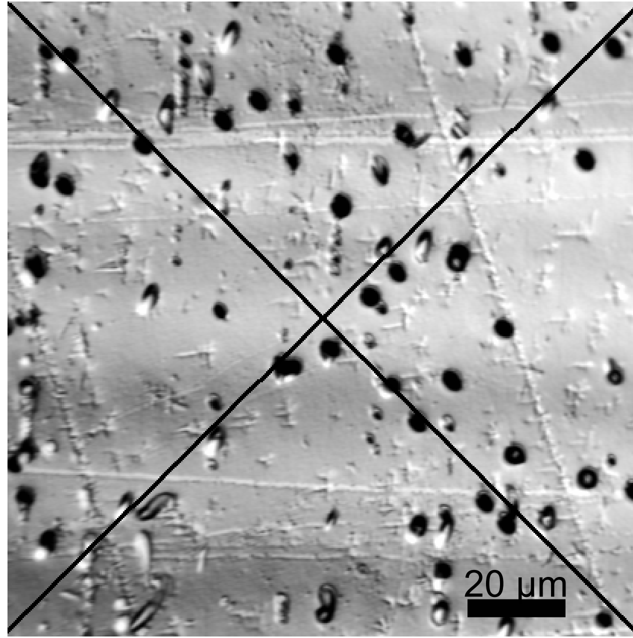

Figure 7: The method of etch pit counting

Then the number of etch pits per area was determined by:

$$\rho = \frac{N}{(2 * L)^2} \qquad (3)$$

where N is the number of counted etch pits on the lines, L is the length of the diagonal line, and ρ is the etch pit density per unit area. For areas that have low dislocation densities and no etch pits intersect with the line, all etch pits in the area were counted instead. An etch pit is taken to represent a single dislocation line, and it is assumed that all dislocations are straight and intersect the viewed surface once, so the etch pit density can be said to be the same as the dislocation density. Since this method was done manually at a high magnification, etch pit types (round and elliptical) were individually counted to determine if one has more bearing on residual stress than the other.

The other etch pit counting method is less accurate but more efficient. After piecing together the images of a larger captured area under a smaller magnification

(200X), the area is sectioned into smaller images to match up with the polariscope resolution. Each pixel in the residual stress map represents the average of residual stress over a 200x200 micron area on the wafer. The microscope has a much higher resolution, therefore a much smaller area of measurement than the polariscope. In order to compare residual stress with dislocation density, the microscope images must be subdivided into 200x200 micron areas so that the average value of dislocation density of each area can be determined. An optimum color threshold value, h, is used to convert the images into black and white pixels. This was done by converting any pixel with the color value of h and above to a black color and anything below h to a white value. A Matlab program has been written to find the average correlation between the residual stress map and the corresponding dislocation density map. The optimum value, h, is necessary to eliminate any lighting differences between the images. By using an iteration of the Matlab program with different values of h, the optimum is found. Figure 8 shows an example of the optimum color threshold value corresponding to the maximum correlation found, which is 154 giving a -29% correlation.

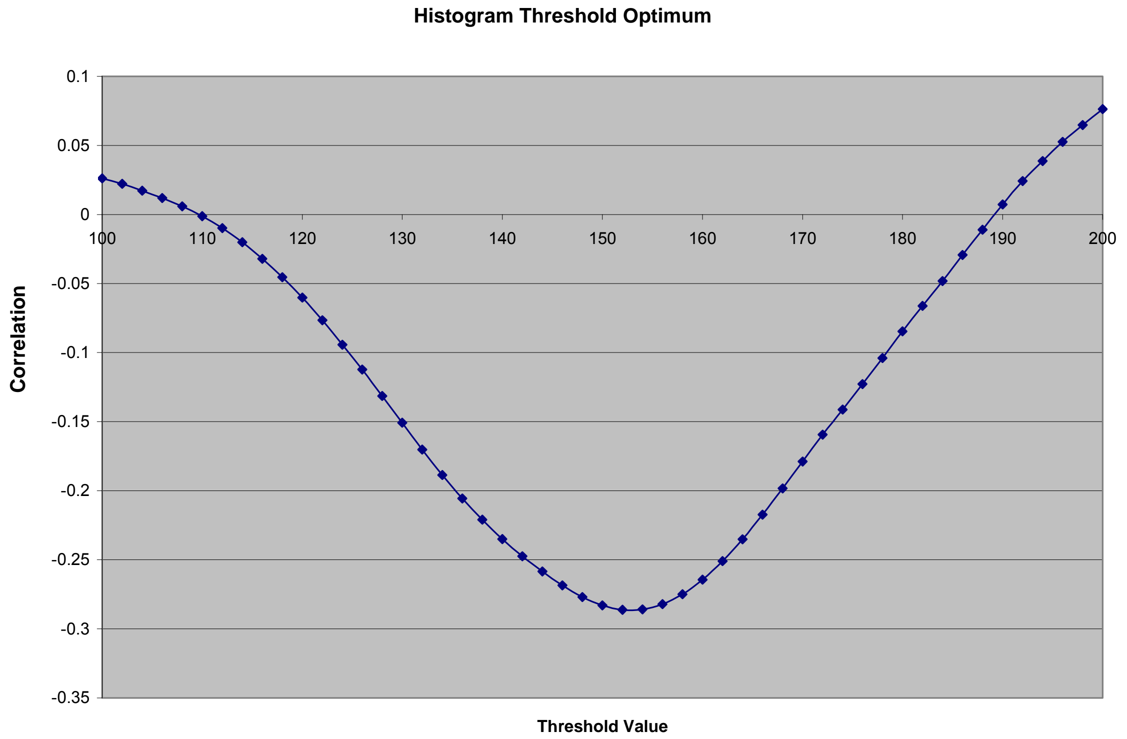

Figure 8: Graph of a typical iteration to find optimum color threshold *h*

The effect of converting into black and white images is shown in Figure 9.

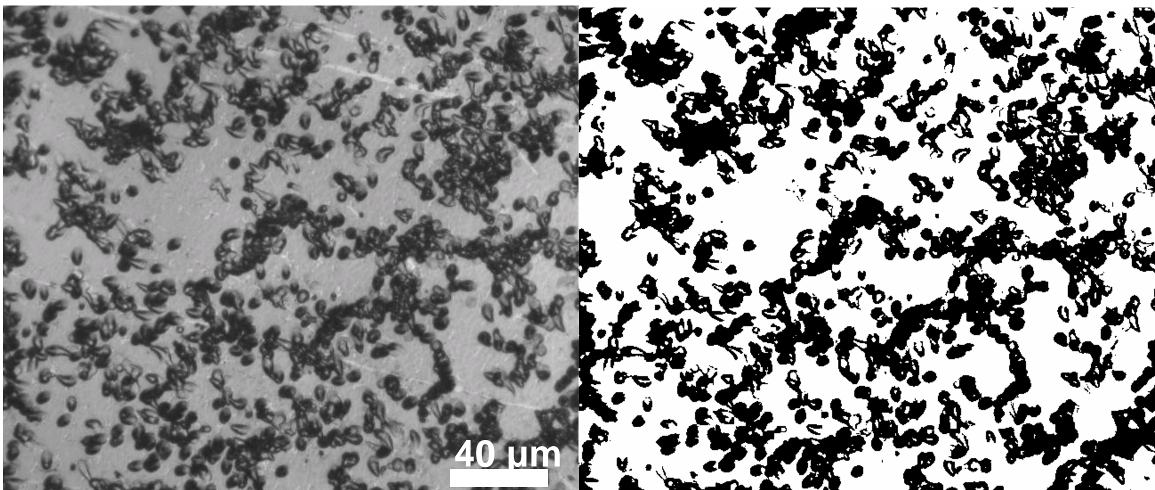

Figure 9: Optical images of an etch wafer before and after conversion to black and white pixels

The percentage of black pixels in the whole area gives a rough value on the etch pit density. There is a loss of accuracy from overlapped etch pits and light scattering/unfocused etch pits, thus incorrectly adding to the etch pit percentage value. The percentage value of black pixels or "etch pit density" is converted into a real dislocation density value by calibration. The etch pits of several samples were manually counted and their values compared to the percentages are used to create a linear equation relating the black pixel percentage to the dislocation density value.

4.2 Back Reflection Laue System

The back reflection Laue system uses x-ray diffraction to determine orientation. The Laue system at the Oak Ridge National Laboratories in Tennessee was used for this research. The Laue system is usually used for checking and adjusting the orientation of a crystal for further study or for checking for deviations from a perfect crystal structure and/or orientation. However, since silicon has a well known crystal structure, the Laue system could be used to check the orientation of the grains with respect to the surface.

A wafer sample is placed in the goniometer and the x-ray beam impinges the surface, perpendicular to the wafer. The beam is reflected to a capture system. The sample could be manipulated in the x and y direction in order to align the beam to the specific area, or grain, to be measured. A computer shows the reflection in real time. The reflection's pattern can then be analyzed to determine the orientation. A pattern reflected

by a certain orientation can be pre-determined by knowing the crystal structure (diamond lattice for silicon) and invoking Bragg's law (Equation 4).

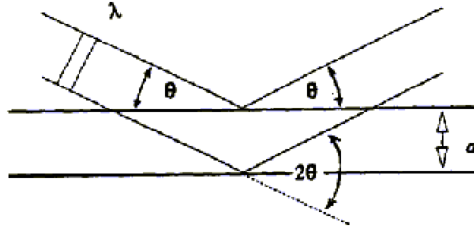

Figure 10: Visualizing Bragg's Law

$$2d \sin \theta = n\lambda \qquad (4)$$

where d is the distance between 2 sequential atomic planes, λ is the wavelength, θ is the angle between the plane and direction of beam, and n is an integer. A Laue pattern consists of dots of varying intensity arranged in specific positions. An example of a Laue pattern can be seen in the top left corner in Fig. 11. Each diffracted beam appears as a dot in a Laue pattern and represents an array of parallel atomic planes. The stronger intensity of the dot correlates to how closely packed the atoms are in the plane. Different planes within the crystal structure will have different d, therefore different theta (angle of incidence). Using geometry of the crystal structure and fixture of the Laue system, the points of diffraction of the x-ray beams can be determined.

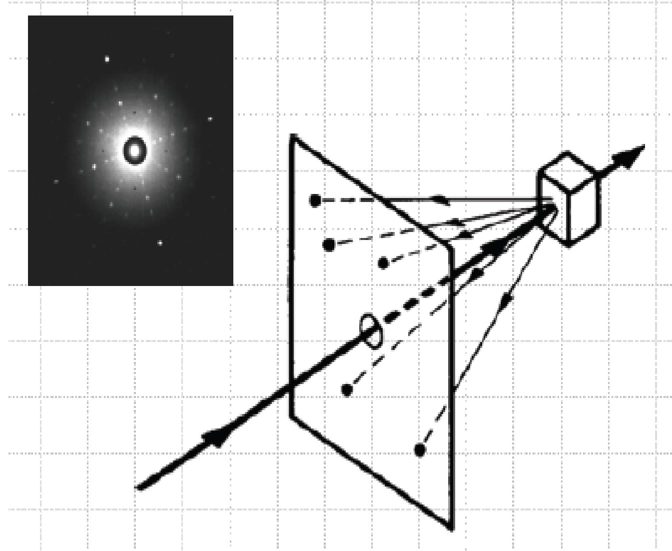

Figure 11: Diagram of a back reflection Laue system with an example of a Laue pattern

A Laue atlas, with over 20 orientations, has been published for the diamond lattice and a matching of patterns to the atlas enables one to determine the orientations of each grain measured.

4.3 Polariscope

In order to find residual stress from the polariscope, the stress optic coefficient C must be known. The stress optic coefficient is orientation dependent, so calibration must be done for each orientation. A known stress is applied to a beam of silicon (10mm by 100mm) by four point bending. The following equation can be used to extract the stress optic coefficient:

$$\sigma_1 - \sigma_2 = \frac{\lambda}{2\pi d C(\theta)} \delta \qquad (5)$$

where σ_1 and σ_2 are the principal stresses, λ is the wavelength of the infrared beam, $C(\theta)$ is the stress optic coefficient based on theta, the angle between stress and orientation, *d* is the thickness of the sample and δ is the phase shift. Phase stepping is where the polarizer and analyzer are adjusted to a specific rotation for each of the six images taken. The value of the light intensity of each corresponding pixel in the resulting images is used in six equations. The six equations include functions of angles that correspond to the configuration of the polarizer and analyzer for each image taken. The equations are used to solve for the phase shift δ parameter. A known stress is applied by a bending moment from four point bending. Working backwards with the known stress from bending and phase shift from the phase stepping method, the stress optic coefficient $C(\theta)$ can be determined for each surface orientation found in the beam. EFG wafers can be taken to have a [110] surface orientation throughout the wafer, so only one stress optic coefficient is needed. The stress optic coefficient of [110] orientation was determined by the four point bending applied to a EFG beam and verified by S. He [5].

CHAPTER V: EXPERIMENTAL RESULTS

5.1 Lines

Seven different areas of several EFG wafers were captured in the optical microscope at either 200X or 400X magnification. Three of the areas were transverse lines perpendicular to the crystal growth. The lines were examined at 400X and two of the lines, Line 10 and Line 20, were measured about 30mm starting from the edge along the 10mm and 20mm mark from the top of the wafer as shown in Fig. 12.

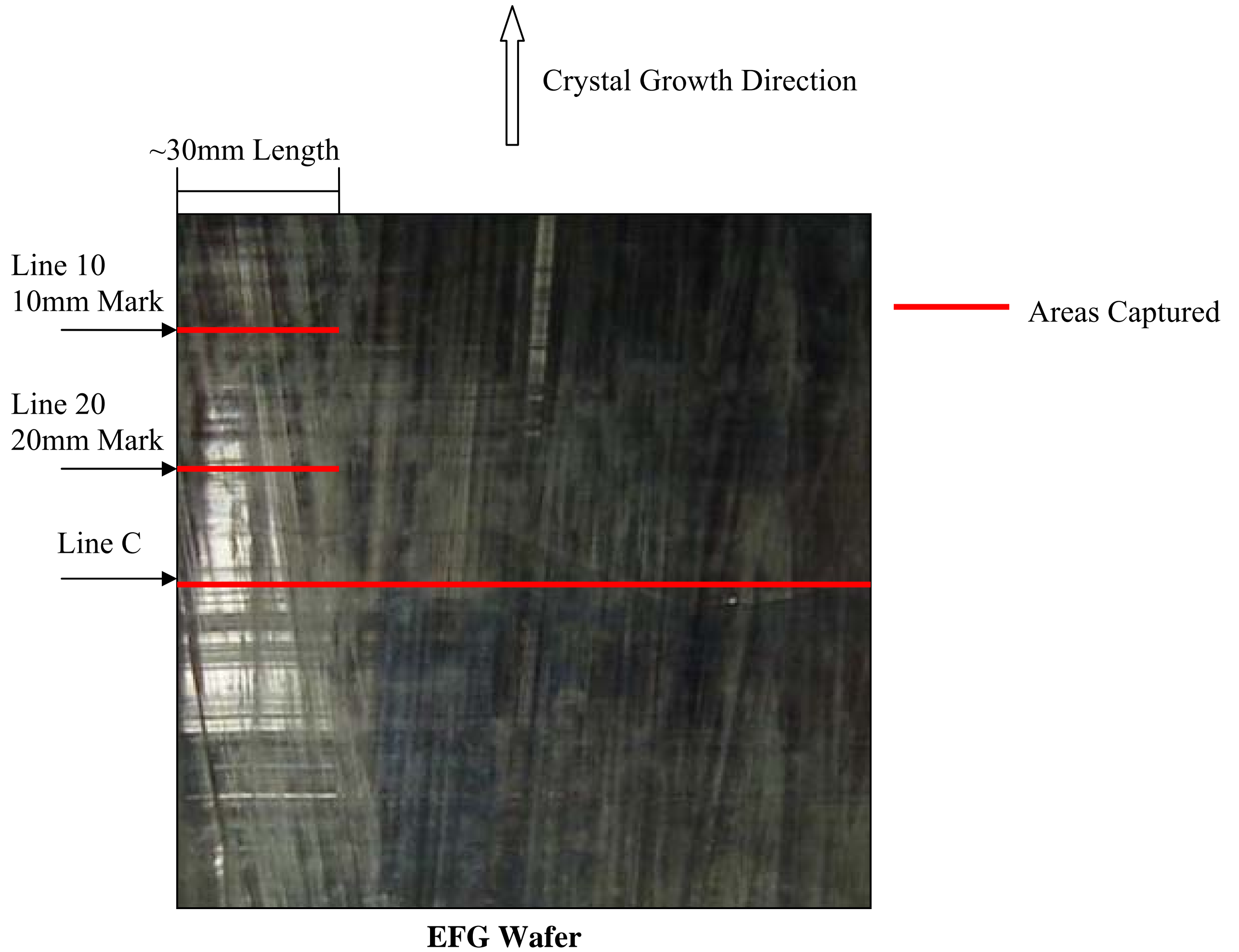

Figure 12: Measured Areas of EFG Sample. Lines 10 and 20 were from same wafer. A different wafer was used for Line C.

The remaining line, Line C, was measured across the entire cross section of the wafer different from the wafer used for the first two lines. Each captured image was subjected to etch pit line counting. Figure 13 and 14 shows the total dislocation density and residual stress respectively of both Line 10 and Line 20.

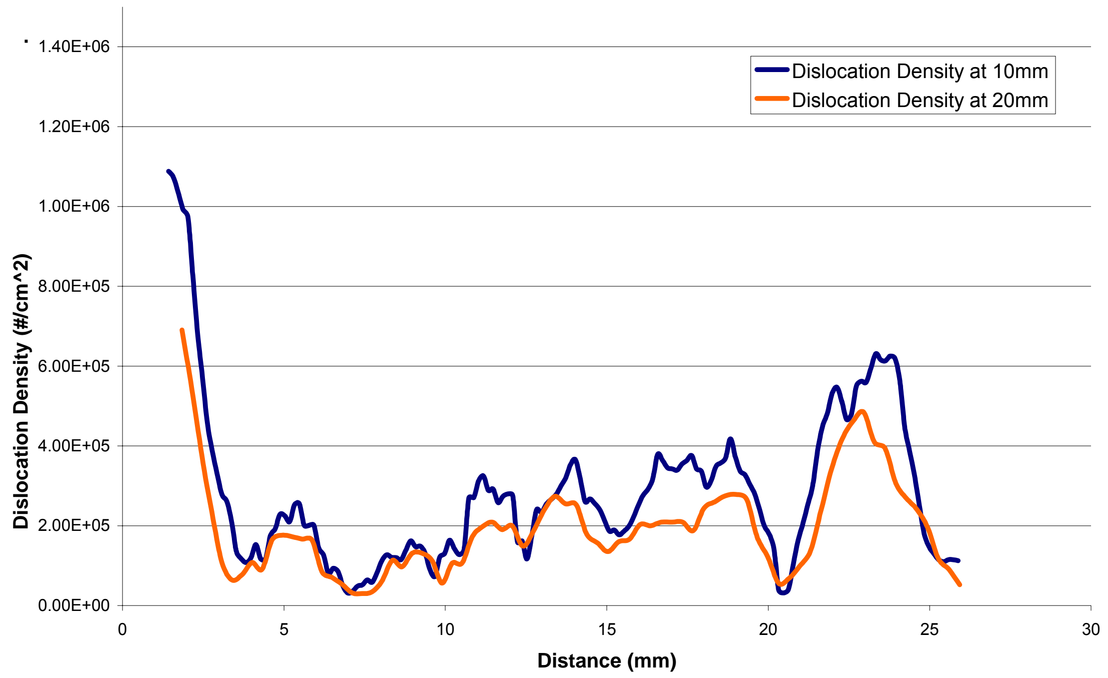

Figure 13: Dislocation Density at Line 10 vs at Line 20. Line 10 is located 10 mm above Line 20 along growth direction.

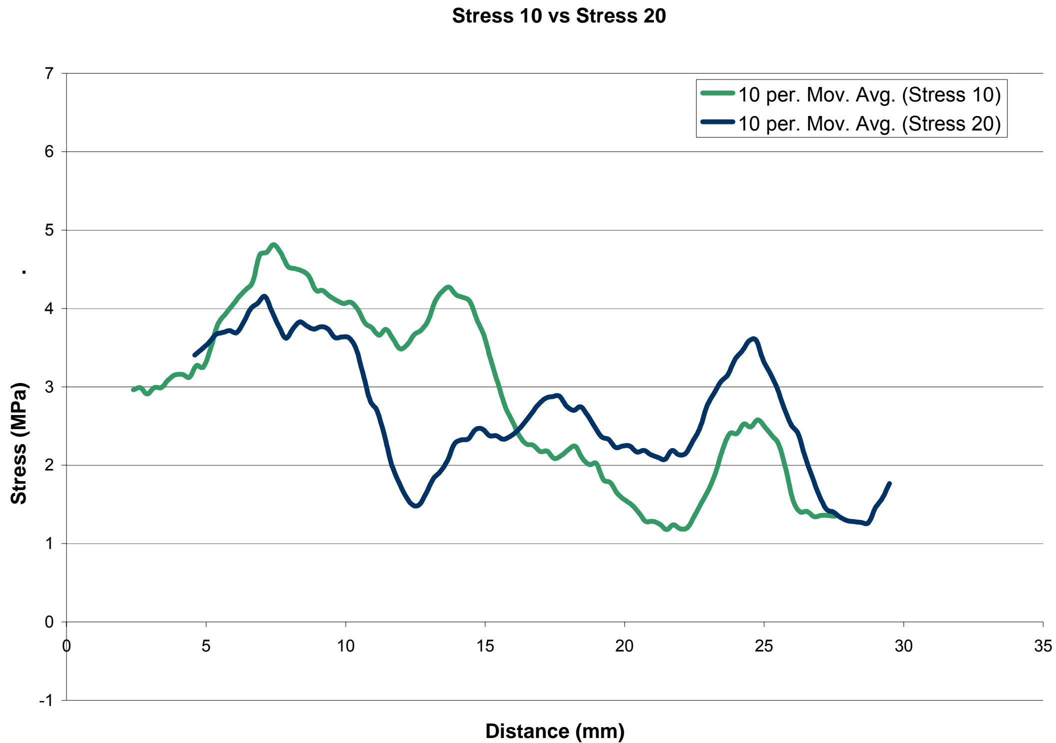

Figure 14: Residual stress at Line 10 vs at Line 20

Aside from a few high dislocation data points from 10mm, the dislocation density data are a reasonable match. This figure shows that the dislocation density stays relatively constant along the crystal growth direction. However, for the stress, there is a very obvious inconsistency between 12 and 16mm indicating stress relaxation. There is an offset in the data due to the slight angle of crystal growth which can be easily seen by looking at the left side of the wafer as shown in Fig 12. To get a clearer picture to compare the data sets in Fig. 13 and 14, Line 20 has been shifted to the right by a few millimeters. In the residual stress map shown in Fig. 15, it is apparent that the residual stress forms a growth pattern similar to dislocation density by looking at the vertical lines of high residual stress. It is also evident in the residual stress map that there are horizontal

lines of higher stress, indicating another source for residual stress. However, the largest stresses are found in the vertical patterns.

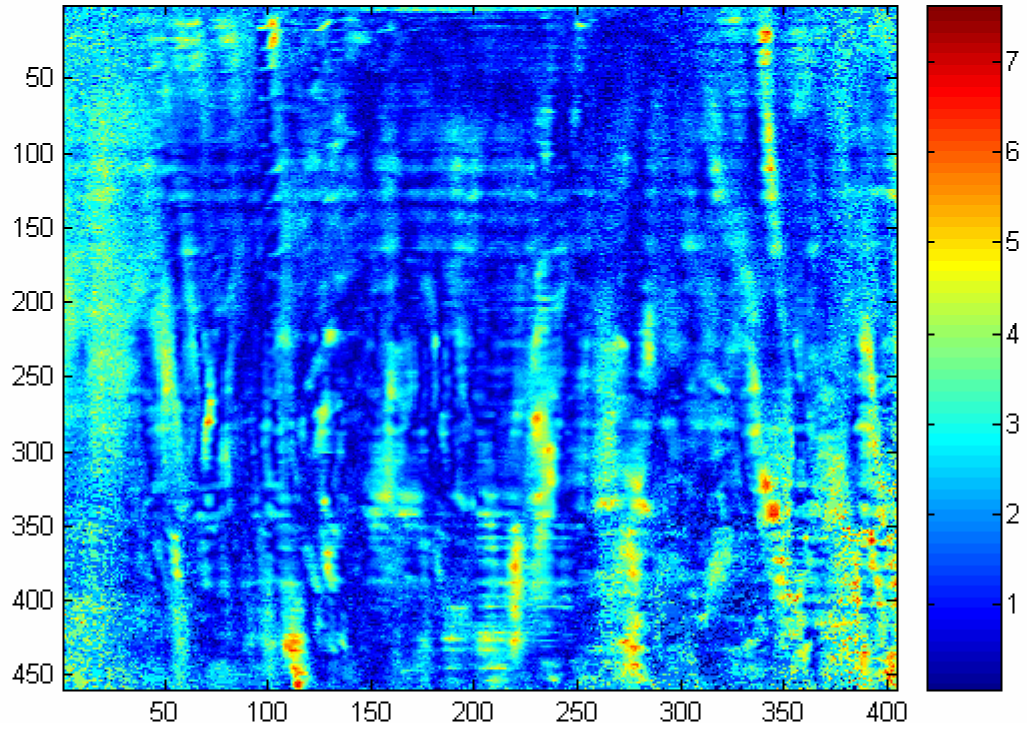

Figure 15: Residual stress (MPa) of EFG wafer captured by polariscope.

For the Line 20, the total number etch pits were counted. For both Line 10 and Line C, the etch pits were separated between round and elliptical shape. The location of corresponding tested area in the stress map was extracted from the dimensions of the whole field images given by the polariscope.

There is a large data variation between consecutive points due to the small measurement area (200x200 microns) per data point (Fig. 16a), so a moving average was done to get the macroscopic mapping of dislocation density. A cubic spline is applied to the moving average of both residual stress and dislocation density (Fig. 16b). Accuracy is

not significantly lost from the smoothing since the data is cumulative. The comparison of dislocation density to residual stress in Line C can be seen in Figure 16b for round etch pits and Figure 17 for elliptical etch pits. Similar graphs for Lines 10 and 20 are found in Appendix A. The distance in the graphs refer to the distance from the edge of the wafer in millimeters. The first 5 millimeters of data for all lines were omitted due to the different behavior of the edges possibly caused from laser cutting.

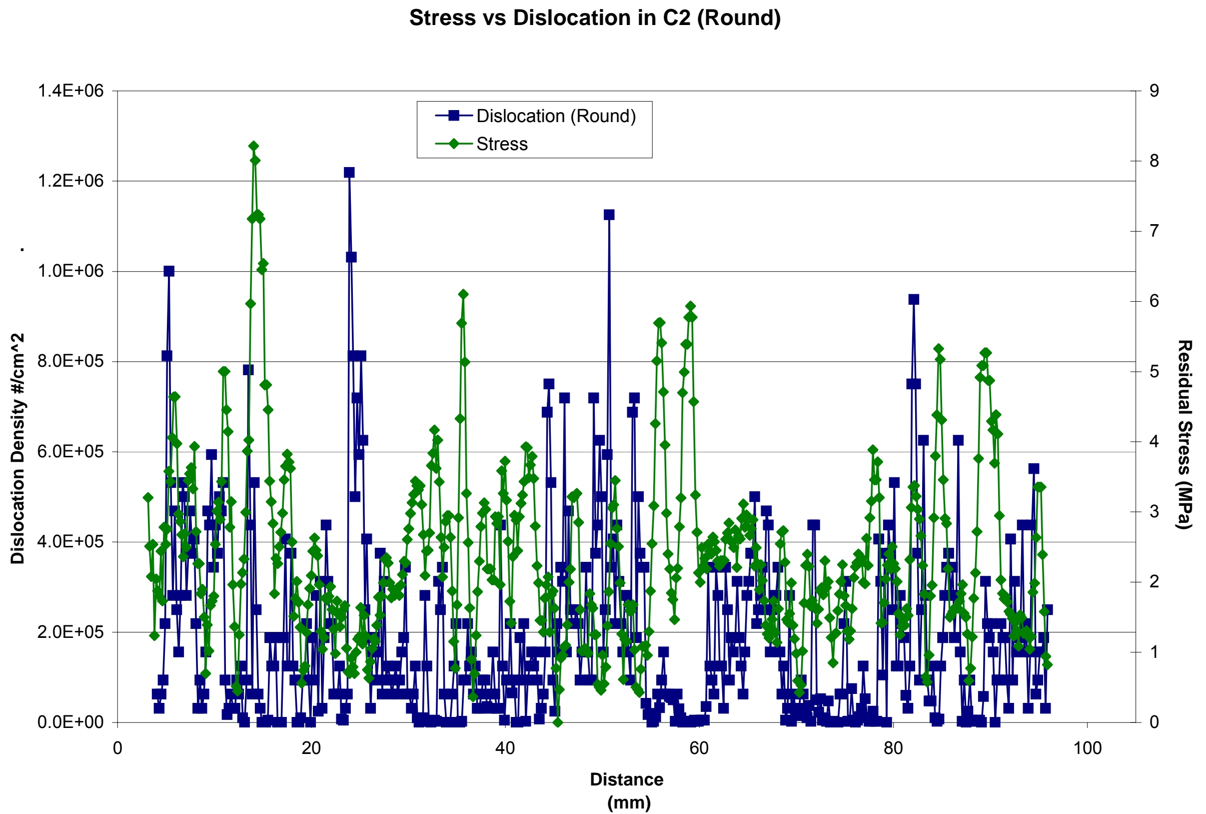

Figure 16a: Dislocation Density (Round Etch Pits) vs Stress in Line C (Raw Data)

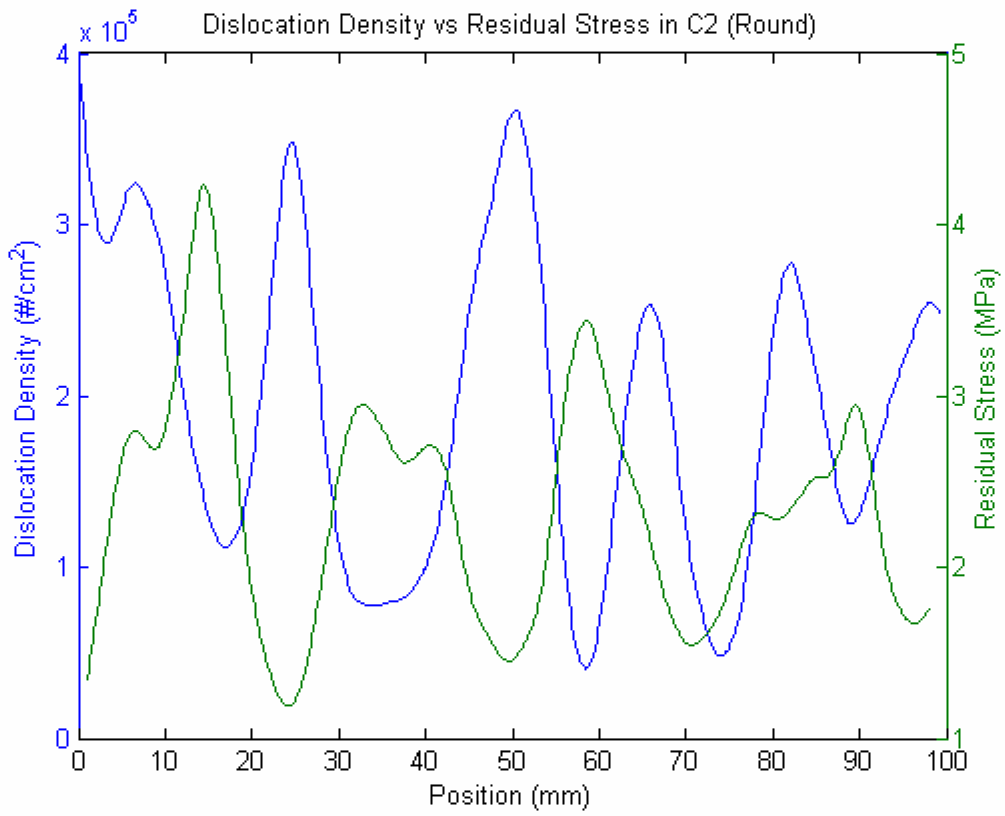

Figure 16b: Dislocation Density (Round Etch Pits) vs Residual Stress in Line C (Smoothed)

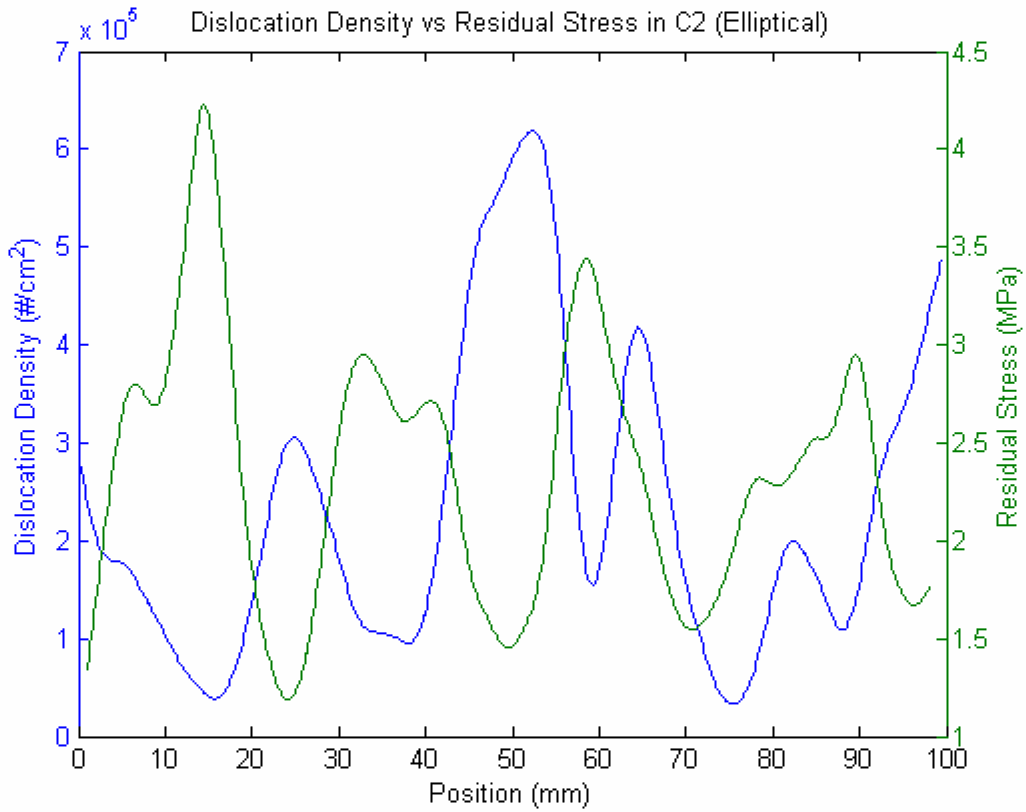

Figure 17: Dislocation Density (Elliptical Etch Pits) vs Residual Stress in Line C

Table 2: Correlation of Dislocation Density to Residual Stress

Labeled Area	Average DD	Correlation %
Total Dislocation at Line 20	1.94E+5	-26.4
Total Dislocation at Line 10	3E+5	4.9
Round Dislocation at Line 10	1.4E+5	13.7
Elliptical Dislocation at Line 10	6.78E+4	17.3
Total Dislocation in Line C	4.23E+5	-34.7
Round Dislocation in Line C	1.92E+5	-27.2
Elliptical Dislocation in Line C	2.32E+5	-32.6

Hypothesis testing has been applied for each line with the null hypothesis of no correlation which was strongly rejected, showing significant evidence of correlation. A significance level of α=.01 was used and shows that the probability of incorrectly rejecting the null hypothesis when it is true is 1%. A strong negative correlation was seen in for the Line 20 and Line C and a positive correlation is seen at Line 10. This would indicate that the results from Line 20 and Line C mostly occurred from stress relaxation, while Line 10 showed evidence of mostly dislocation induced stress.

5.2 Areas

Four larger areas of EFG were also measured. Below are microscope images pieced together to represent a rectangular area in an EFG wafer. Since the areas are large, the images seen in this thesis are at a low magnification showing etch pits as dark shading. The images of the areas are at a high magnification and resolution. The areas were purposefully picked so that one side represents a higher dislocation density than the other. There may be discrepancies in the value of residual stress when measuring different areas due to different lighting conditions that can affect light intensities. Therefore a single area is needed to show the high and low dislocation density to see the behavior in residual stress. Figures 18-29 show, for each area measured, the optical microscope image, normalized dislocation density based on the black and white histogram of the microscope image, and the residual stress from the polariscope. The x and y axis for the residual stress and dislocation density mapping correspond to the pixel

number. All images, both by microscope and polariscope, are taken with the wafer oriented so that the growth direction of the EFG is facing either up or down. The purpose is to see the behavior effects of residual stress and dislocation density along the growth direction.

Figure 18: EFG Area 1 (D1-3). Wafer was cracked during measuring. Area Size: 14mm x 8mm.

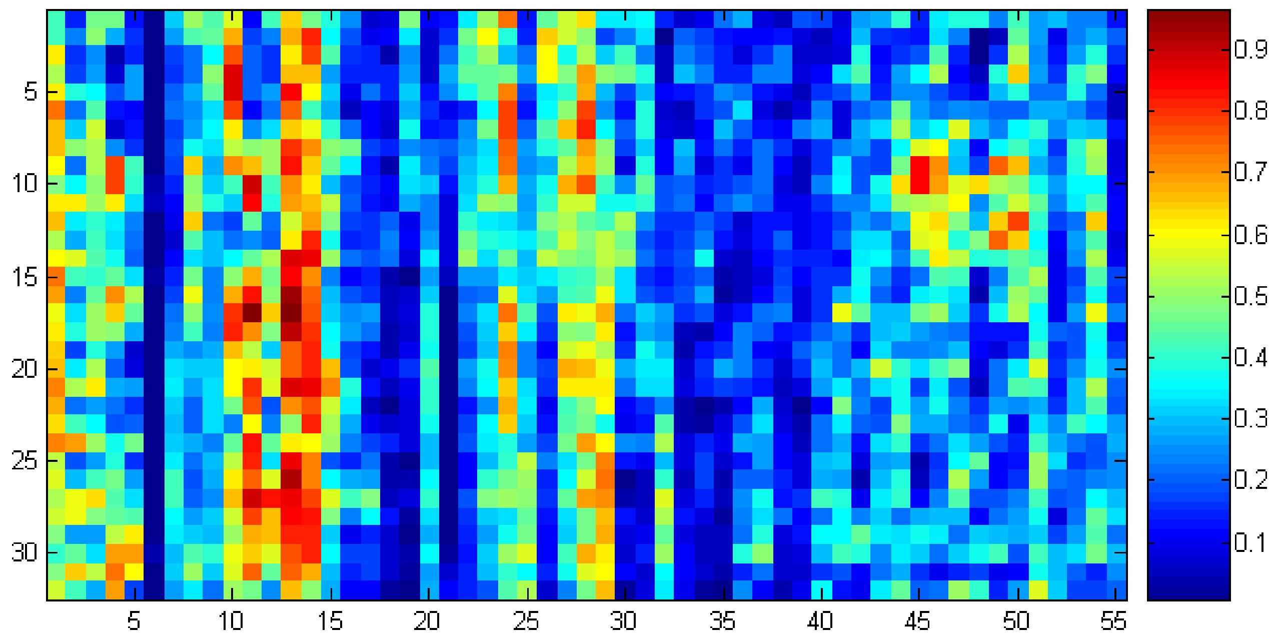

Figure 19: Normalized Dislocation Density of Area 1

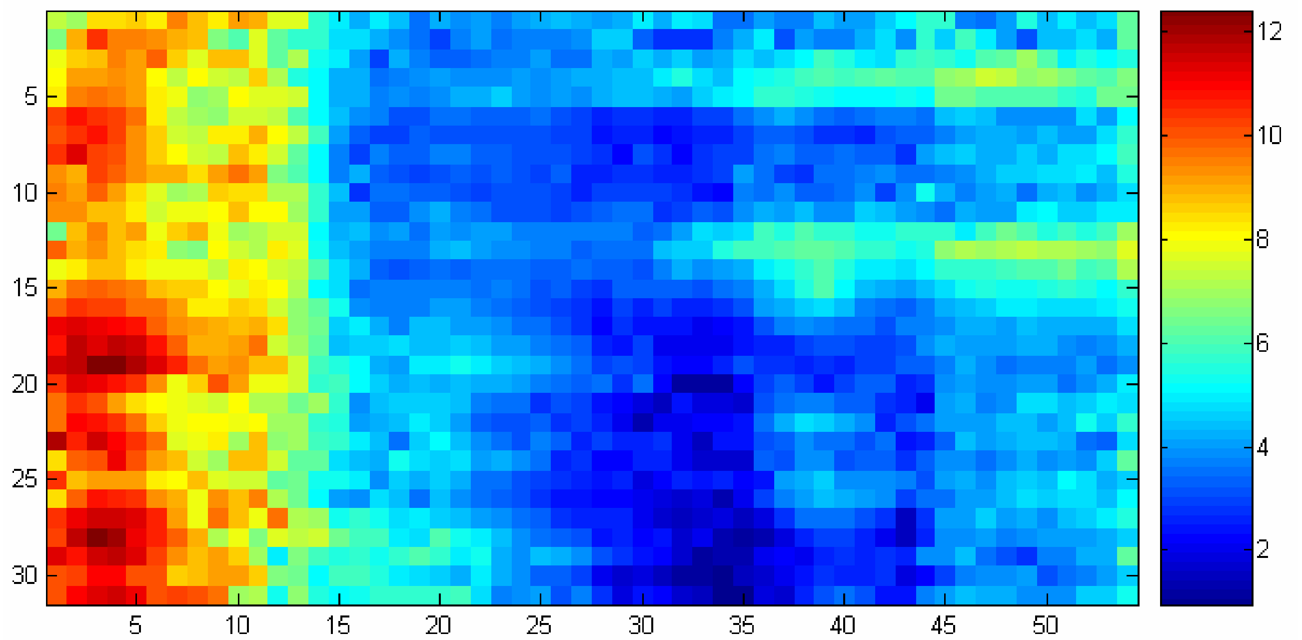

Figure 20: Residual Stress (MPa) of Area 1. Area was measured before the crack.

It’s interesting to note that the crack seen in Fig. 19 propagated though the highest residual stress areas of the region in Area 1. The crack went from the highest stress on the right side and went down to the highest stress on the left side. Area 1 shows evidence of a positive relationship.

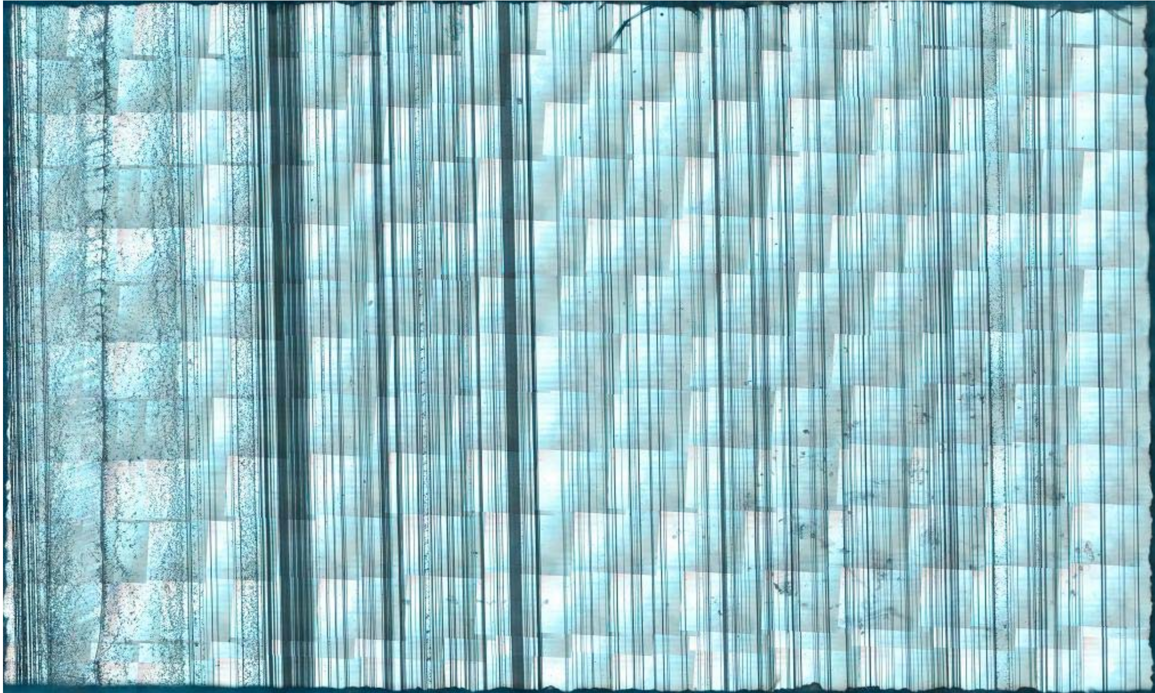

Figure 21: Microscope image of Area 2 (D1-2). Area Size: 15 mm x 10mm.

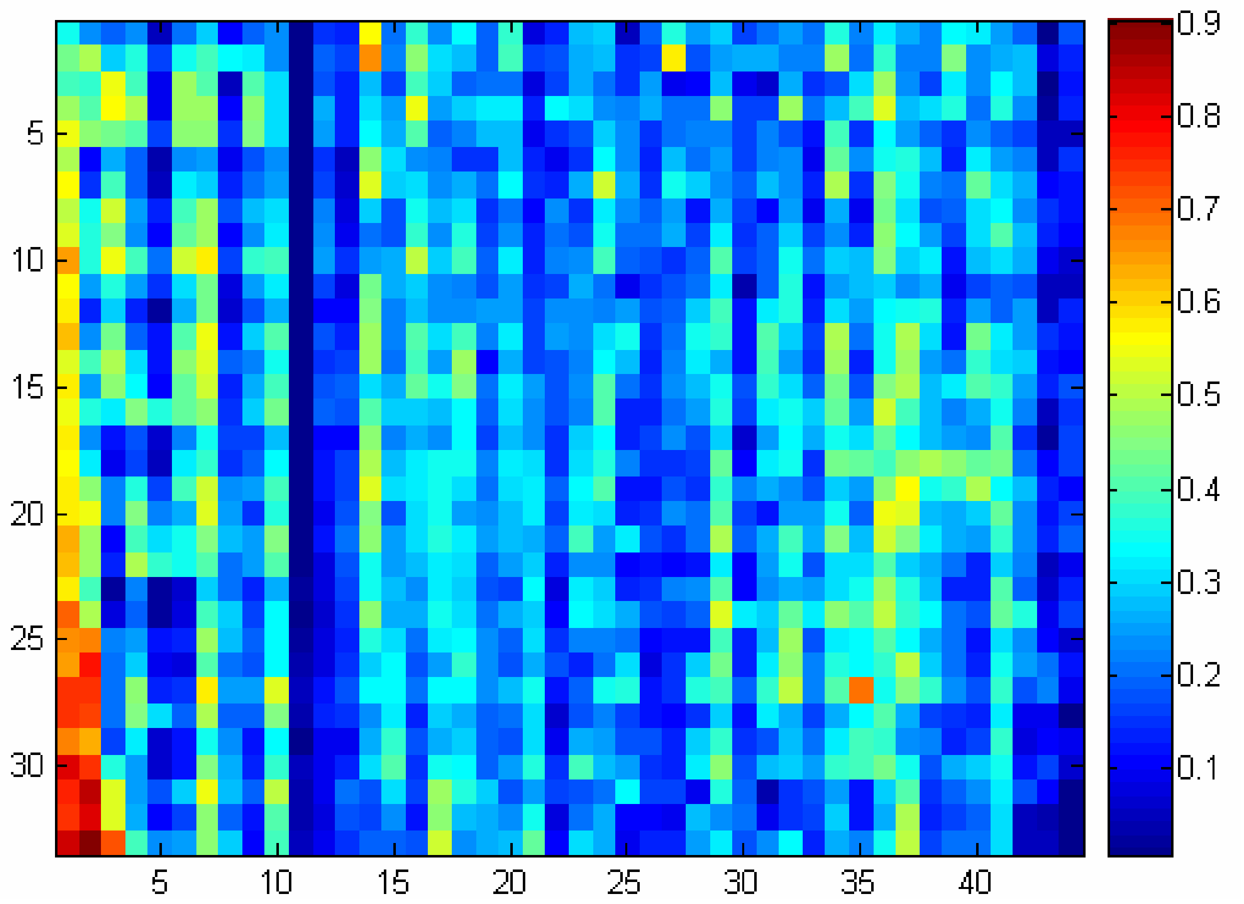

Figure 22: Normalized Dislocation Density Map of Area 2

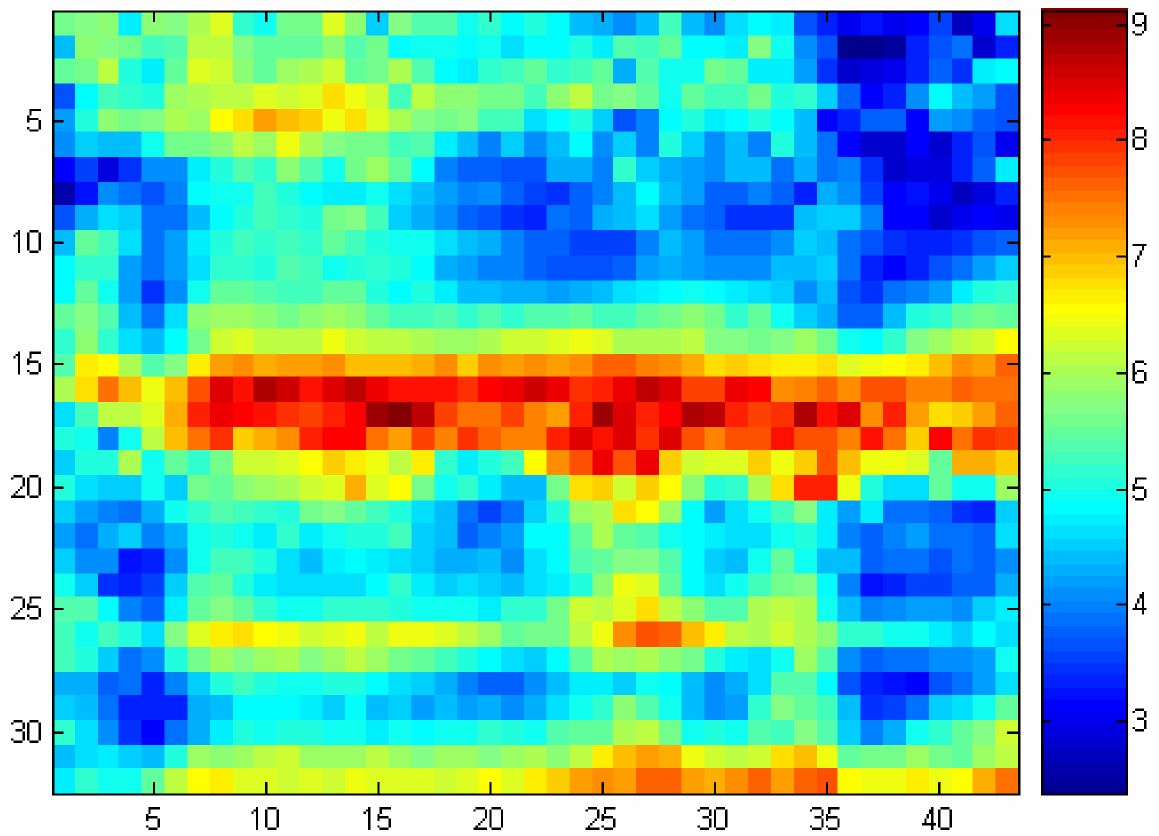

Figure 23: Residual Stress (MPa) of Area 2

Area 2 shows evidence that there is another source other than dislocation density that is causing residual stress. The high residual stress propagates perpendicular to the growth, which is uncommonly seen in EFG wafers.

Figure 24: Microscope Image of Area 3 (D-3). Area Size: 16mm x 2.5mm

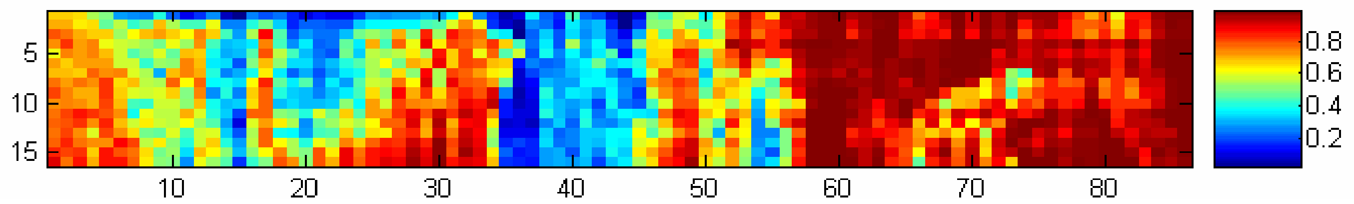

Figure 25: Normalized Dislocation Density Map of Area 3

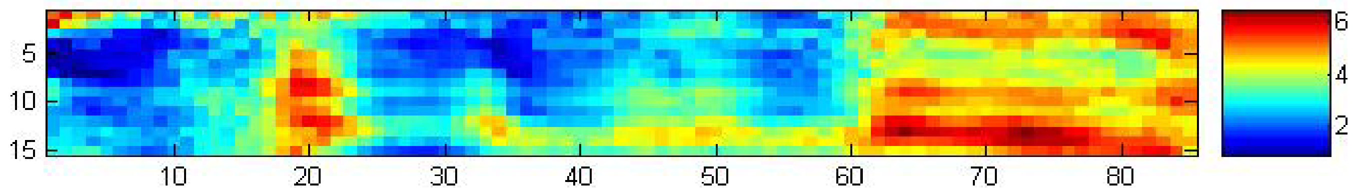

Figure 26: Residual Stress (MPa) of Area 3

Area 3 exhibits both positive and negative relationship. The right half of the area (using ~40 as the halfway mark) shows a positive relationship while the left half show a negative relationship.

Figure 27: Microscope Image of Area 4 (Wafer A6-3 Area 1). Area Size: 12 mm x 8mm

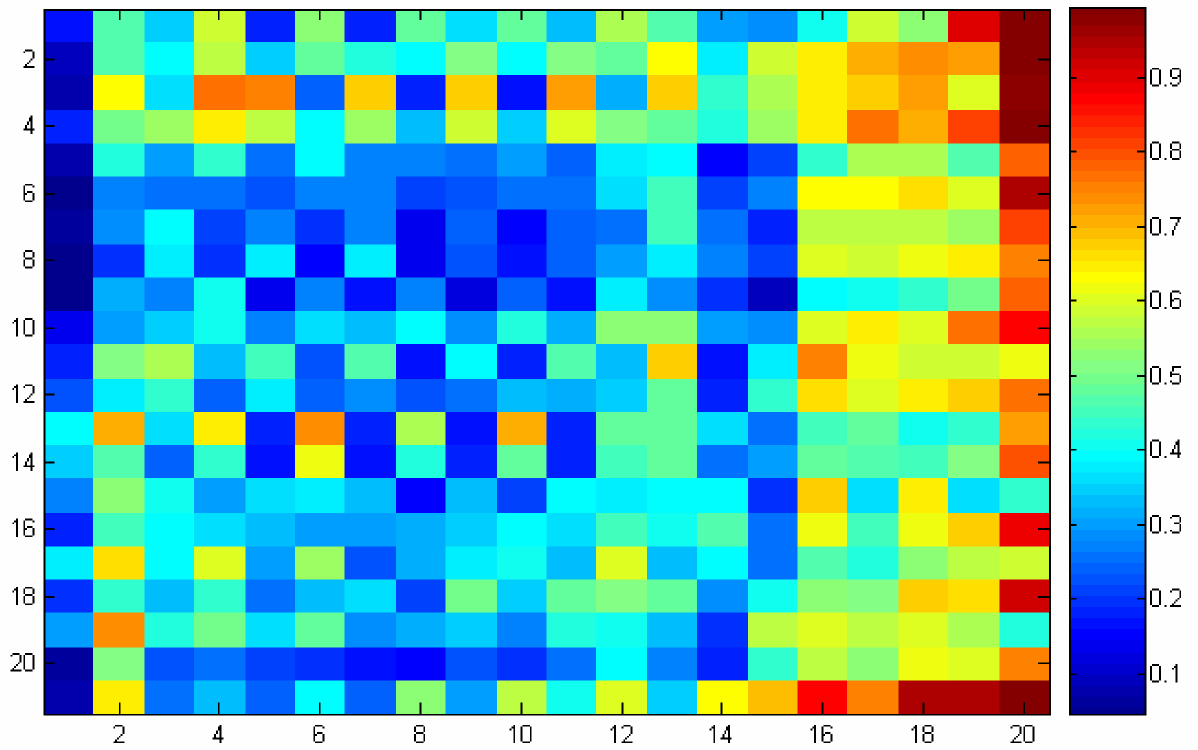

Figure 28: Normalized Dislocation Density Map of Area 4

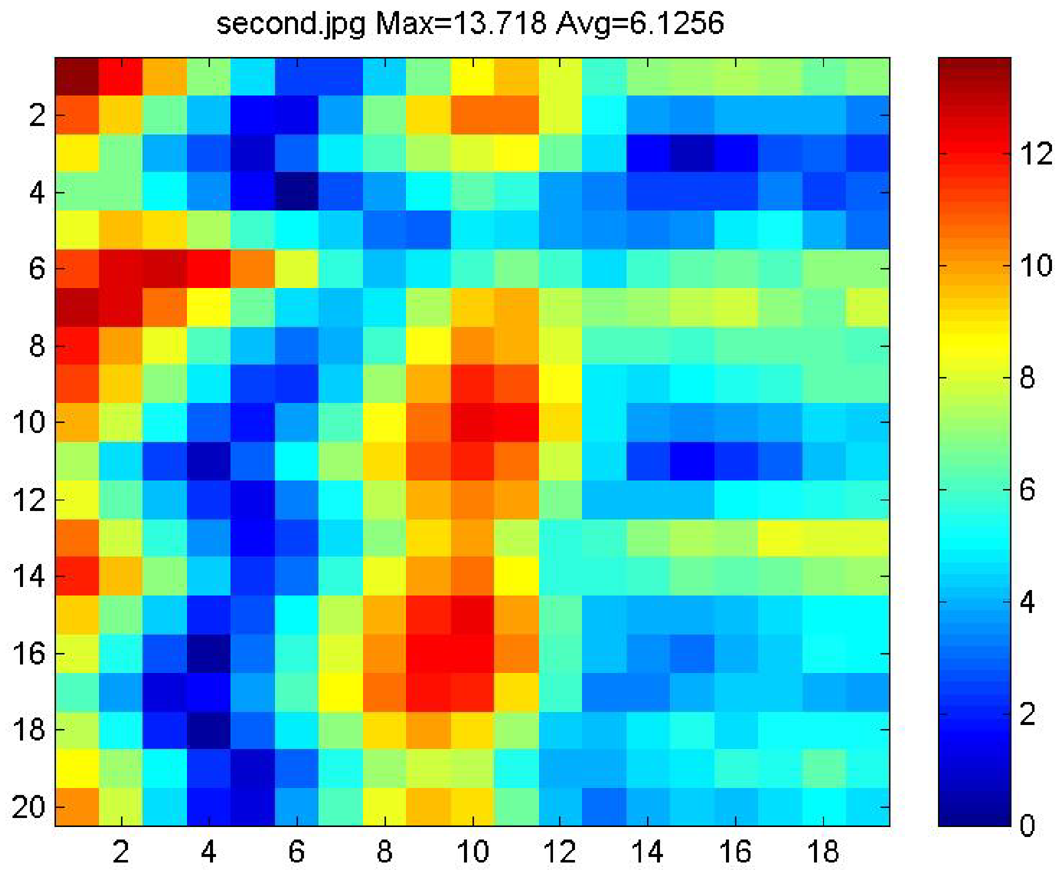

Figure 29: Residual Stress (MPa) of Area 4

Area 4 shows a strong negative relationship. Table 3 summarizes the correlation and the results of hypothesis testing.

Table 3: Correlation between Residual Stress and Dislocation Density

Wafer Area	Correlation %	Hypothesis Testing (p)
Area 1 (D1-3)	24.9	0
Area 2 (D1-2)	-2.2	.34
Area 3 (D-3)	-28.6	0
Area 4 (A6-3 1)	-29.4	0

A check for hypothesis testing for correlation was done on the areas. As done previously, the test uses the null hypothesis of no correlation and a value of $p<.05$ shows significant evidence of correlation. Areas 1, 3 and 4 show correlation with magnitudes of 24%-30% with significant evidence. The hypothesis test has rejected Area 2 due to the overwhelming residual stress from an unknown source. The black lines shown in the microscope images are twin boundaries and have been shown to be dislocation free [49]. The black lines were manually whitened out as not to offset the histogram and give incorrect readings for etch pit density. Some elliptical etch pits are light colored and can be converted into white pixels, undermining the etch pit density. A better image analysis can vastly improve the accuracy of the results.

Orientation of the wafer was checked by x-ray and it was expected to have a relative constant orientation throughout the wafer. Because of multiple twinning, a characteristic feature of EFG wafers, the Laue patterns often showed two orientations at once. The spatial resolution of the x-ray beam is 2 mm and multiple twinning features are often only several hundred microns wide. However, the patterns were watched in real time as the x-ray beam transversed across the wafer in order to find any areas that have a

constant orientation. Some areas showed clear [110], [210], and [321] orientations, with [110] being primary. Three 100x100 mm wafers were subjected to x ray analysis and about 12 data points were taken across each wafer in intervals of approximately 5 mm. Wafer P predominantly had [321], Wafer R had [110], and Wafer Q did not show any predominant orientations. Any similar orientations within a wafer also had the same pole axis rotation. The difference in orientation could affect the range of A in the model. Since silicon has anisotropic properties, orientation affects the magnitude of the shear stress that is being applied directly to the slip plane that causes dislocations.

CHAPTER VI: MODELING OF DISLOCATION DENSITY

Modeling of residual stress in a wafer is very specific to the growth environment, material and process of production. Residual stress of EFG and FZ/CZ wafers has been modeled by C.K. Bhihe et. al. and A. Muiznieks et. al. respectively [4, 50]. However, modeling of residual stress requires extensive knowledge of parameters such as the temperature gradient, initial dislocation density, and solid-liquid interface cooling rate. In addition to the uncertainty of the aforementioned parameters, there is also a lack of knowledge in the creep law that explains stress relaxation. A different approach to modeling of residual stress can be done by knowing the parameters of the aftermath of production such as dislocation defects and impurity concentration. However, only dislocation density will be considered in this thesis. Modeling dislocation density as a function of residual stress will examine two cases. One case will involve the increase of dislocation density which causes an increase in residual stress, resulting in a positive relationship. The other case will examine when the critical resolved shear stress is reached, stress relaxation occurs from the propagation of dislocations, resulting in a negative relationship.

5.1: Case 1 – Dislocation Induced Stress (No stress relaxation)

Starting with a straight edge dislocation in an infinite medium, Equations [6-8] describes the stress field around the dislocation [51]. The z-axis is taken to be the dislocation line (out of the page in Fig. 30).

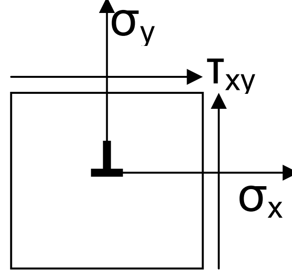

Figure 30: Diagram of stress field around dislocation

$$\sigma_x = \frac{-\mu b}{2\pi(1-v)} \frac{y(3x^2 + y^2)}{(x^2 + y^2)^2} \tag{6}$$

$$\sigma_y = \frac{-\mu b}{2\pi(1-v)} \frac{y(x^2 - y^2)}{(x^2 + y^2)^2} \tag{7}$$

$$\tau_{xy} = \frac{-\mu b}{2\pi(1-v)} \frac{x(x^2 - y^2)}{(x^2 + y^2)^2} \tag{8}$$

A dislocation-induced stress field has been simulated using Matlab. It was assumed that wafers are thin enough to be treated as 2D plates. The polariscope measures the maximum shear stress in a wafer, so the simulation will also be the maximum shear stress field caused by dislocations. The purpose of the simulations was to find the average values for dislocation-induced stress for an area with given dislocation density. The equation for finding the maximum shear stress is found in Eq. 9.

$$\tau_{\max} = \sqrt{\left(\frac{\sigma_x - \sigma_y}{2}\right)^2 + \tau_{xy}^2} \qquad [9]$$

The simulated maximum shear stress field of a single dislocation can be seen in Fig. 12.

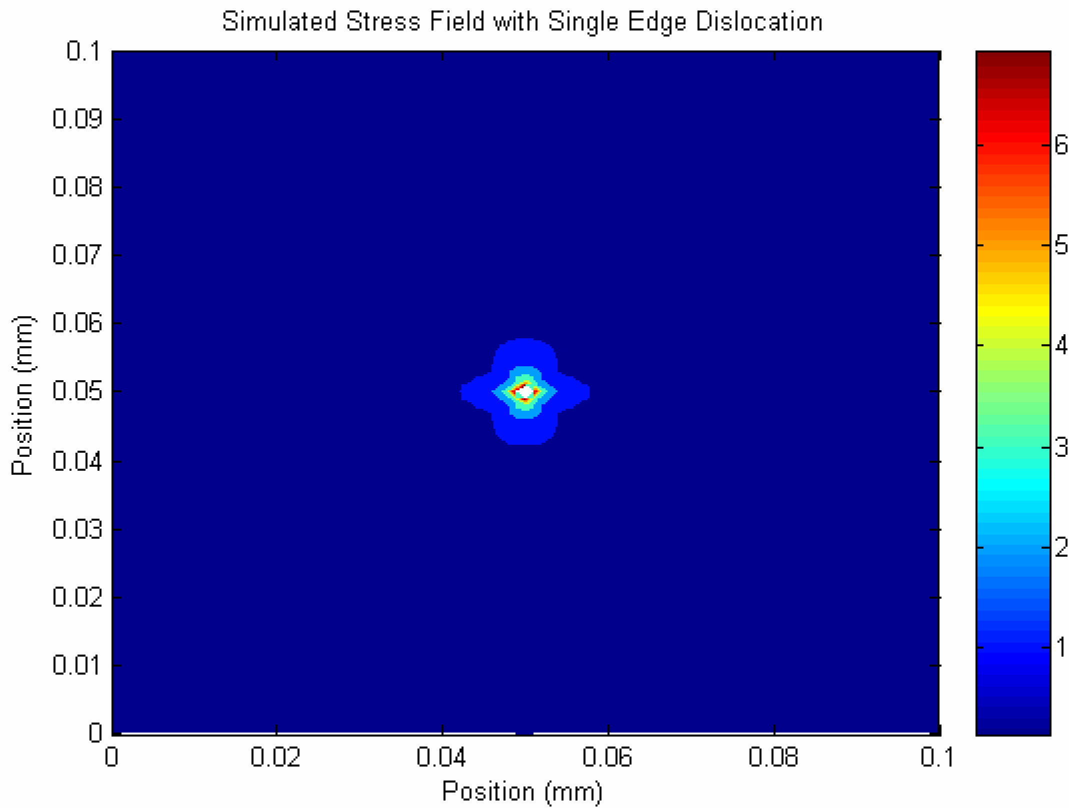

Figure 31: Maximum Shear Stress Field (Color bar in MPa) of a Single Dislocation in a 100 x 100 Micron Area

The area is fixed to 200x200 microns since the resolution of the polariscope takes the shear stress average over this area. Since the area is fixed, the number of dislocations in the area can be calculated knowing the dislocation density. Each dislocation has a stress field as seen in Fig. 31. The orientation and location of the dislocations can be randomized within the area. An example of two dislocations in random positions and orientation is shown in Figure 32. Since the orientations differ, the three stresses, σ_x, σ_y, and τ_{xy}, must be transformed from the local axis, associated with the origin of the dislocation, to the major axis of the stress field. The purpose of this is to be able to add

the three components of stresses from all the dislocations separately. The transformation equations are found in Eq. 10-12.

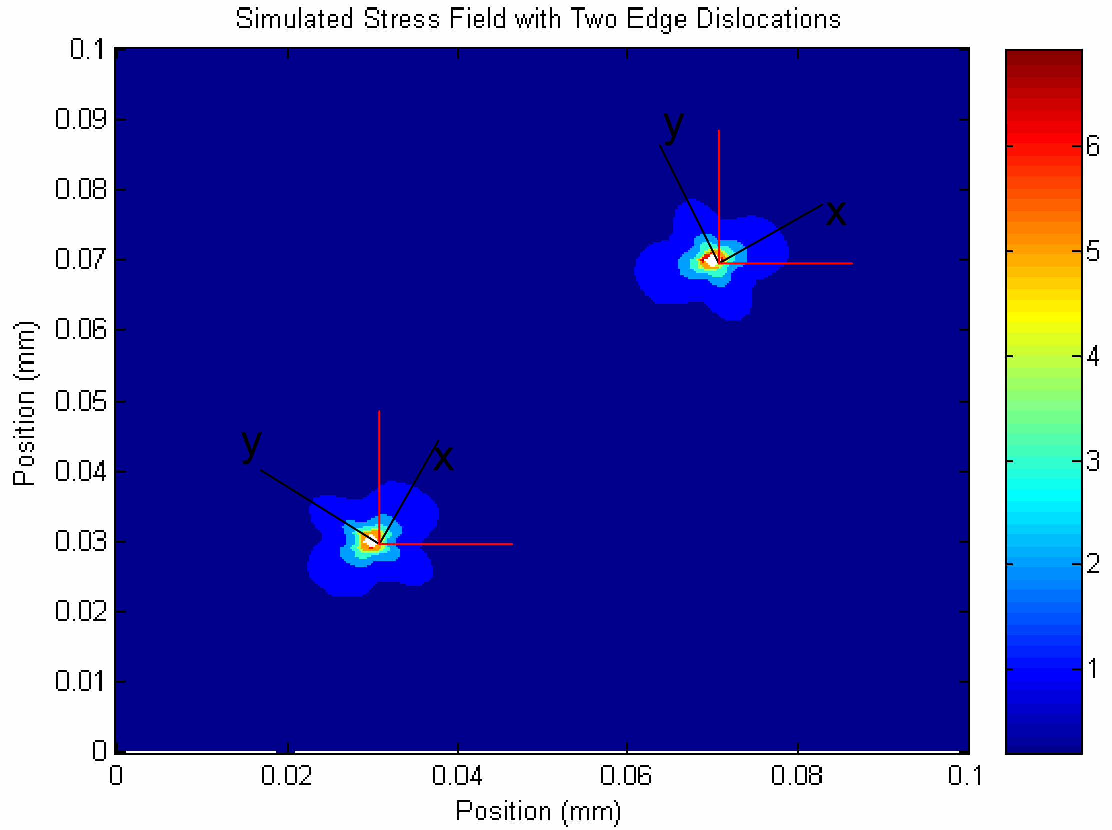

Figure 32: Stress field of two edge dislocations with different rotation. Local stress fields must be transformed to conform to the global axis (red lines).

$$\sigma_{x1} = \frac{\sigma_x + \sigma_y}{2} + \frac{\sigma_x - \sigma_y}{2}\cos 2\theta + \tau_{xy}\sin 2\theta \tag{10}$$

$$\sigma_{y1} = \frac{\sigma_x + \sigma_y}{2} - \frac{\sigma_x - \sigma_y}{2}\cos 2\theta - \tau_{xy}\sin 2\theta \tag{11}$$

$$\tau_{x1y1} = -\frac{\sigma_x - \sigma_y}{2}\sin 2\theta + \tau_{xy}\cos 2\theta \tag{12}$$

Each dislocation has the three stress components from its stress field transformed into the major axis. Each pixel adds up all the contribution from the stress fields given by each dislocation. Three stress fields are created; one for each stress component and Equation 9 is used to utilize the three stress fields to find the final stress field containing the maximum shear stress.

The theoretical value of average dislocation induced maximum shear stress must be averaged over an area with a specified dislocation density in order to be compared with the polariscope results. For each iteration, a value of dislocation density is implemented into the Matlab program to obtain the average maximum shear stress of the area. Figure 33 shows a flowchart of the steps taken to calculate the average maximum shear stress.

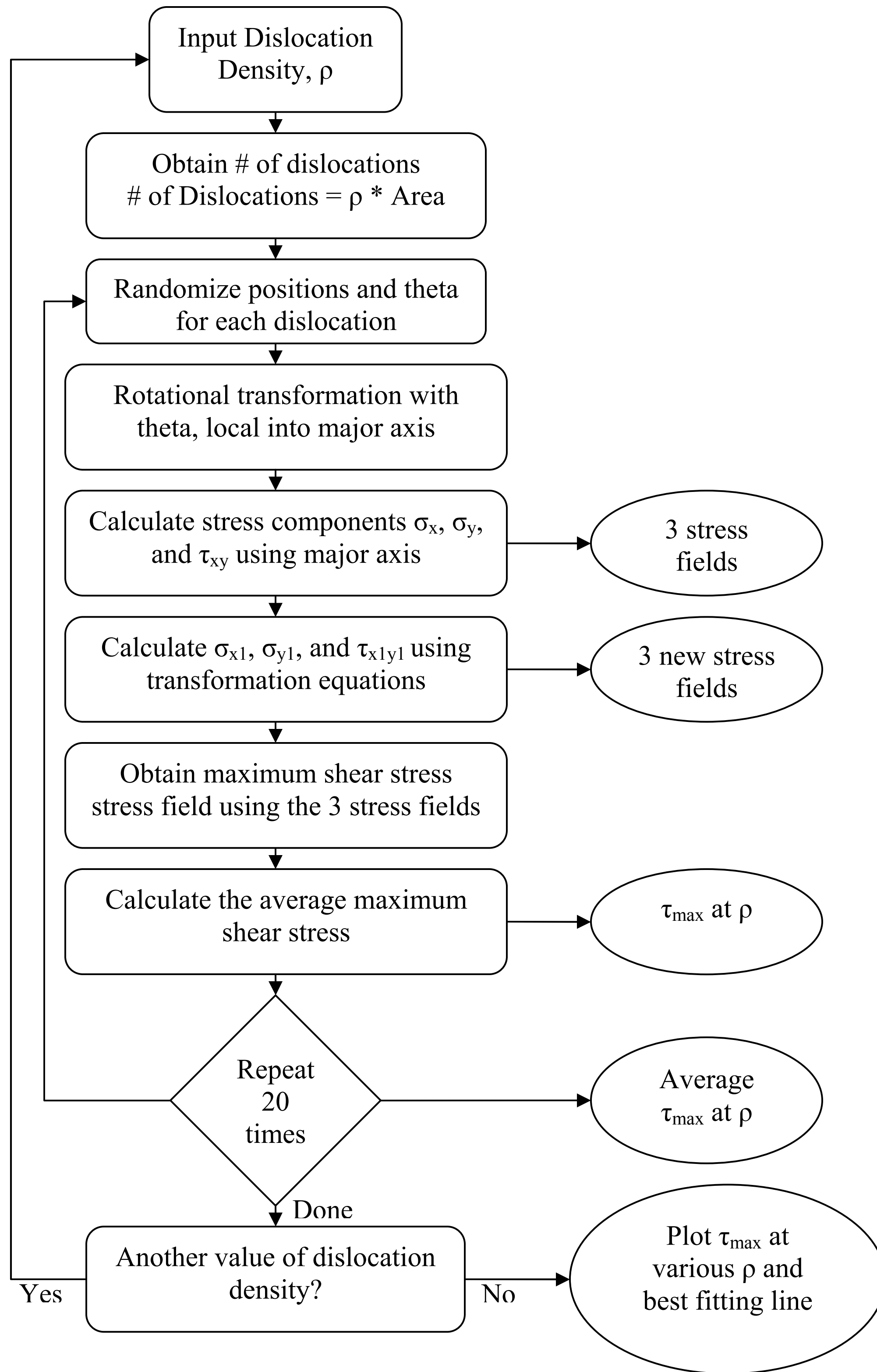

Figure 33: Flowchart describing the steps taken to obtain the model describing the average maximum shear stress for a dislocation density

Figures 34 and 35 the results of the simulated stress field of an area with a specific value of dislocation density.

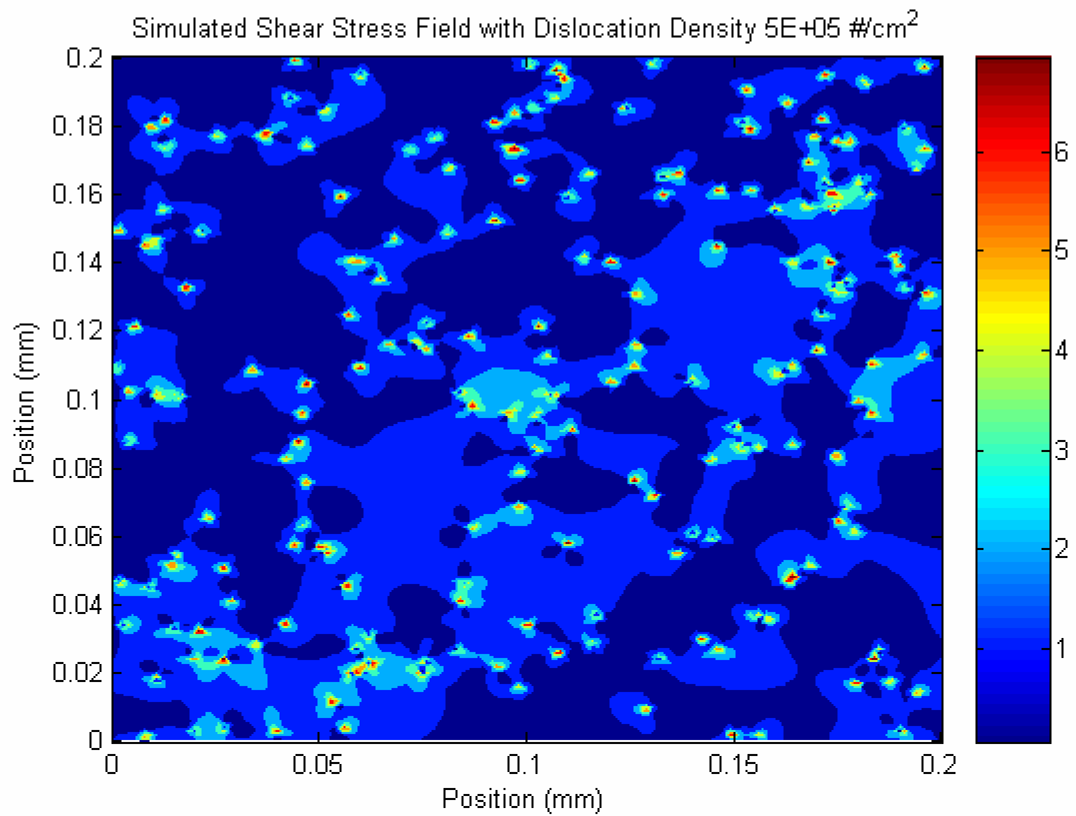

Figure 34: Absolute Stress Field (Color bar in MPa) of an Area 200 x 200 Micron With Dislocation Density of 5 x 10^5 /cm^2, Average Stress: 1.13MPa

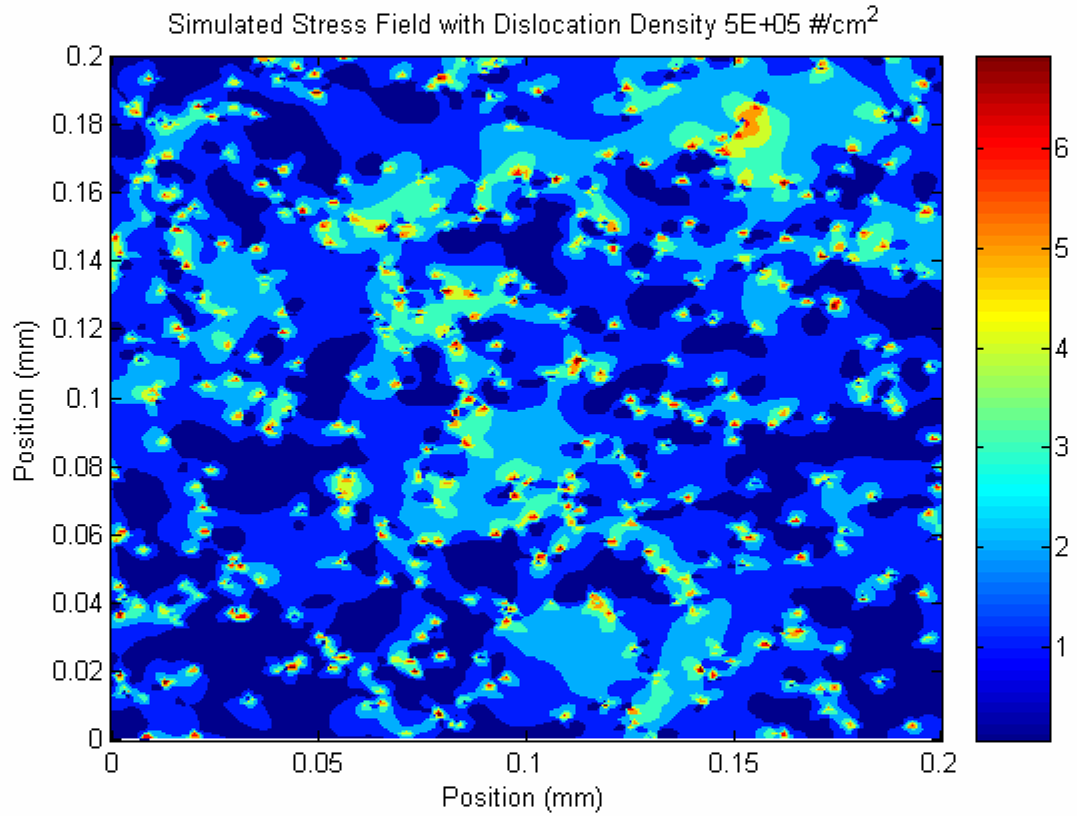

Figure 35: Absolute Stress Field (Color bar in MPa) of an Area 200 x 200 Micron Area With Dislocation Density of 1 x 10^6 /cm^2, Average Stress: 1.71MPa

The simulated stress fields were calculated for numerous dislocation densities ranging 10^4 to 10^6 dislocations/cm^2. The results and best fitting line are seen in Fig. 36.

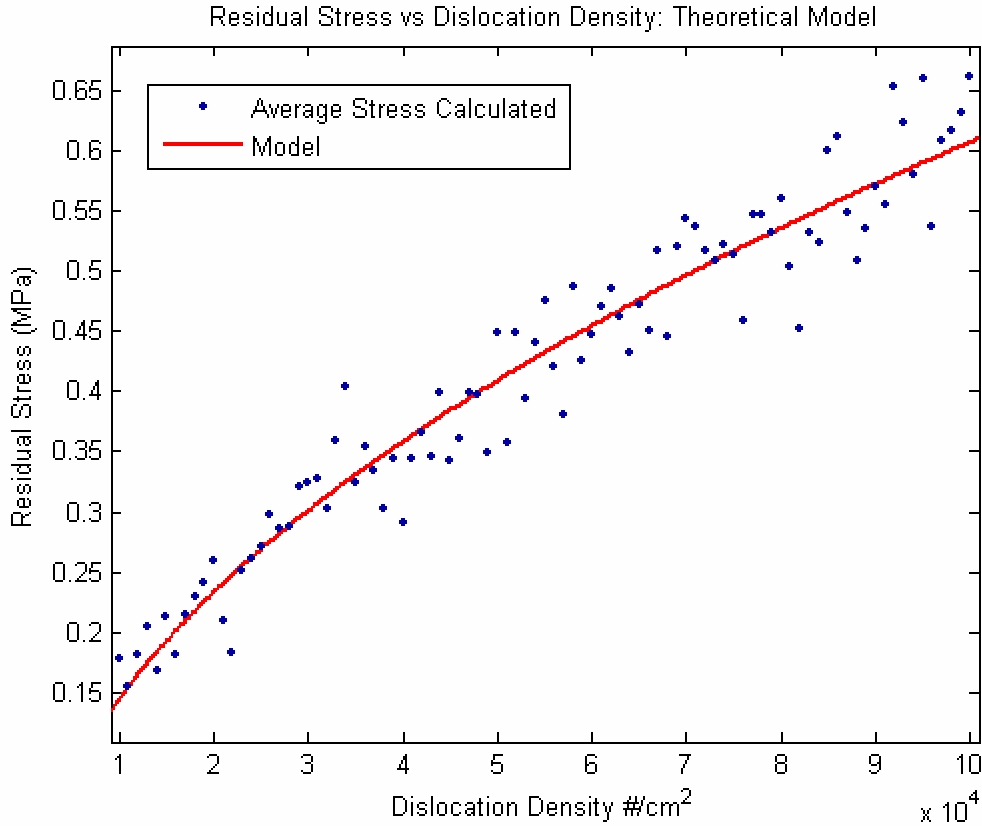

Figure 36: Theoretical Maximum Shear Stress vs Dislocation Density. Max shear stress is obtained from simulated stress fields.

The average of residual stress over the area of the simulated field was calculated for each dislocation density and a relationship was found in Eq. (13)

$$\sigma = K\mu b\sqrt{\rho} \qquad (13)$$

The variables are the Burgers vector *b*=3.84Å, the shear modulus μ=65GPa, and the constant K=0.68, calculated from the Matlab simulations. σ represents the residual stress caused by dislocations. It should be noted that Equation 13 is similar to Taylor's equation

[51] as a form of flow stress caused by dislocation interaction, describing work hardening.

As shear stress reaches the critical resolved shear stress (CRSS), dislocations may propagate, bringing localized stress relief. The critical shear stress required to move a dislocation is [52, 53]:

$$\sigma = \frac{2\mu}{(1-\nu)}\exp\left(-\frac{2\pi a}{(1-\nu)b}\right) \qquad (14)$$

Values used for a and b were represented by the distance between the lattice planes parallel to the slip plane and the magnitude of the Burgers vector respectively. Since dislocations have the slip system {111}<110>, a is taken to be the distance between {111} planes, which is $a_0/\sqrt{3}$ and b is taken to be is $a_0/$<110>, i.e. $a_0/\sqrt{2}$. a_0 is the lattice spacing in silicon. In the case of silicon, the values used are: μ=65GPa, ν=.28, a=3.13 Å, b=3.84Å resulting in a CRSS value of 145MPa. This value only can be reached during high temperatures near the silicon solid-melt interface. The temperature profile must be known in order to see if stresses have reached the CRSS for dislocation multiplication and/or propagation.

5.2 Case 2 – Stress Relaxation

The positive relationship does not apply to areas where stress relaxation has occurred, producing a need for another explanation. Stress relaxation occurs when shear stresses acting on a slip plane exceed the critical value. Propagation of dislocations

occurs along with stress relief. Even though there is stress caused by dislocations, the stress relief overwhelms the stress caused by new dislocations. There have been models to explain this behavior, but these are strain rate and temperature dependent. There are no known models to explain the values of dislocation density and residual stress after stress relaxation. A model will be created from data analysis.

A random variation in both residual stress and dislocation density was seen across the EFG wafers, perpendicular to the growth. Line C contains 3 times more data points than the other lines and has the largest range of both dislocation density and residual stress. Instead of accumulating data from all the lines and finding the best fitting model, only the data from Line C was used to find the best fitting model. The equation from the best fitting model will then be applied to the other data sets. If the equation explains the other data sets reasonably well, it shows applicability of the model. Dislocation density was plotted against the corresponding residual stress to find the relationship and can be seen in Fig. 37.

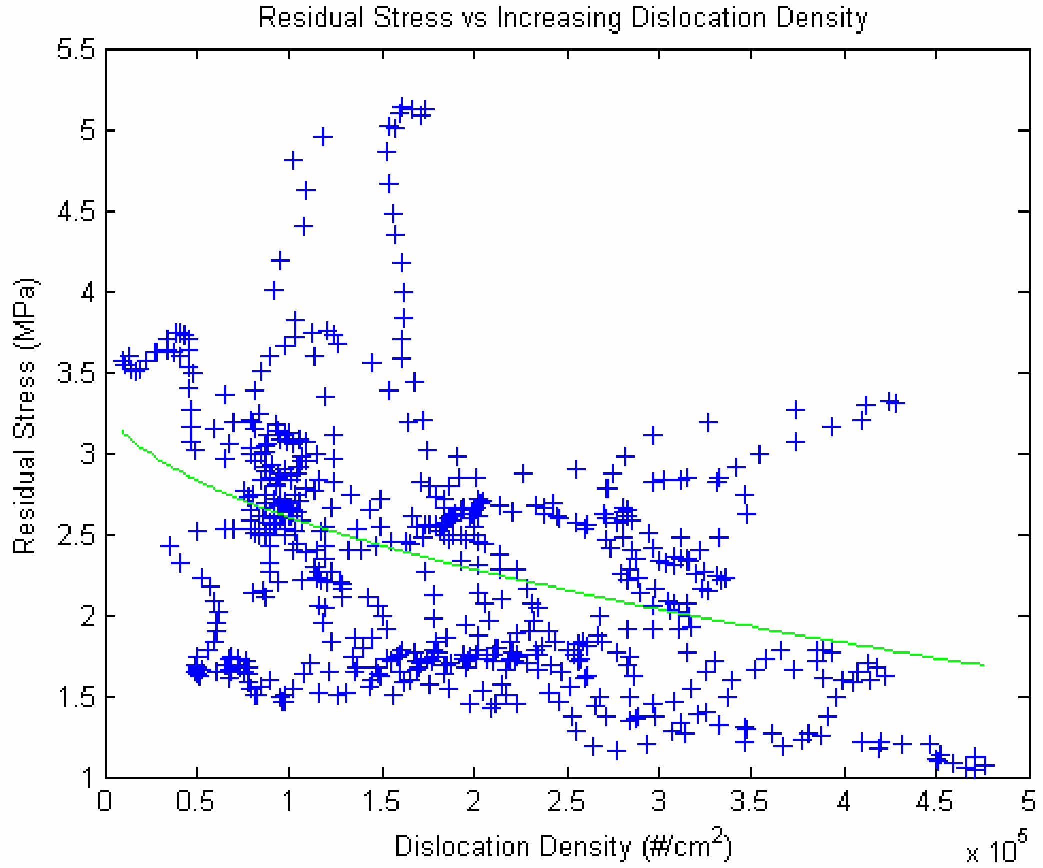

Figure 37: Experimental data plotted with increasing dislocation density

The graph shows large variations due to other sources of residual stress. However, a least squares fitting was applied to obtain the general equation for further analysis. Equation 15 was found to be the best fitting line to explain the experimental data behavior.

$$\sigma = -A\mu b\sqrt{\rho} + \sigma_0 \qquad (15)$$

μ is the shear modulus, b is the modulus of Burgers vector, and *A* is a constant caused by unknown sources. Residual stress not caused by dislocation density in addition to original stress immediate before stress relaxation is represented by σ_0. Combining Equation 15

(after stress relaxation) and Equation 13 (dislocation induced stress) gives a more complete description of dislocation density's effect on residual stress. A graph visualizing both equations can be seen in Fig. 38, which is a combination of Fig 36 and 37. A red box is placed at the intersection to represent the uncertainty of the point of stress relaxation, which is not solely a function of dislocation density.

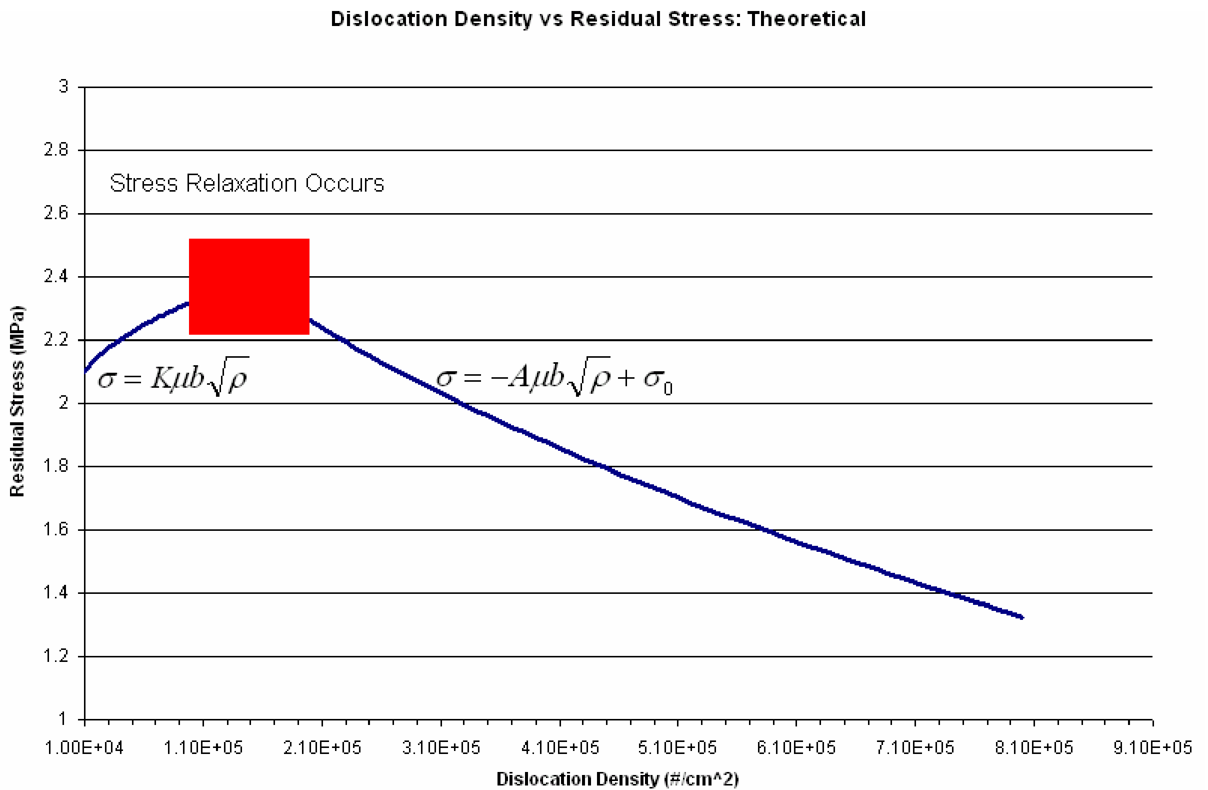

Figure 38: Residual stress model based on dislocation density. Model consists of positive and negative relationship based on Eqs 13 and 15.

Using a constant *A*, there is a 52% correlation and an average of 25% deviation of the experimental data from the model. Assuming A is constant for each type of etch pit, A_R=1.56, A_E=1.48, the results of how well the data conforms to Equation 15 are summarized in Table 4. A R-square value of 1 represents a perfect fit. The values of A

were found using the best fitting line of Line C. Line 20 is not in the table since the etch pits were not categorized into round or elliptical shapes.

Table 4: Correlation by Type of Etch Pit

		R-Square	
Type of Etch Pit	A	Line C	Line 10
Round	1.56	.19	.23
Elliptical	1.48	.26	.17

A comparison of the experimental and theoretical model using a constant A for all lines can be seen in Appendix for round and elliptical etch pits. The R-square values are low because *A* is assumed to be constant. Figure 35 shows large deviations from the model and a possible reason is that *A* in Equation 15 is variable. A constant *A* is not realistic and may be a factor of an unknown source that influences the behavior of dislocations, such as orientation, oxygen impurities, dopants, and other defects. To get a clearer idea of the range of A, the data for all the lines were cut up piecewise to get a simple curve to do least squares fitting using Eq. 16, a more generalized form of Eq. 15 and Eq. 13.

$$\sigma = C_1 \mu b \sqrt{\rho} + C_2 \qquad (16)$$

This would allow an adjustable C_1 (representing either K or A from Eq. 13 and Eq. 15, respectively) to be used for each piece of data. The local stress peaks were used as the start and end of each piece of data. An example can be visualized in Fig. 39. Similar graphs for all other lines can be found in the Appendix.

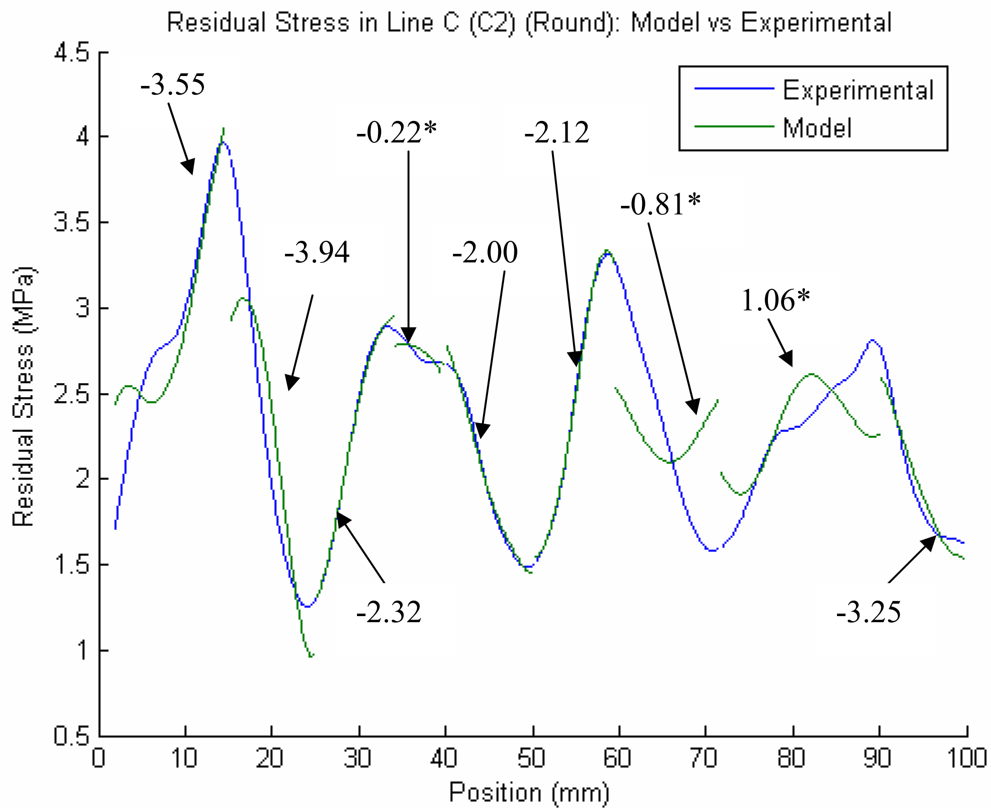

Figure 39: Model vs Experimental by Piecewise (Adjusted C_1 shown for each section). A negative number indicates Eq. 15 while for positive, it is Eq. 13. * = less than 95% statistical evidence of correlation.

The only difference between Equation 13 and 15 is the sign of the constant, which allows us to apply Eq. 16 to both positive and negative relationships. The sign of the adjustable C_1 represents a positive or negative relationship. 75% of the data from all the lines fall under either a positive or negative relationship following Equation 16 with 90%

confidence with p-value of .02 or less. P-value is the probability of getting the observed correlation by random chance. A p-value of .05 or less shows statistically significant evidence that there is correlation [54].

CHAPTER VII: DISCUSSION

Equation 16 was applied to all data (lines and areas) with an adjustable C_1. Equation 16 allows the application of Equation 13 and 15 simultaneously to test for a positive (before stress relaxation), negative (after stress relaxation, or nonexistent relationship. Because the constant C_1 can vary, large lines or areas were cut up piecewise, about 8-15mm lengthwise each section, in order to apply different values for C_1. Each piece of the measured residual stress data was compared to the residual stress model (Eq. 16) based on the corresponding measured dislocation density. The methods used to obtain dislocation density for lines differ than those used for areas, therefore the results of lines and areas are kept separate.

7.1 Lines

The data for each line, Line 10, 20, and C, was cut up piecewise and Eq. 16 was applied to each piece with the best fitting C_1. The results for all lines are summarized in Table 5.

Table 5: Summarized Results for Lines with Variable C_1

a)

% of Data Positive – Before Stress Relaxation (90% confidence)	13
Range of C_1 (or K)	1.26 − .66
Range of Stress (MPa)	1.88 − 1.61
Range of Disl. (#/cm^2)	2.94E+05 − 9.26E+04
Deviation from Model (%)	Avg: 0.2% Max: 0.3%

b)

% of Data Negative – After Stress Relaxation (90% confidence)	62
Range of C_1 (or A)	-.18 − -16.98
Range of Stress (MPa)	3.15 − 1.81
Range of Disl. (#/cm^2)	6.33E+05 – 1.30E+05
Deviation from Model (%)	Avg: 3% Max: 15%

c)

% of Data Unexplained (less than 90% confidence)	25

The percentage of the data that does not fit into either positive or negative model which is 25% (Table 5c) shows that dislocation density does have a predominant effect but is not the only source for residual stress.

For the positive relationship (Table 5a), the range of C_1 (or K) has a relatively nominal distribution around 1, which is close to the value of K=.68 in Equation (13), verifying the dislocation induced stress (before stress relaxation) model. The deviation of the experimental data from the positive model is very small, having no more than 0.3%. The range of dislocation density is found below 3E+05 disl./cm^2 for the positive relationship while the range for the negative relationship is found above 1E+05 disl/cm^2. This verifies that stress relaxation occurs at higher dislocation density. Based on the

experimental data, the dislocation density where stress relaxation occurs is at 1-3E+05 dislocations/cm^2. This is also seen in Table 2, where the positive correlation only occurs below 3E+05 disl./ cm^2 while the negative correlation only occurs above 1E+05 disl./ cm^2.

As for the negative relationship (Table 5b), there is a larger range of C_1 (or A) that has an average of 8.6 with a standard deviation of 4. The deviation of experimental data from the negative model is reasonable, having an average of 3%. An increase of percentage of negative linear data that fall under 90% confidence occurred after the omitting of data from the first 5mm at the edge. The increase indicates a strong positive relationship at the edges of the wafer, showing high stress along with high dislocation density.

7.2 Areas

The model based on Eq. 15 can only be applied on a one dimension axis across the wafer. It is possible to extend it to accommodate 2D areas. However, since dislocation density generally stays constant on the y direction (parallel to the growth), as shown in Fig. 13 and the residual maps of areas, any variation in residual stress is due to unknown source for which there is no experimental data. For this reason, lines perpendicular to the growth were extracted from the 4 areas previously mentioned so that the model can be applied.

Since the lines from the areas are too small (less than 10mm) to be cut up piecewise, the whole length of the lines is compared to the model. The results of the lines

from the areas are summarized in Table 6. Area 2 was not subjected to analysis due to hypothesis testing resulting in evidence of no correlation between dislocation density and residual stress.

Table 6: Summarized Results for Areas with Variable C_1

a)

% of Data Positive – Before Stress Relaxation (90% confidence)	64
Range of C_1 (or K)	244.89 – 1.57
Range of Stress (MPa)	9.29 – 5.28
Range of Disl. (#/cm^2)	8.96E+04 − 7.27E+03
Deviation from Model (%)	Avg: 1% Max: 12%

b)

% of Data Negative – After Stress Relaxation (90% confidence)	33
Range of C_1 (or A)	-8.51 – -205.8
Range of Stress (MPa)	11.02 – 2.00
Range of Disl. (#/cm^2)	2.23E+05 – 1.39E+04
Deviation from Model (%)	Avg: 4% Max: 32%

c)

% of Data Unexplained (less than 90% confidence)	2

The range of C_1 for both relationships is much larger than listed in Table 4 for Lines A, B, and C. This is largely contributed to the inaccuracy in the magnitude of dislocation density, due to undercounting etch pits and error in the black and white conversion. However, the model based on Eq. 16 has explained nearly 98% of the data's behavior (Table 6c) even though the magnitude of the model does not match up with

those of the experimental data as can be seen in the maximum values of the deviation from model in Table 6a and 6b. A large range of C_1 is not expected for this model since it is unreasonable that any factor affecting dislocation interaction would intensify the behavior by more than 10 orders of magnitude. The areas show more of a positive linear relationship than in the lines. In both Table 4 and 6, the highest values of dislocation density (greater than ~2E+05 #/cm^2) are only found in negative relationship (after stress relaxation).

CHAPTER VIII: CONCLUSIONS

The relationship between dislocation density and residual stress has been examined. Several conclusions have been achieved and will be discussed in the bulletin points. The first 3 are the most important conclusions.

1) Dislocation density has a mainly negative square root relationship, $\sigma = -A\mu b\sqrt{\rho} + \sigma_0$, with residual stress in EFG wafers which contain about 10^4 to 10^6 dislocations/cm^2.

2) The range of the critical value of dislocation density that indicates stress relaxation is 1-3E+05.

3) The positive model $\sigma = K\mu b\sqrt{\rho}$ can explain dislocation induced residual stress very well.

4) Orientation differs across EFG wafers, perpendicular to the growth. Orientation is a possible factor in A for the negative relationship (after stress relaxation).

5) Over 85% of the data fits both models (with varying C_1) with 90% confidence with alpha less than .02.

6) Elliptical etch pits were consistently found to have a slightly higher effect on correlation to residual stress than round etch pits, but there is not enough statistical proof.

7) Areas that are up to 5mm from the edges have a strong positive correlation between dislocation density and residual stress.

8) Dislocation density stays relatively constant along the growth of EFG wafers. Residual stress has some discrepancies along growth, suggesting other unknown sources.

9) The range for the variable A in the negative linear model is relatively small and defined. The model can be extended to include A as a function of an unknown source.

CHAPTER IX: RECOMMENDATIONS

To strengthen the statistical evidence of the model, there needs to be an image analyzing software that can successfully determine etch pit density over large areas. Since this paper only examined EFG wafers that had dislocation density in the range of $10^4 - 10^6$, a larger range of dislocation density must be examined in order to verify the critical final dislocation density to indicate stress relief during high temperatures.

The variable A in Eq. 15 is possibly a source of orientation and must be analyzed. In this thesis, an orientation of [110] was assumed for all measured areas to apply Equation 15. To further this study, the orientation of the exact same areas where the dislocation density and residual stress are measured must be determined.

Other possible sources of residual stress must be examined, such as oxygen and carbon concentrations, dopants, and other impurities. The residual stress caused by other sources can be implemented into the model (Eq. 15) as σ_0. It is also possible that the impurities can have an effect on dislocation interaction, thus influencing A.

APPENDIX A: Experimental Data - Residual Stress vs Dislocation Density

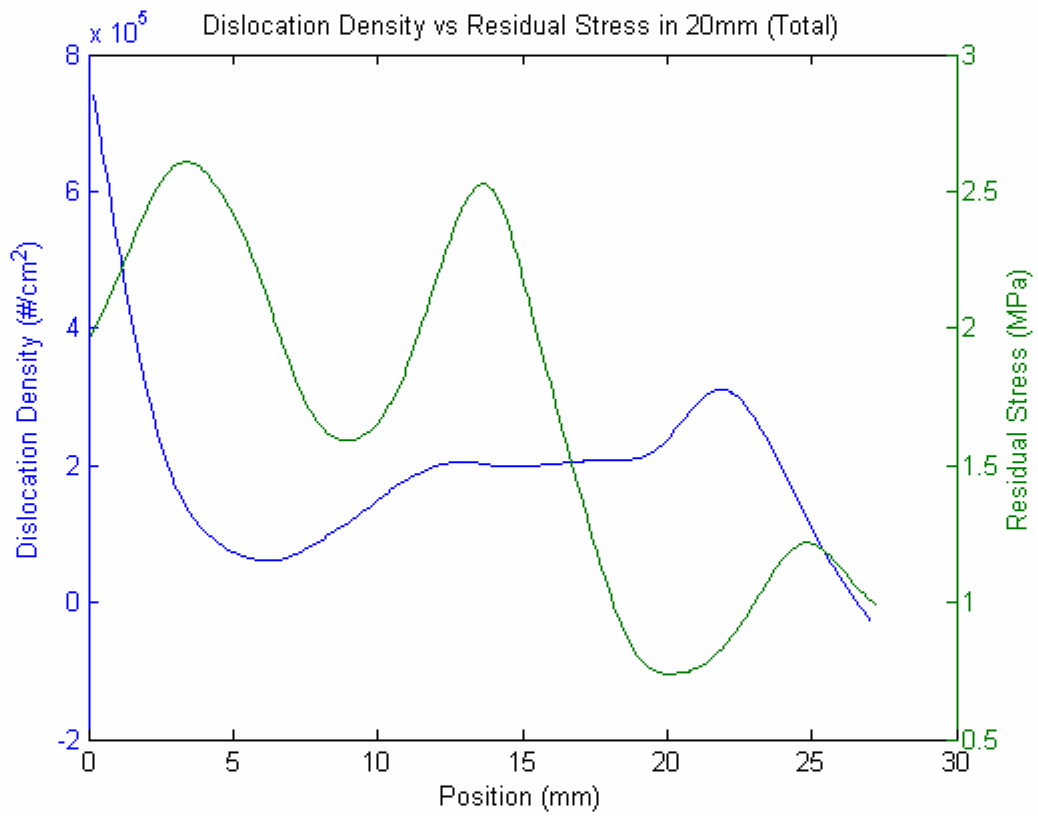

21% Correlation

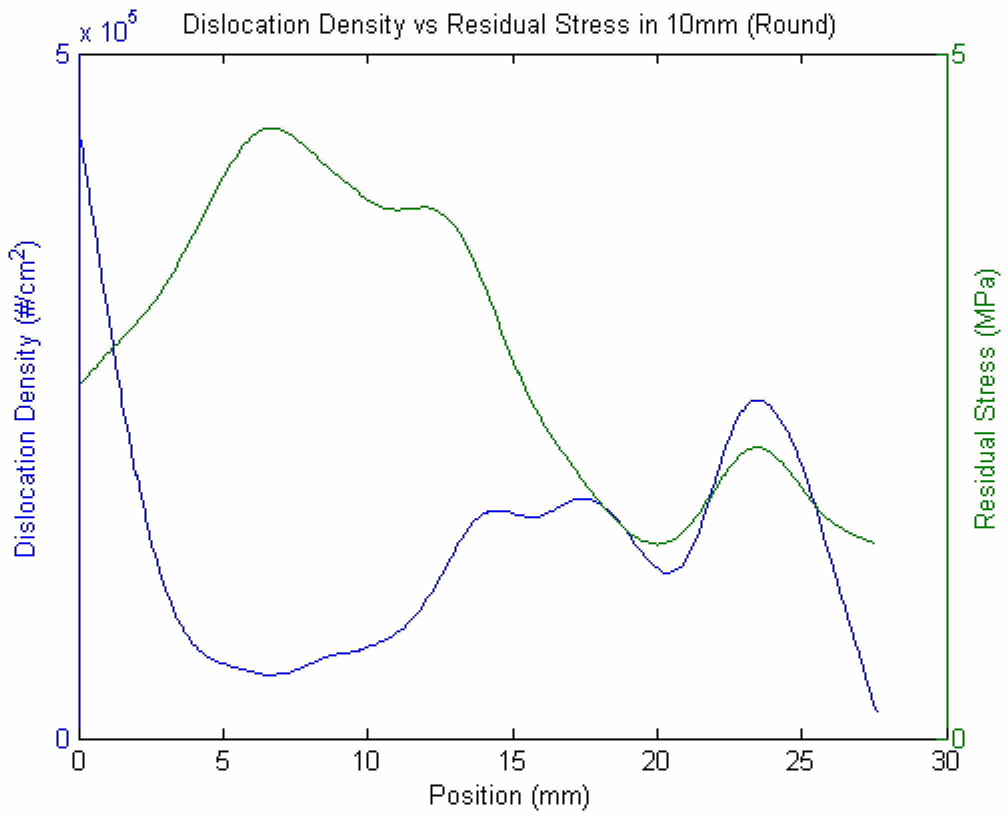

-20% Correlation

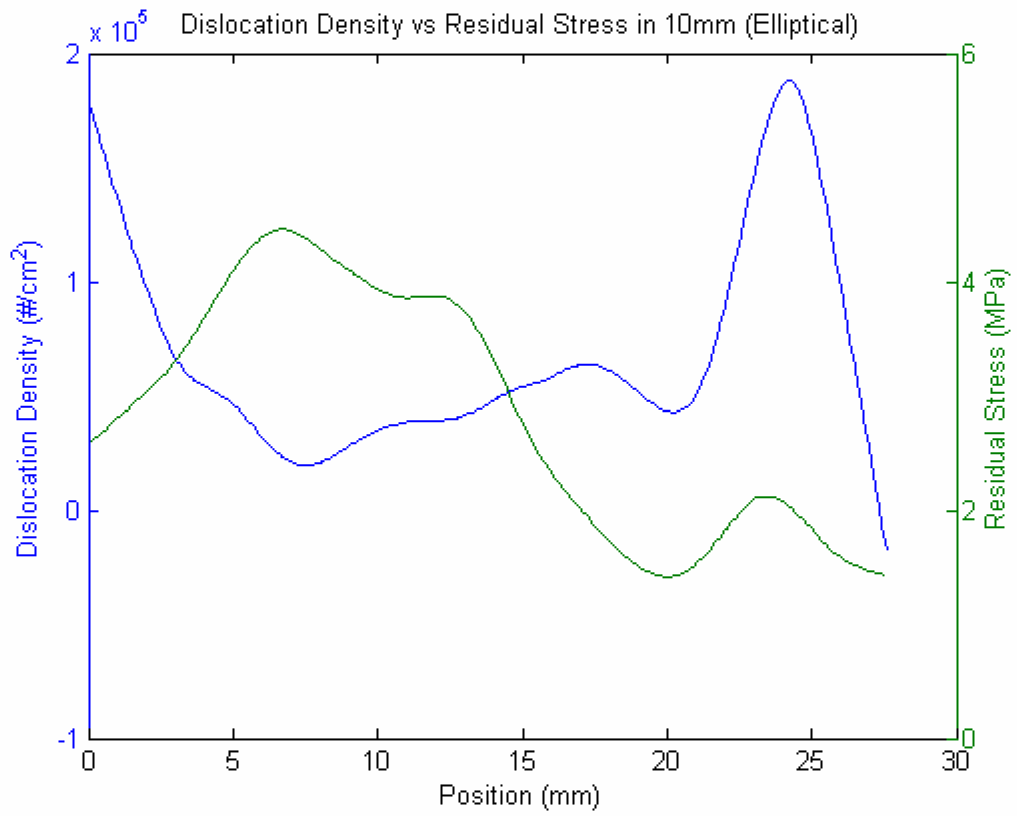

-18% Correlation

APPENDIX B: Residual Stress Modeling Using a Constant A

Models use the Equation # with a constant A and uses experimental dislocation density data.

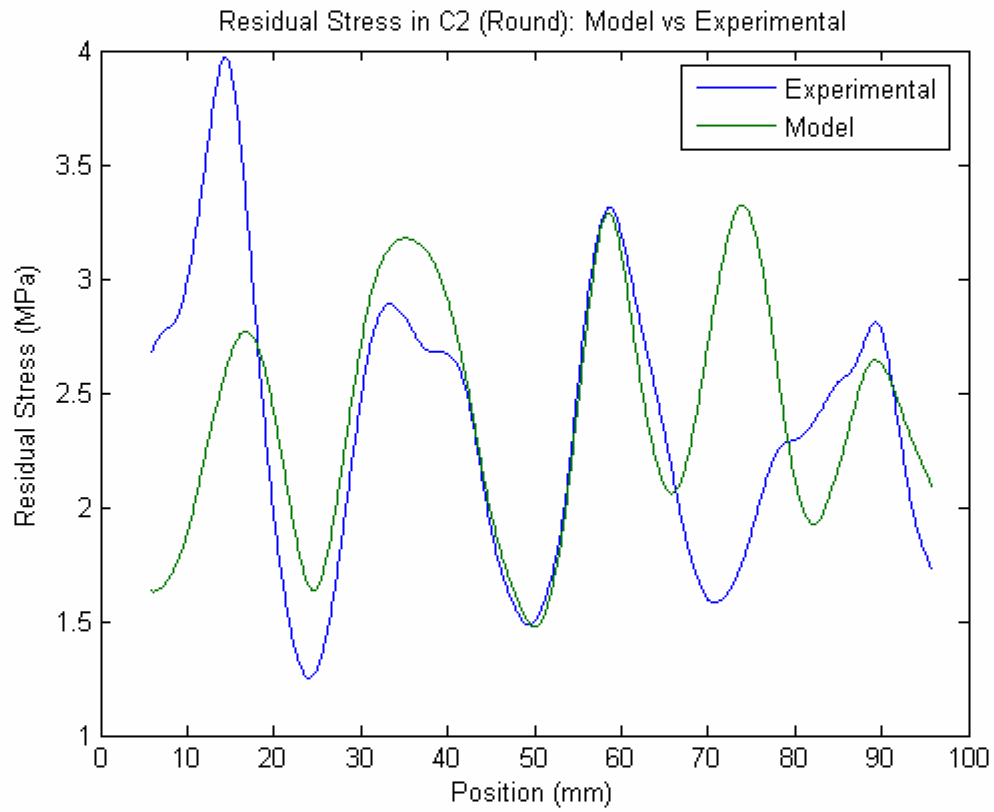

44% Correlation

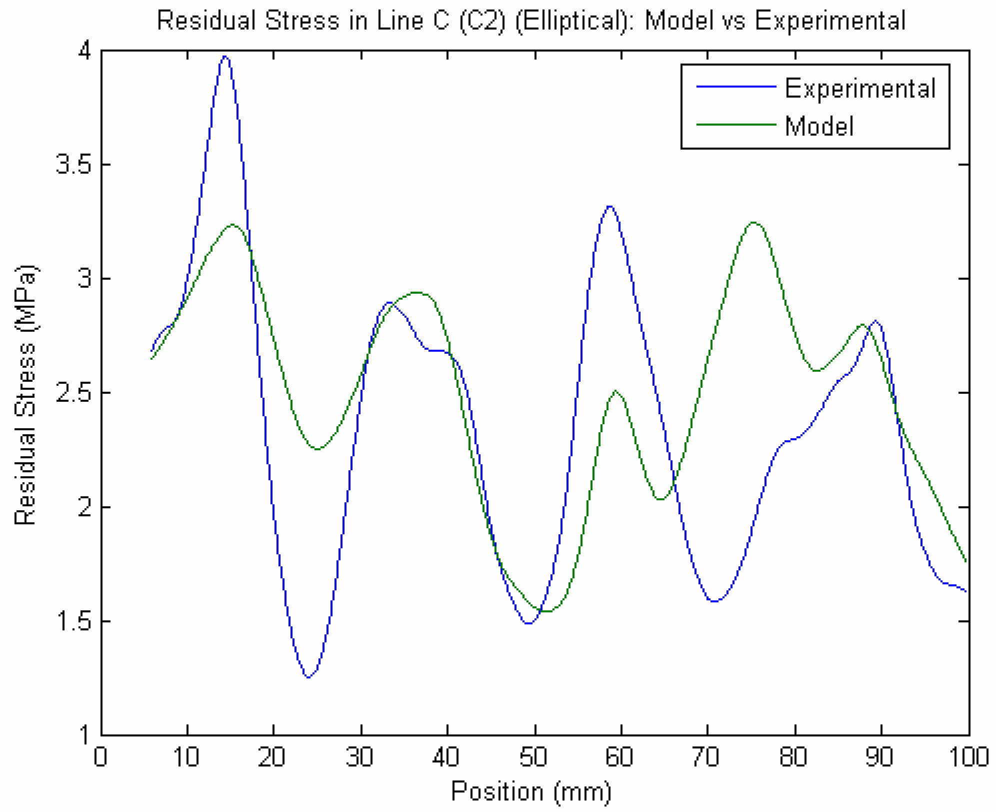

51% Correlation

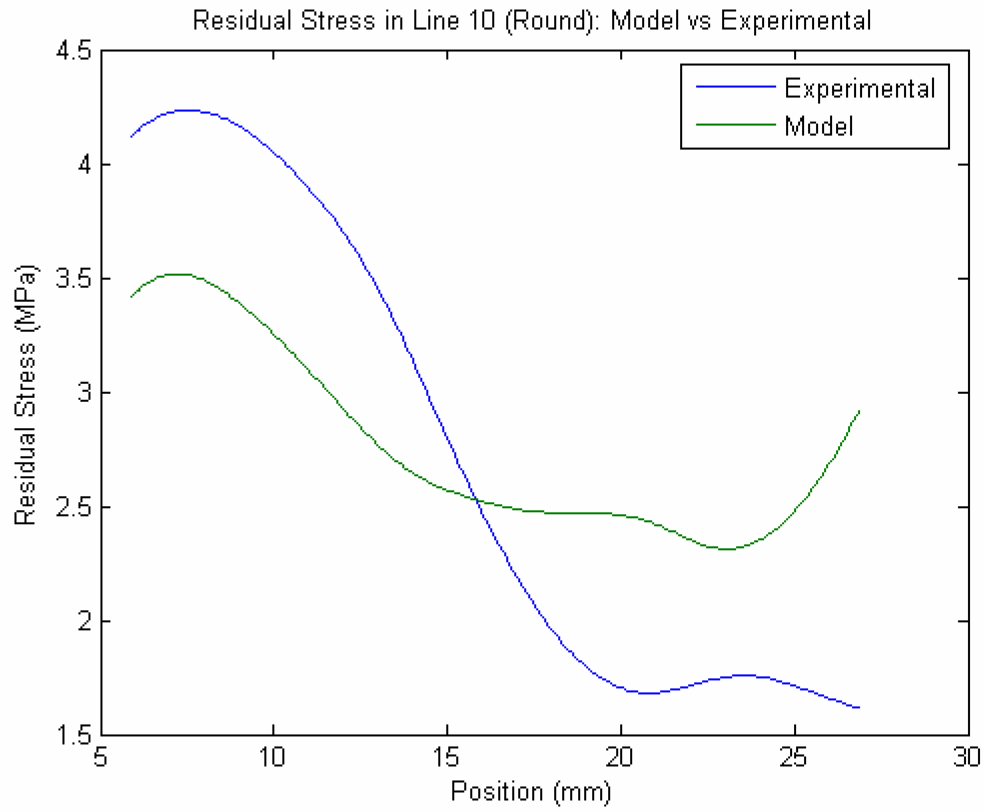

90% Correlation

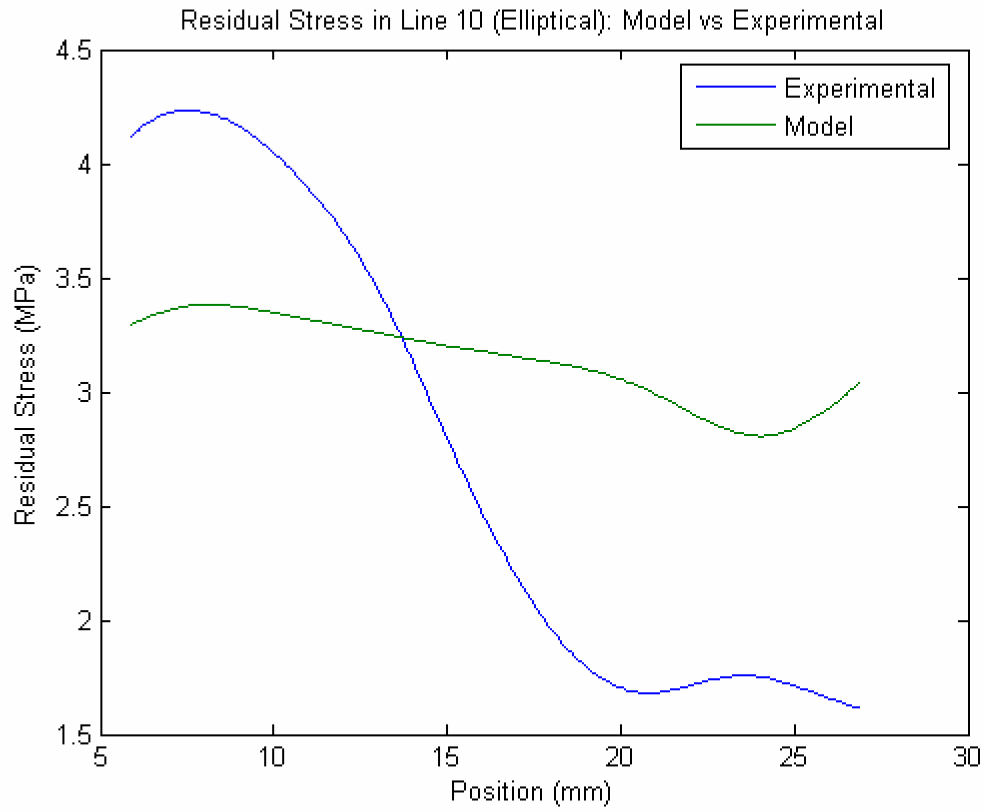

91% Correlation

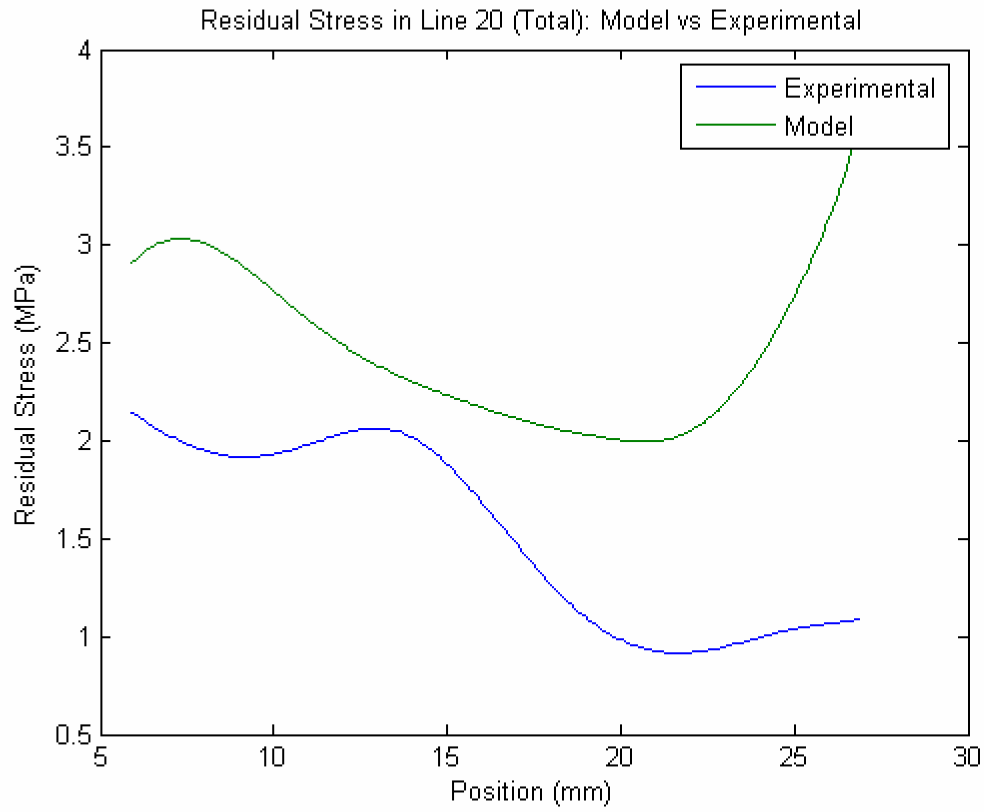

34% Correlation

APPENDIX C: Residual Stress Piecewise Modeling Using Variable A

Models use the Equation # with a variable A for each section and uses experimental dislocation density data.

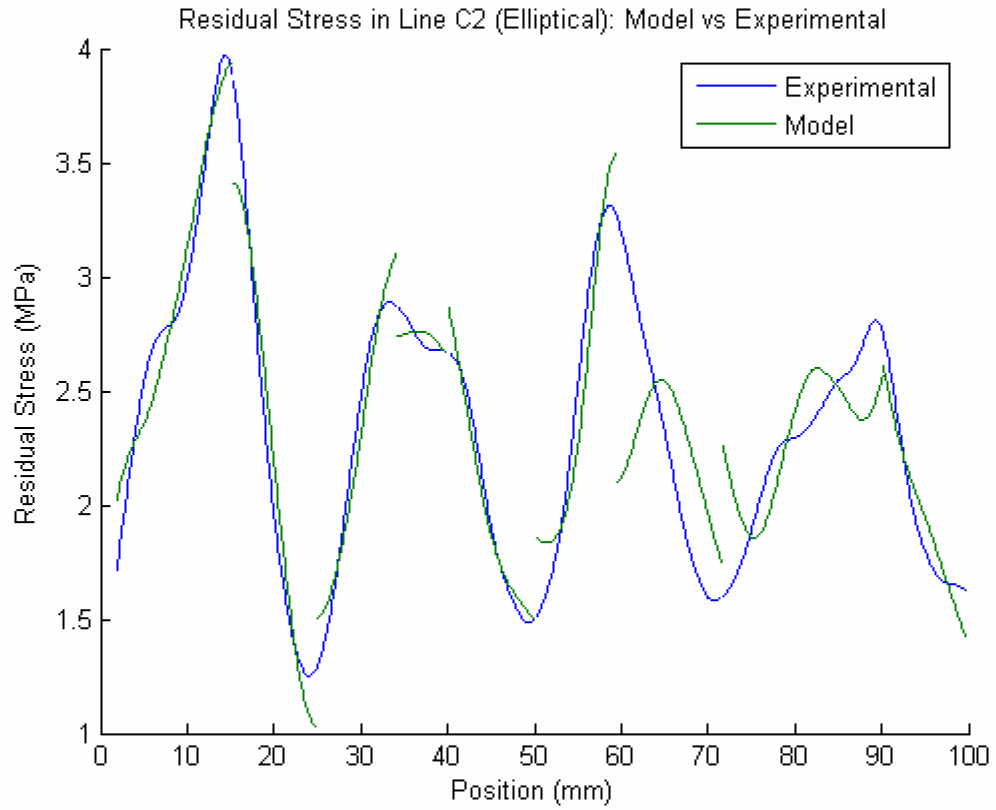

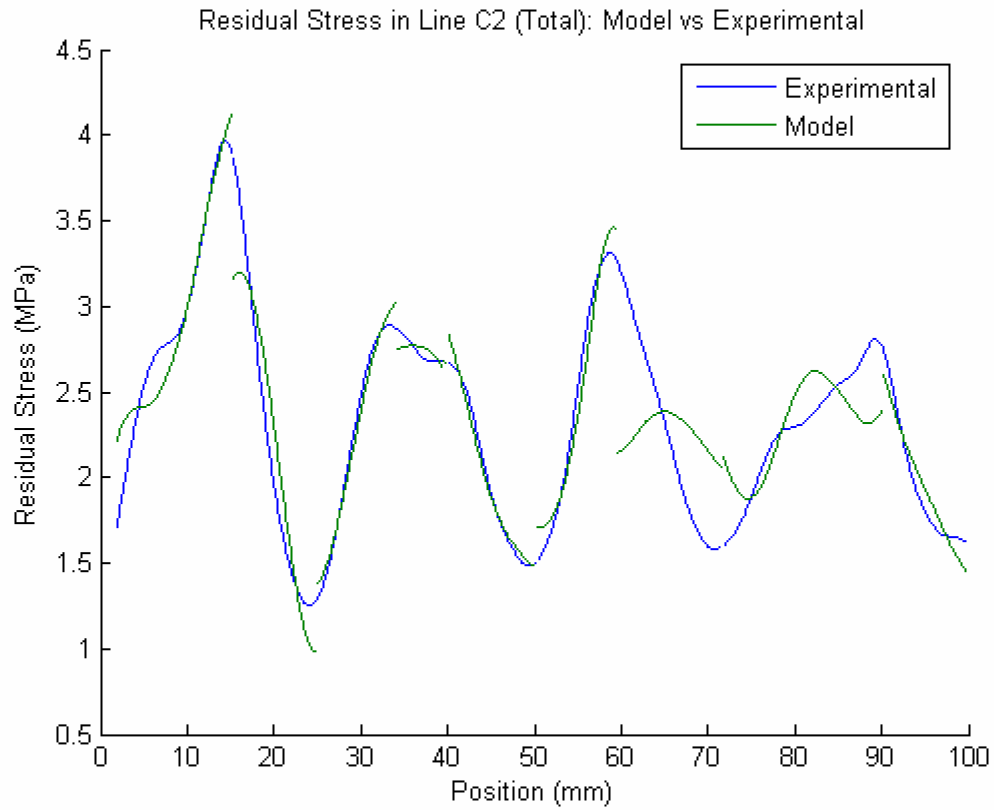
Residual Stress in Line C2 (Total): Model vs Experimental
Experimental
Model
Residual Stress (MPa)
Position (mm)
4.5
4
3.5
3
2.5
2
1.5
1
0.5
0
10
20
30
40
50
60
70
80
90
100

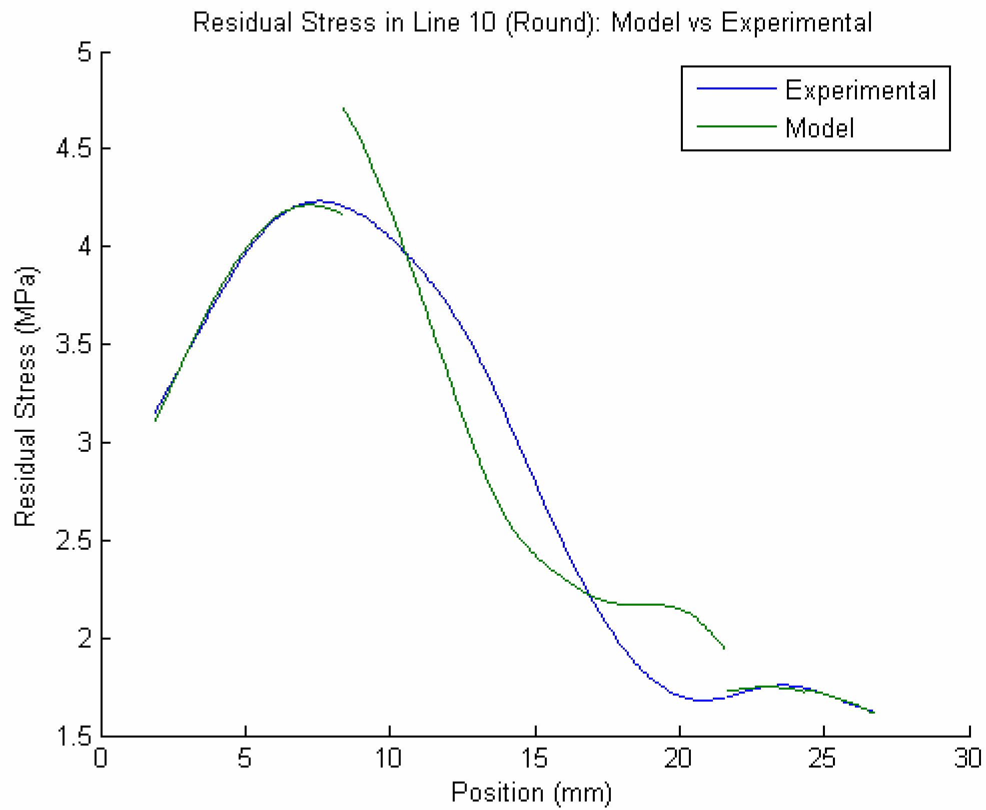
Residual Stress in Line 10 (Round): Model vs Experimental
Experimental
Model
Residual Stress (MPa)
Position (mm)
5
4.5
4
3.5
3
2.5
2
1.5
0
5
10
15
20
25
30

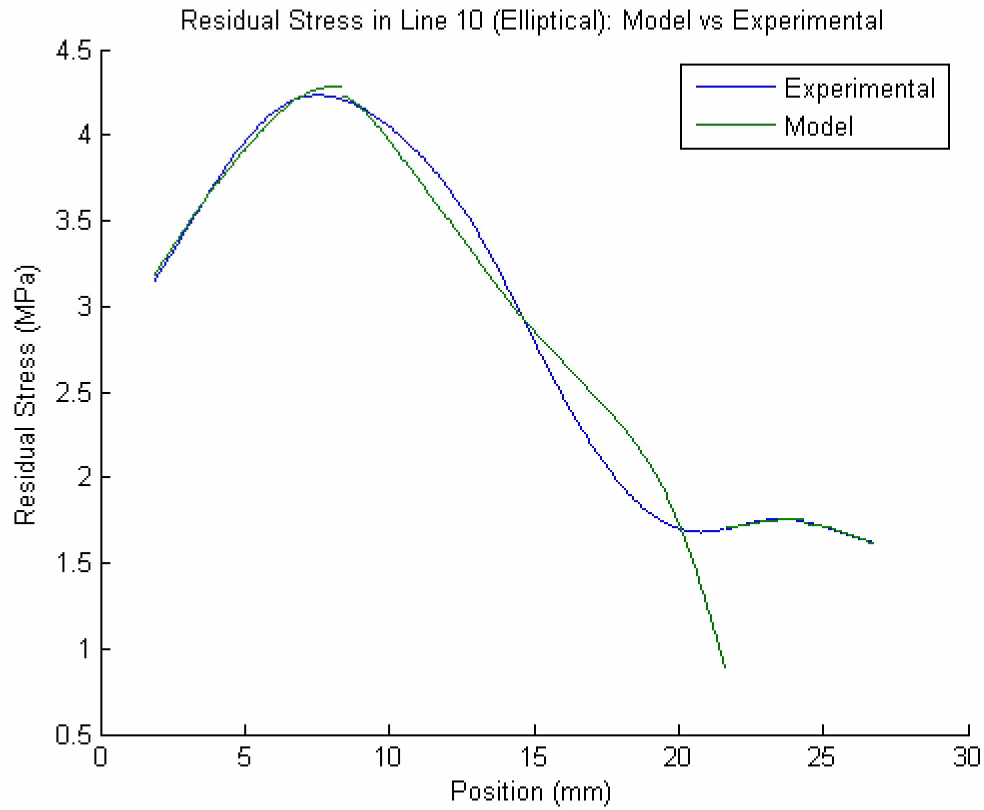
Residual Stress in Line 10 (Elliptical): Model vs Experimental
Experimental
Model
Residual Stress (MPa)
Position (mm)
4.5
4
3.5
3
2.5
2
1.5
1
0.5
0
5
10
15
20
25
30

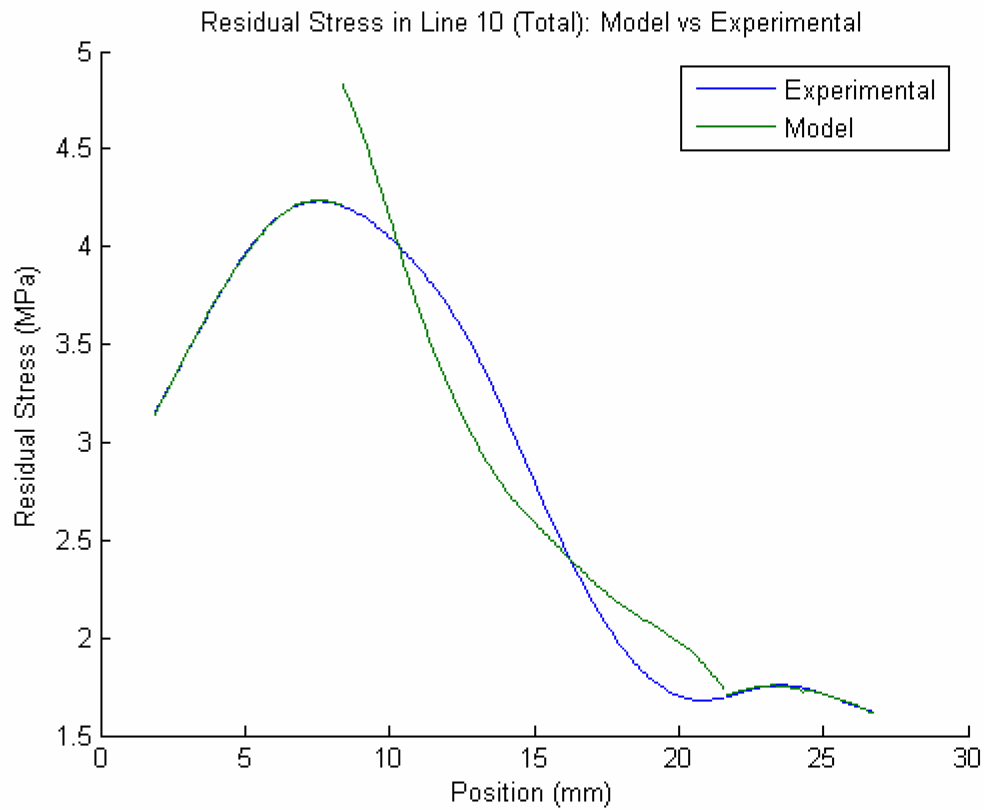
Residual Stress in Line 10 (Total): Model vs Experimental
Experimental
Model
Residual Stress (MPa)
Position (mm)
5
4.5
4
3.5
3
2.5
2
1.5
0
5
10
15
20
25
30

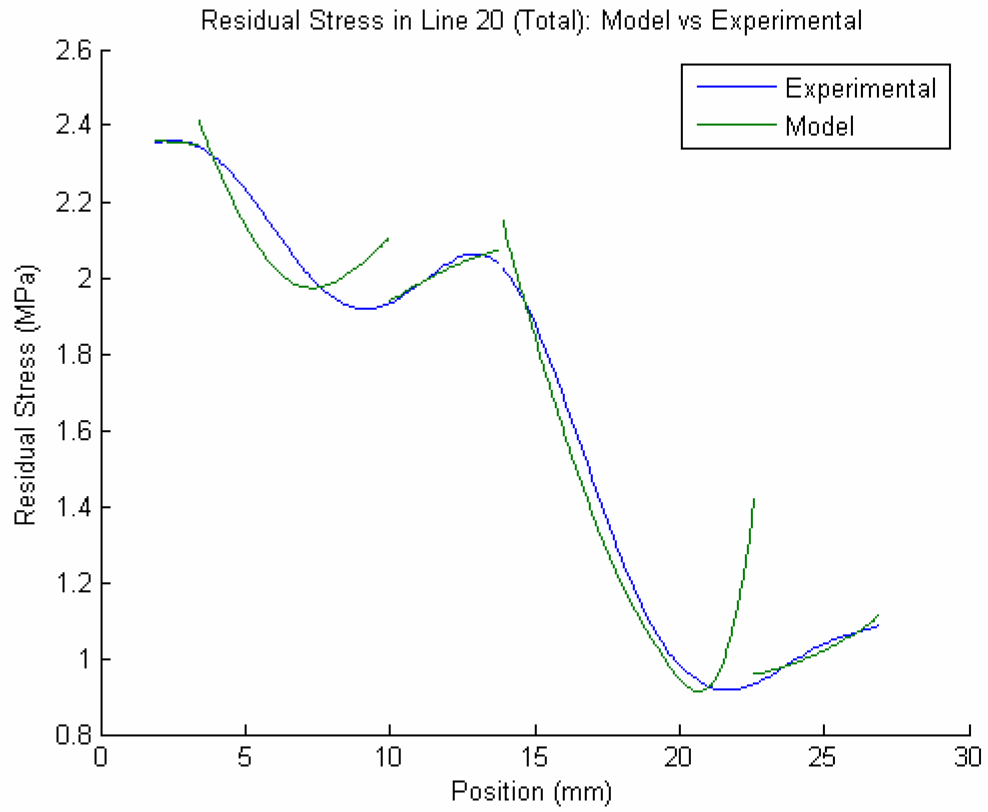
Residual Stress in Line 20 (Total): Model vs Experimental
Experimental
Model
Residual Stress (MPa)
Position (mm)
2.6
2.4
2.2
2
1.8
1.6
1.4
1.2
1
0.8
0
5
10
15
20
25
30

APPENDIX D: Laue Patterns of EFG Wafers

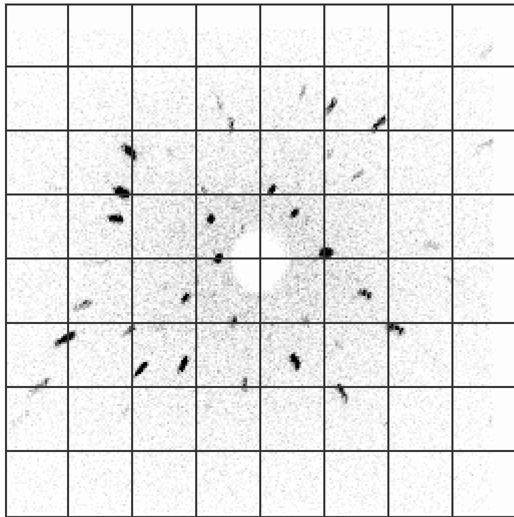

Wafer P - Grain 1

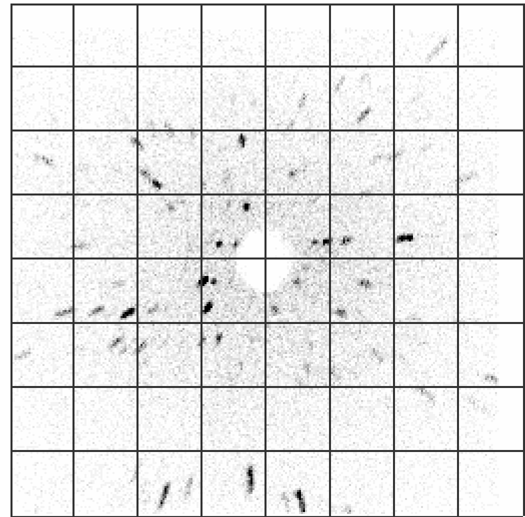

Wafer P - Grain 3

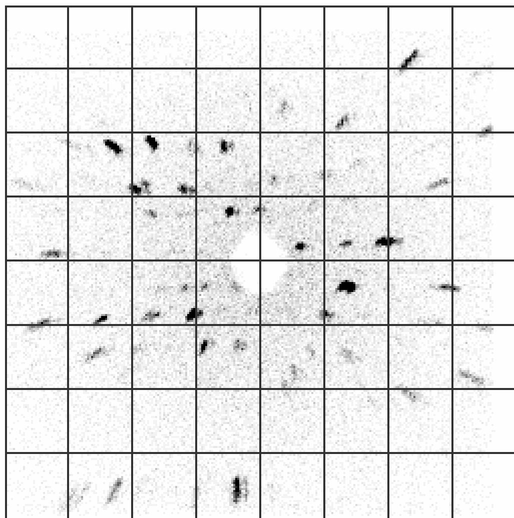

Wafer P - Grain 2

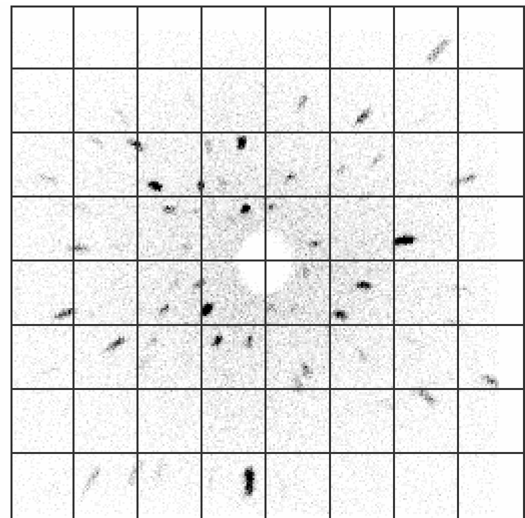

Wafer P - Grain 4

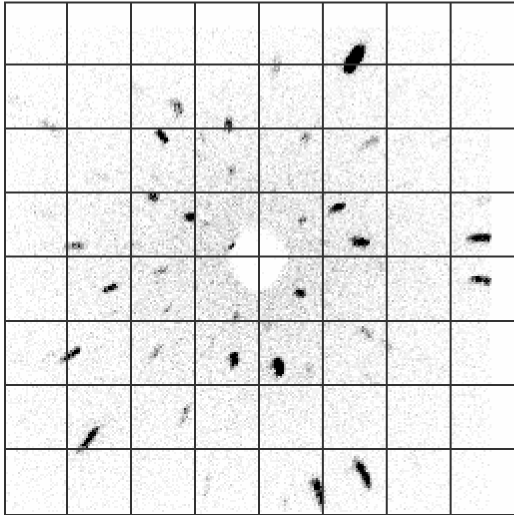

Wafer P - Grain 5

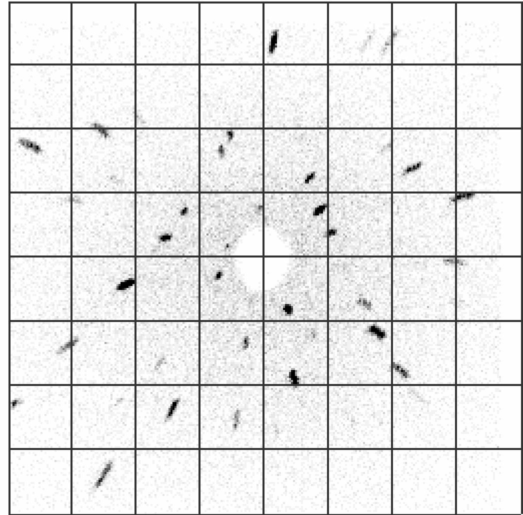

Wafer P - Grain 7

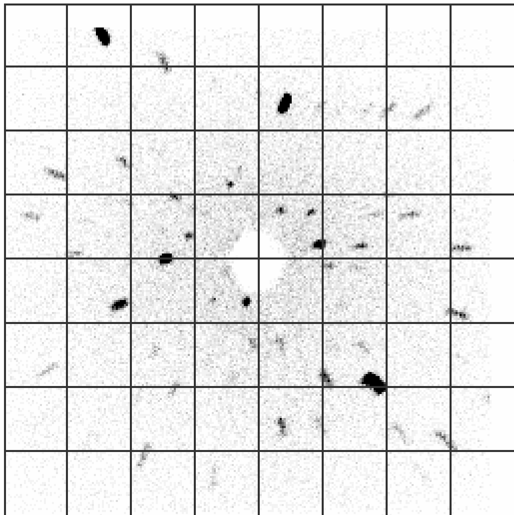

Wafer P - Grain 6

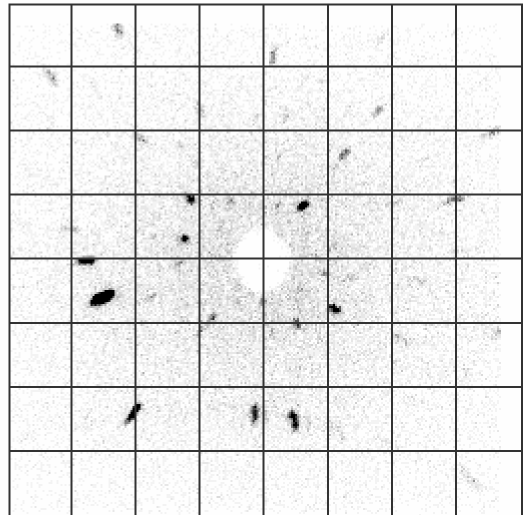

Wafer P - Grain 8

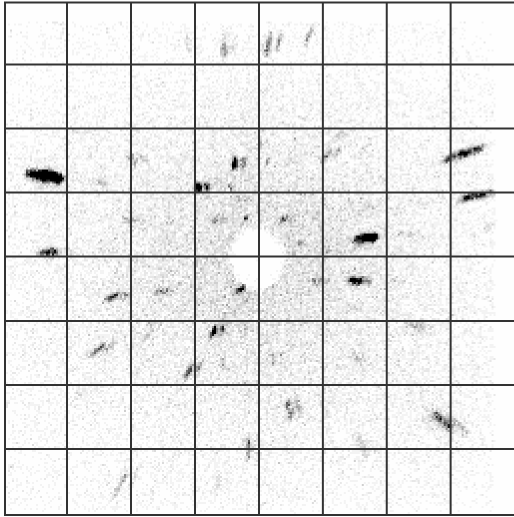

Wafer P - Grain 9

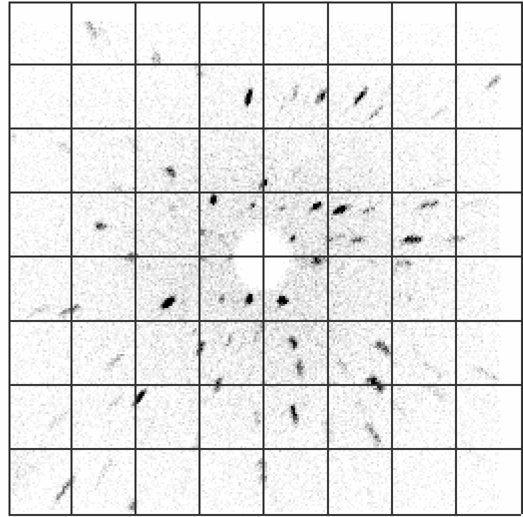

Wafer P - Grain 11

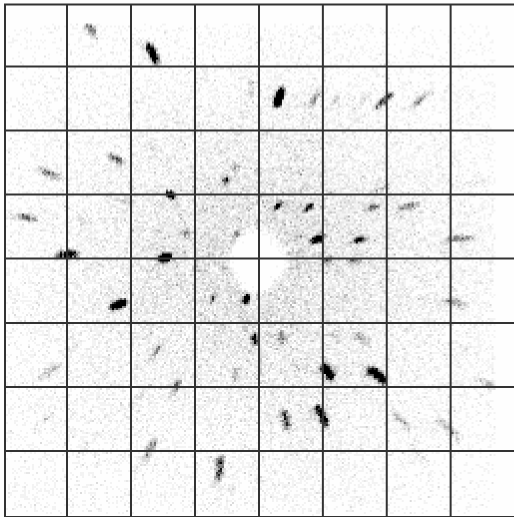

Wafer P - Grain 10

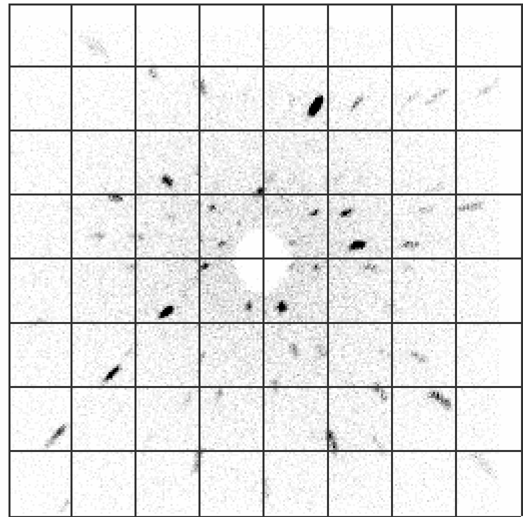

Wafer P - Grain 12

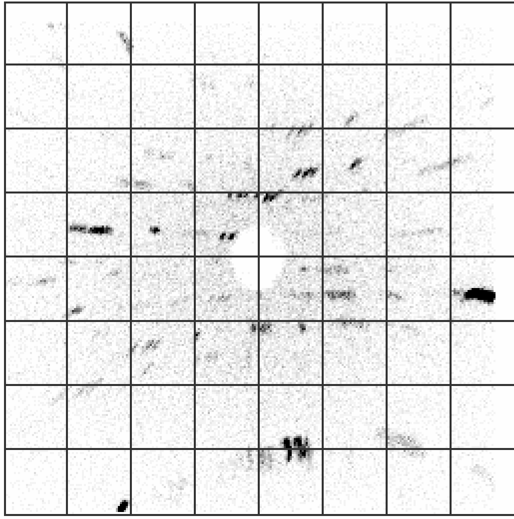

Wafer P - Grain 13

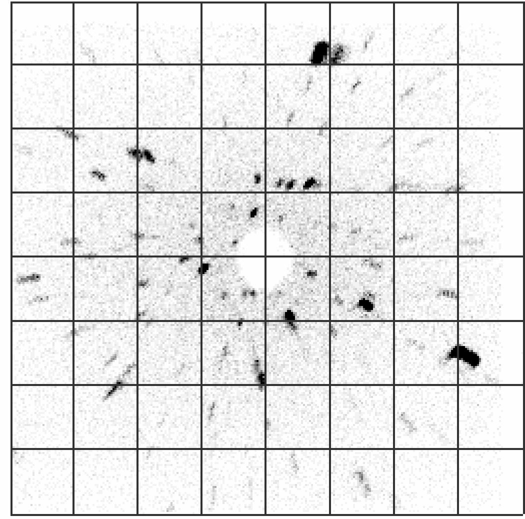

Wafer Q - Grain 1

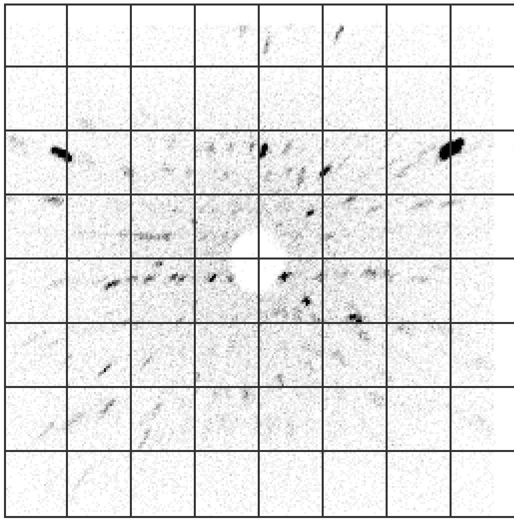

Wafer P - Grain 14

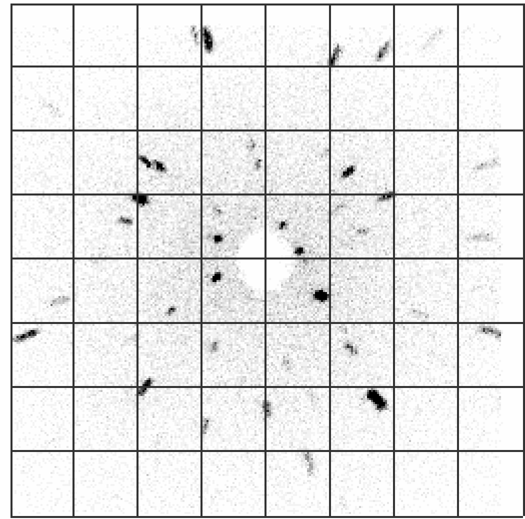

Wafer Q - Grain 2

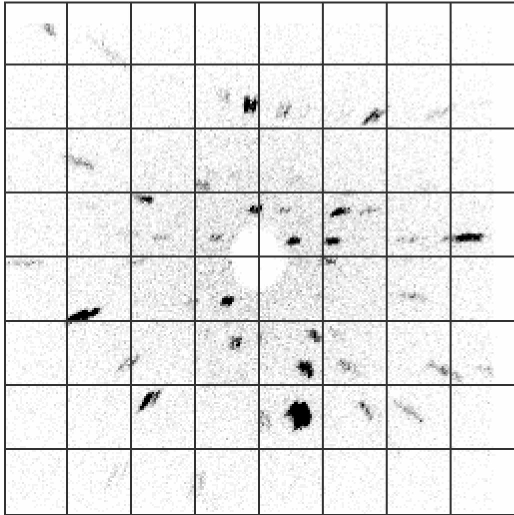

Wafer Q - Grain 3

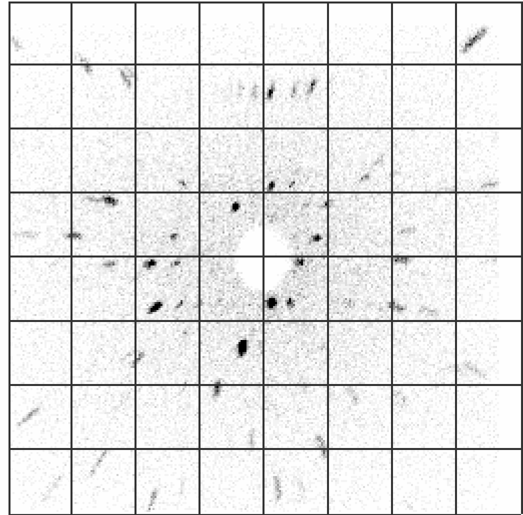

Wafer Q - Grain 5

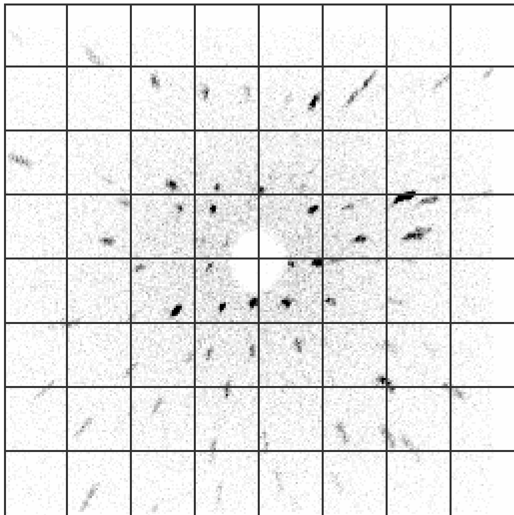

Wafer Q - Grain 4

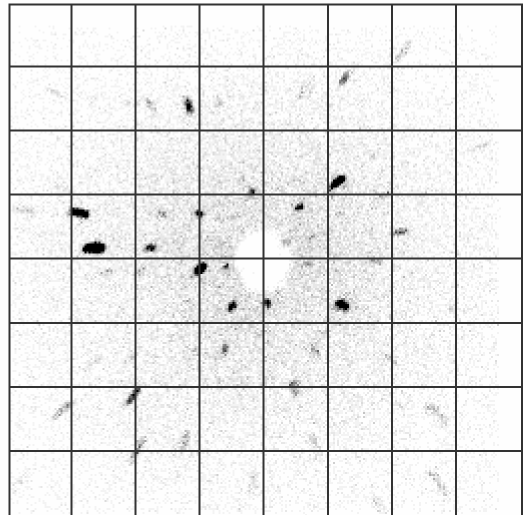

Wafer Q - Grain 6

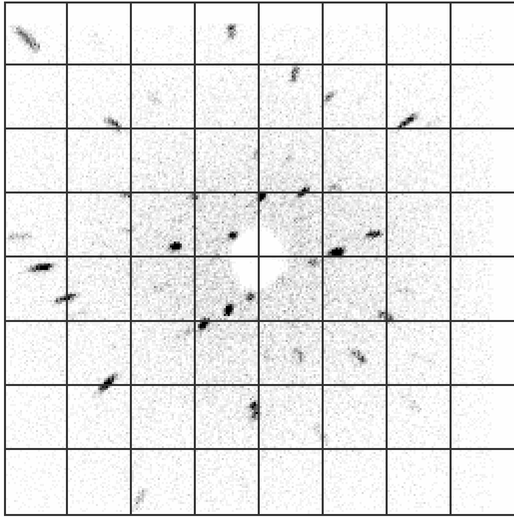

Wafer Q - Grain 7

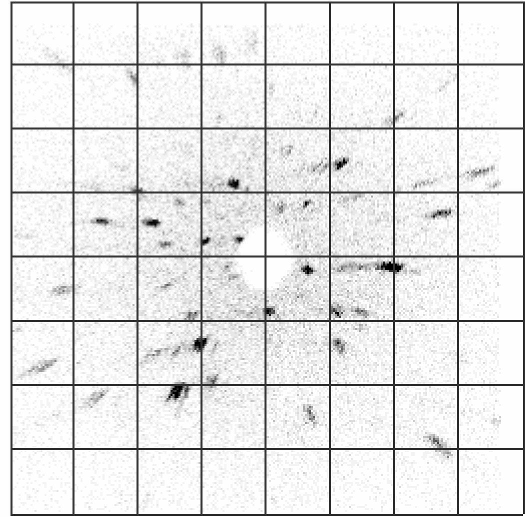

Wafer Q - Grain 9

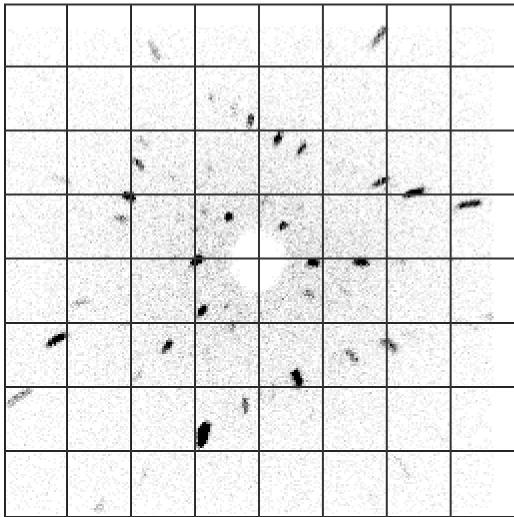

Wafer Q - Grain 8

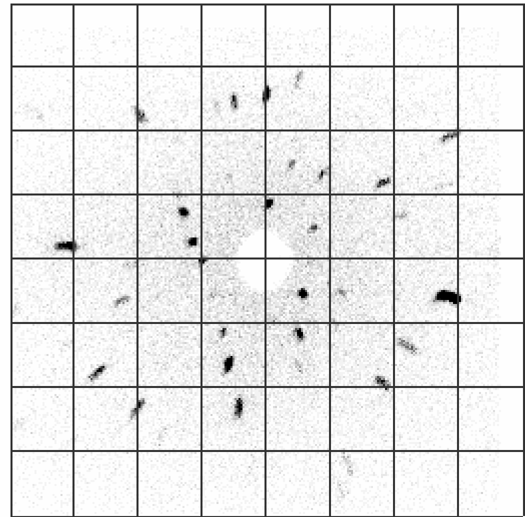

Wafer R - Grain 1

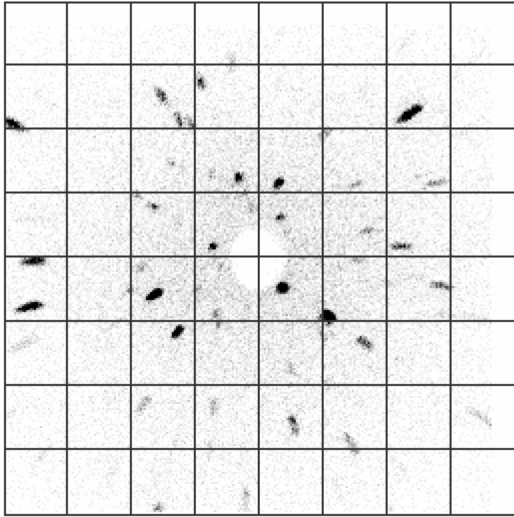

Wafer R - Grain 2

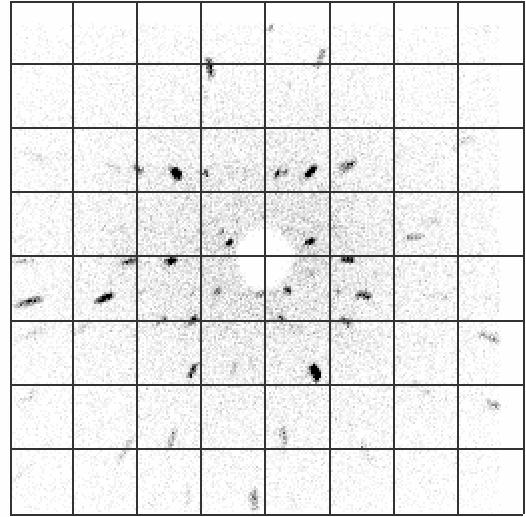

Wafer R - Grain 4

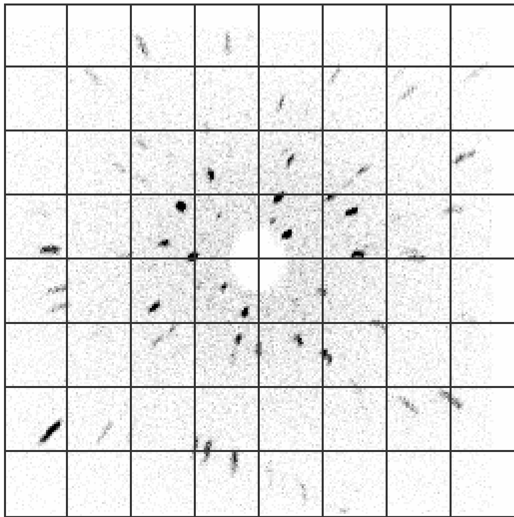

Wafer R - Grain 3

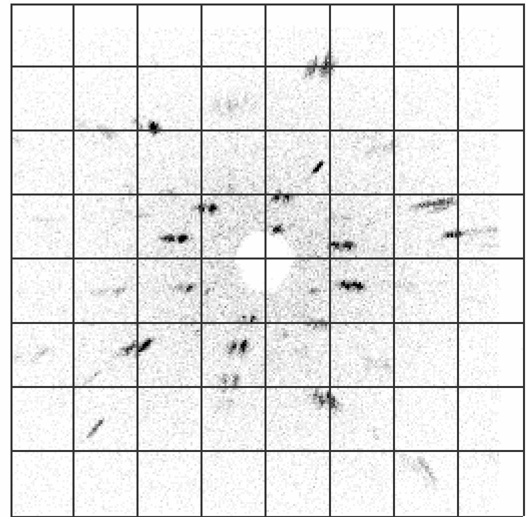

Wafer R - Grain 5

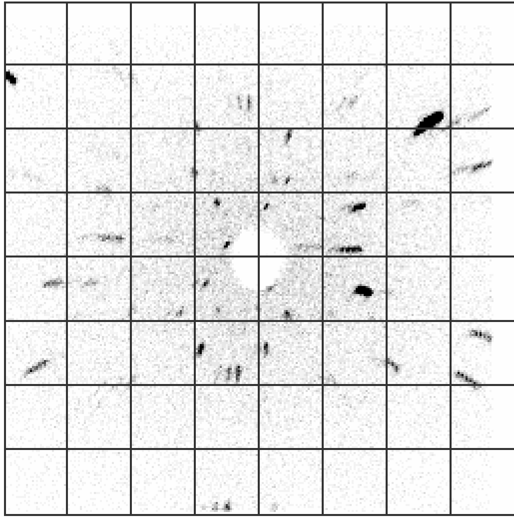

Wafer R - Grain 6

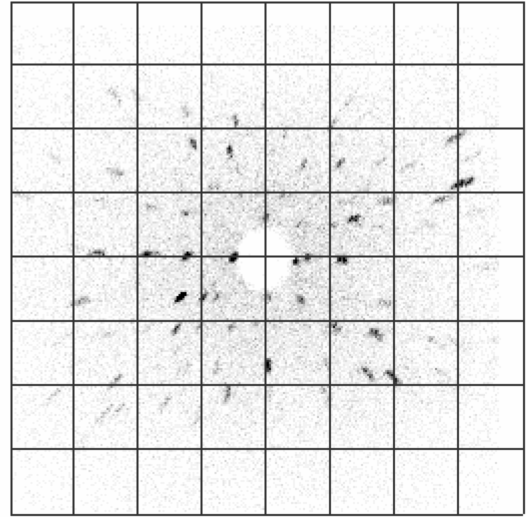

Wafer R - Grain 8

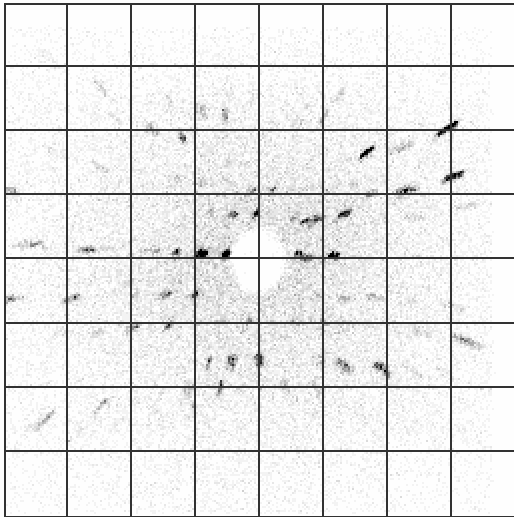

Wafer R - Grain 7

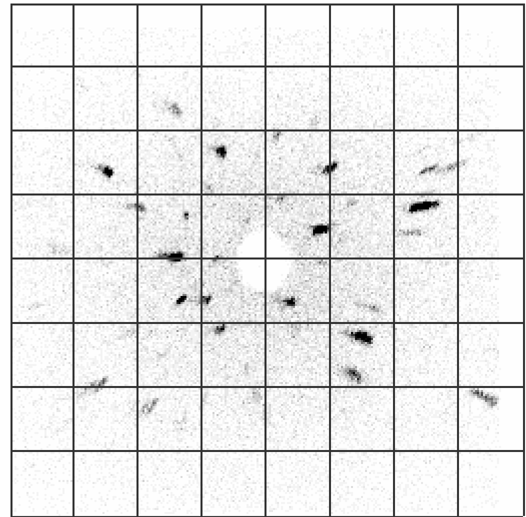

Wafer R - Grain 9

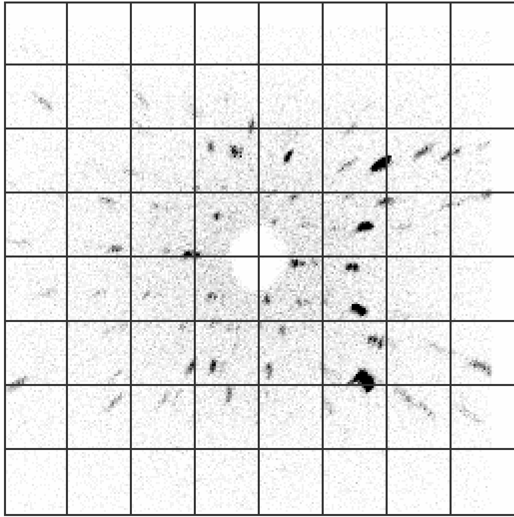

Wafer R - Grain 10

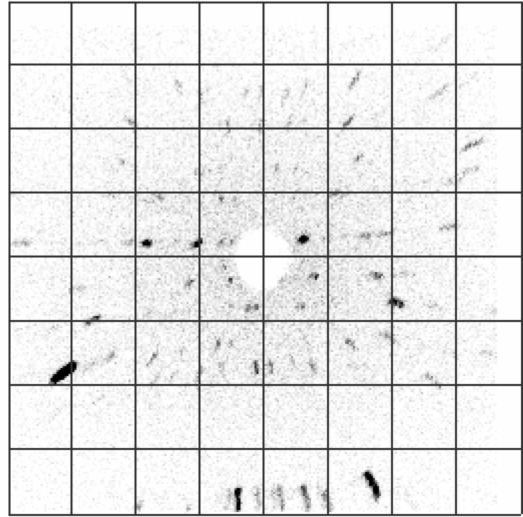

Wafer R - Grain 11

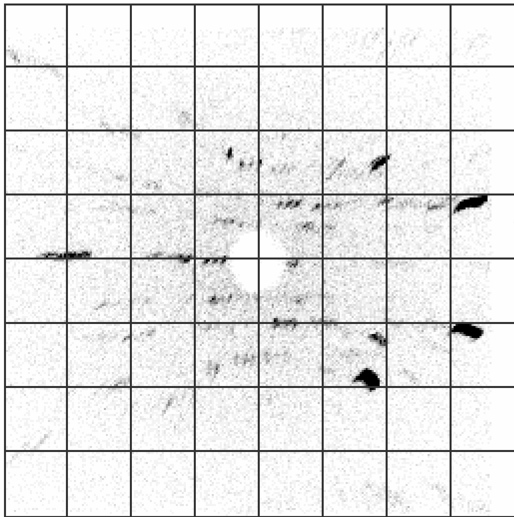

Wafer R - Grain 12

REFERENCES

[1] B. Mackintosh, et. al. Large silicon crystal hollow-tube growth by the edge-define film-fed growth (EFG) method. *Journal of Crystal Growth*. Vol. 287. p. 428-432. 2006.

[2] H. Behnken, et. al. 3D dynamic stress model for the growth of hollow silicon polygons. Journal of Crystal Growth. Vol. 275. p. 375-380. 2005

[3] J.C. Lambropoulos, et. al. "Plastic deformation influence on stress generated during silicon sheet growth at high speeds" *Journal of Crystal Growth.* Vol. 65. p. 324-330. 1983.

[4] C.K. Bhihe et. al. Residual stresses in crystal growth. *Journal of Crystal Growth.* Vol. 137. p. 86-90. 1994.

[5] S. He. Near-Infrared photoelasticity of polycrystalline silicon and its relation to in-plane residual stresses. Ph.D. Thesis. Georgia Institute of Technology. 2005.

[6] G. Hahn, et. al. Review on ribbon silicon techniques for cost reduction in PV. Photovoltaic Energy Conversion, Conference Record of the 2006 IEEE 4th World Conference. Volume 1. p. 972 – 975. May 2006.

[7] S. Ostapenko, et. al. Residual stress measurements using polariscopy and crack detection and analyses using resonance ultrasonic vibrations in crystalline silicon wafers. Proceedings from DOE Solar Energy Technologies Program Review Meeting. April 17-19, 2007.

[8] J.P. Kalejs. Point defect, carbon, and oxygen complexing in polycrystalline silicon. *Journal of Crystal Growth*. Vol. 128. p. 298-303. 1993.

[9] B. Chalmers. High-speed growth of sheet crystals. *Journal of Crystal Growth* Vol. 70. Issues 1-2. p. 3-10. December 1984.

[10] H.M. Ettouney, et. al. Comparison of finite element calculations and experimental measurements in edge-defined film-fed growth of silicon sheets. *Journal of Crystal Growth.* Vol 70. p. 306-313. 1984.

[11] J.P. Kalejs. Modeling contributions in commercialization of silicon ribbon growth from the melt. *Journal of Crystal Growth*, 230 (1-2) p.10-21, 2001.

[12] T. Zheng and S. Danyluk. Study of stresses in thin silicon wafers with near-infrared phase stepping photoelasticity. *J. Mater. Res.*, Vol. 17(1). p. 36-42. 2002.

[13] D. Brewster. *Philosophical Transactions of the Royal Society*. p. 156-178. 1816.

[14] D. Post. Photoelastic-fringe multiplication for ten fold increase in sensitivity. *Experimental Mechanics*. Vol. 10. p.305-312. 1970.

[15] C. Claeys and J. Vanhellemont. Recent progress in the understanding of crystallographic defects in silicon. *Journal of Crystal Growth.* Vol 126. p.41-62. 1993.

[16] A.H. Cottrell. *Dislocations and Plastic Flow in Crystals.* Oxford at the Clarendon Press. 1953.

[17] E. Emorhokpor, et. al. Characterization and Mapping of Crystal Defects in Silicon Carbide. *Material Processing and Devices.* Spring 2004.

[18] J. Takahashi, et. al. Sublimation growth of SiC single crystalline ingots on faces perpendicular to the (0001) basal plane. *Journal of Crystal Growth.* Vol. 135. p. 61-70. 1994.

[19] Y. Ohshita et. al. Effects of defects and impurities on minority carrier lifetime in cast-grown polycrystalline silicon. *Journal of Crystal Growth*. Vol 275 p. 491–494. 2005.

[20] K.L. Pauls, K.W. Mitchell, W. Chesarek. The effect of dislocations on the performance of silicon solar cells. *Photovoltaic Specialist Conference.* 10-14 May 1993. p. 209-213.

[21] T.Kieliba, S. Riepe, W. Warta. Effects of dislocations on minority carrier diffusion length in practical silicon solar cells. *J. of Applied Physics.* Vol. 100 (6). p. 63706-63712. 2006.

[22] I. Tarasov, et. al. Defect diagnostics in multicrystalline silicon using scanning technologies. *Physica B: Physics of Condensed Matter.* Vol 308. p. 1133-1136. 2001.

[23] C.A. Dimitriadis. Influence of dislocations on the performance of solar cells made from large-grain polysilicon. *J. Phys. D.: Appl. Phys.* Vol. 18. p. 2489-2495. 1985.

[24] R.G. Seidensticker and R.H. Hopkins. Silicon ribbon growth by the dendritic web process. *Journal of Crystal Growth.* Vol. 50 (1) p.221-235. 1980.

[25] A.R. Rosenfield, et al. *Dislocation Dynamics.* Battelle Institute, Materials Science Colloquia. McGraw-Hill. 1968.

[26] D. Franke, M. Apel. Change of dislocation density in silicon wafers during thermal processing. Photovoltaic Specialists Conference, 2000. Conference Record of the Twenty-Eighth IEEE. p. 237-240. 2000.

[27] H. Kotake and S. Takasu. "The effect of annealing on residual stress and dislocation propagation in silicon slices with damaged layer induced by scribing." *Journal of Materials Science.* Vol. 16. p. 767-774. 1981.

[28] D. Franke. Rise of dislocation density in crystalline silicon wafers during diffusion processing. *3rd World Conference on Photovoltaic Energy Conversion.* May 11-18, 2003. Japan.

[29] C. Rao, et. al. Imperfections and impurities in EFG silicon ribbons. *Journal of Crystal Growth.* Vol. 50. p.311-319. 1980.

[30] P.M. Fahey, et. al. "Stress induced dislocation in silicon integrated circuits" IBM J. Res Develop. Vol.. 36. No. 2. March 1992.

[31] N.A. Fleck, M.F. Ashby, J.W. Hutchinson. "The role of geometrically necessary dislocations in giving material strengthening." *Scripta Materialia*. Vol. 48. p. 179-183. 2003.

[32] N.A. Fleck, et. al. "Strain gradient plasticity: Theory and experiment" *Acta. Metall. Material.* Vol. 42. No. 2. p. 475-487. 1994.

[33] J.R. Patel and A..R. Chaudhuri. " Macroscopic Plastic Properties of Dislocation-Free Germanium and Other Semiconductor Crystals" *Journal of Applied Physics.* Vol. 34. No. p. 2788-2799. 1963.

[34] J.P. Kalejs, A.A. Menna, and R.W. Stormont. Stress in thin hollow silicon cylinders grown by the edge-defined film-fed growth technique. *Journal of Crystal Growth*, 104 p.14-19, 1990.

[35] R.O. DeNicola and R.N. Tauber, Effect of growth parameters on the residual stress and dislocation density of Czochralski-grown silicon crystals. *Journal of Applied Physics.* Vol. 42, No. 11. p. 4262-7270. Oct. 1971.

[36] G. Dour, et. al. Relaxation of thermal stresses by dislocation flow and multiplication in the continuous casting of silicon. *Mater. Sci. Eng.* Vol. 5. p. 275-288. 1997.

[37] H. Alexander, P. Haasen. "Dislocations and Plastic Flow in the Diamond Structure", *Solid State Physics*, Vol. 22. p. 27-158. 1968.

[38] J. Vanhellemont and S. Amelinckx. "Film-edge-induced dislocation generation in silicon substrates. I. Theoretical Model." *Journal of Applied Physics.* Vol:63 Issue:12 p. 5703-5711. 1988.

[39] N. Miyazaki, et. al. Development of three-dimensional dislocation density analysis code for annealing process of single crystal ingot. *Journal of Crystal Growth.* Vol. 243. p. 47-54. 2002.

[40] C. Tsai. On the finite element modeling of dislocation dynamics during semiconductor crystal growth. *Journal of Crystal Growth.* Vol. 113. p. 499-507. 1991.

[41] Z. Sourek, R. Bubakova. "The deformation by stress relaxation at the edge dislocation." *Phys. Stat. Sol. (A).* Vol. 70. p. 641. 1982.

[42] P.A. Mataga, et. al. Effects of transverse temperature field nonuniformity on stress in silicon sheet growth. *Journal of Crystal Growth.* Vol. 82. p.60-64. 1987.

[43] W.N. Borle and R.K. Bagai. Dislocation etch pits on various crystal planes of silicon. *Journal of Crystal Growth.* 36. p. 259-262. 1976.

[44] B. Rau, K. Petter, I. Sieber, et. al. Extended defects in Si filmes epitaxially grown by low temperature ECRCVD. *Journal of Crystal Growth.* 287. p. 433-437. 2006.

[45] A.V. Aghabekyan, G.E. Ayvazyan, A.H. Vardanyan. Distribution of slip dislocations in thermally deformed silicon wafers. *Proc. 23rd International Conference on Microelectronics.* Vol. 2. p. 555-557. 12-15 May 2002.

[46] J.M. Gere. *Mechanics of Materials, 5th Edition.* Brooks/Cole. Thomson Learning. 2001.

[47] H. Kohlbrecher, et. al. "Pipe Diffusion and Dislocation Density in Silicon." *Thin Solid Films*. Vol. 92. p. 381-383. 1982.

[48] B.L. Sopori. A new defect etch for polycrystalline silicon. *Journal of Electrochemical Society.* March 1984.

[49] H.J. Moller, et. al. "Multicrystalline silicon for solar cells." *Thin Solid Films.* Vol. 487. p. 179-187. 2005.

[50] A. Muiznieks, et. al. Stress-induced dislocation generation in large FZ and CZ silicon single crystals – numerical model and qualitative considerations. *Journal of Crystal Growth.* Vol. 230. p. 305-313. 2001.

[51] T. Suzuki, et. al. *Dislocation Dynamics and Plasticity.* Springer-Verlag. 1991.

[52] R. Peierls, Proc. Phys. Soc. Vol. 52, 34 (1940)

[53] F. Nabarro, Proc. Phys. Soc Vol 59, 256 (1947)

[54] F. A. Graybill, *Theory and Application of the Linear Model*. Colorado State University. Duxbury Classic Series. 1976.

[55] B.L. Sopori. The Principal of Dislocation Analysis by Coherent Optical Scattering from a Defect-Etch Surface. J. *Electrochem. Soc*., Vol. 135 (10) p. 2601-2606. October 1988.

[56] N. Miyazaki. Dislocation density evaluation using dislocation kinetics model. *Journal of Crystal Growth*, 303 p.302-309, 2007.

[57] D.J. Bacon, D.M. Barnett, R.O. Scattergood. Anisotropic continuum theory of lattice defects. *Progress in Materials Science.* 23. p. 51-262

[58] H. Liang. et. al. Two-dimensional state of stress in a silicon wafer. *J. Appl. Phys.* 71(6), p. 2863-2870. 1992.

[59] K. Fijiwara, et. al. Investigation of crystal growth behavior of silicon melt for growing high quality polycrystalline silicon by cast method. IEEE. 2005.

[60] A.H. Cottrell. *Dislocations and Plastic Flow in Crystals*. Oxford University Press. New York, 1953

[61] M.F. Ashby et. al. *Dislocation Modeling of Physical Systems.* Proceedings of International Conference. Pergamon Press. 1981.

[62] J. Kalejs, et. al. Challenges for EFG ribbon technology on the path to large scale manufacturing. Photovoltaic Specialists Conference, 2005. Conference Record of the Thirty-first IEEE. p. 1301 – 1304. 3-7 Jan. 2005.

[63] A. Roy, et. al. Growth of large diameter silicon tube by EFG technique: modeling and experiment. *Journal of Crystal Growth.* Vol. 230. p.224-231. 2001.